

WL-TR-94-2085

MICRO/MINIATURE HEAT PIPE ANALYSIS

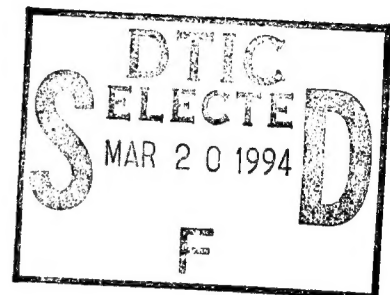


AMIR FAGHRI, PH.D.
DMITRY KHRUSTALEV, PH.D.

DEPARTMENT OF MECHANICAL AND
MATERIALS ENGINEERING
WRIGHT STATE UNIVERSITY
DAYTON, OH 45435

JULY 1994

INTERIM REPORT FOR 6/92-12/93



APPROVED FOR PUBLIC RELEASE; DISTRIBUTION IS UNLIMITED.

This document has been approved
for public release and sale; its
distribution is unlimited

AEROPROPULSION AND POWER DIRECTORATE
WRIGHT LABORATORY
AIR FORCE MATERIEL COMMAND
WRIGHT PATTERSON AFB OH 45433-7251

19950317 133

NOTICE

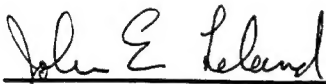
WHEN GOVERNMENT DRAWINGS, SPECIFICATIONS, OR OTHER DATA ARE USED FOR ANY PURPOSE OTHER THAN IN CONNECTION WITH A DEFINITELY GOVERNMENT-RELATED PROCUREMENT, THE UNITED STATES GOVERNMENT INCURS NO RESPONSIBILITY OR ANY OBLIGATION WHATSOEVER. THE FACT THAT THE GOVERNMENT MAY HAVE FORMULATED OR IN ANYWAY SUPPLIED THE SAID DRAWINGS, SPECIFICATIONS, OR OTHER DATA, IS NOT TO BE REGARDED BY IMPLICATION, OR OTHERWISE IN ANY MANNER CONSTRUED, AS LICENSING THE HOLDER, OR ANY OTHER PERSON OR CORPORATION; OR AS CONVEYING ANY RIGHTS OR PERMISSION TO MANUFACTURE, USE, OR SELL ANY PATENTED INVENTION THAT MAY IN ANY WAY BE RELATED THERETO.

LICENSE RIGHTS LEGEND

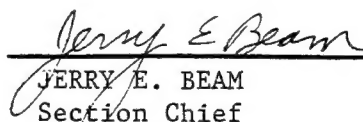
Contract Number: F33615-92-C-2276
Contractor or Subcontractor: Wright State University

For a period of two (2) years after the delivery and acceptance of the last deliverable item under the above contract, this technical data shall be subject to the restrictions contained in the definition of "Limited Rights" in DFARS clause at 252.227-7013. After the two-year period, the data shall be subject to the restrictions contained in the definition of "Government Purpose License Rights" in DFARS clause 252-227-7013. The Government assumes no liability for unauthorized use or disclosure by others. This legend, together with the indications of the portions of the data which are subject to such limitations, shall be included on any reproduction hereof which contains any portions subject to such limitations and shall be honored only as long as the data continues to meet the definition on Government purpose license rights.

This technical report has been reviewed and is approved for publication.



JOHN E. LELAND
Project Engineer
Thermal Technology



JERRY E. BEAM
Section Chief
Thermal Technology
Power Technology Branch



MICHAEL D. BRAYDICH, Lt Col, USAF
Deputy Chief
Aerospace Power Division
Aero Propulsion & Power Directorate

Publication of this report does not constitute approval or disapproval of the ideas or findings. It is published in the interest of scientific and technical information exchange.

Copies of this report should not be returned unless return is required by security considerations, contractual obligations, or notice on a specific document.

REPORT DOCUMENTATION PAGE

Form Approved
OMB No. 0704-0188

Public reporting burden for this collection of information is estimated to average 1 hour per response, including the time for reviewing instructions, searching existing data sources, gathering and maintaining the data needed, and completing and reviewing the collection of information. Send comments regarding this burden estimate or any other aspect of this collection of information, including suggestions for reducing this burden, to Washington Headquarters Services, Directorate for Information Operations and Reports, 1215 Jefferson Davis Highway, Suite 1204, Arlington, VA 22202-4302, and to the Office of Management and Budget, Paperwork Reduction Project (0704-0188), Washington, DC 20503.

1. AGENCY USE ONLY (Leave blank)		2. REPORT DATE July 1994	3. REPORT TYPE AND DATES COVERED Interim 6/92 - 12/93
4. TITLE AND SUBTITLE Micro/Miniature Heat Pipe Analysis			5. FUNDING NUMBERS C-F33615-92-C-2276 PE-63218C PR-1601 TA-05 WU-05
6. AUTHOR(S) Amir Faghri Dmitry Khrustalev			8. PERFORMING ORGANIZATION REPORT NUMBER
7. PERFORMING ORGANIZATION NAME(S) AND ADDRESS(ES) Department of Mechanical and Materials Engineering Wright State University Dayton OH 45435			10. SPONSORING/MONITORING AGENCY REPORT NUMBER WL-TR-94-2085
9. SPONSORING/MONITORING AGENCY NAME(S) AND ADDRESS(ES) Aeropropulsion & Power Directorate Wright Laboratory Air Force Materiel Command Wright-Patterson AFB OH 45433-7251			
11. SUPPLEMENTARY NOTES			
12a. DISTRIBUTION/AVAILABILITY STATEMENT Approved for public release; distribution is unlimited.			12b. DISTRIBUTION CODE
13. ABSTRACT (Maximum 200 words) Analysis presented in this report shows that longitudinal groove designs are crucial to increase the heat transport capacity of miniature heat pipes. Furthermore, vapor continuum limitation for a micro heat pipe operation is also defined and presented. The steady-state mathematical models of a micro heat pipe operation and miniature axially-grooved heat pipe are developed where the importance of the interfacial phenomena at the surfaces of the ultra-thin films is emphasized. The predicted capillary and boiling limitations as well as the thermal resistances are compared to existing experimental data on micro, miniature and conventional axially-grooved heat pipes. It is found that flat miniature heat pipes are easily capable of withstanding heat fluxes on the order of 40 W/cm ² on the evaporator wall.			
14. SUBJECT TERMS Heat Pipes, Electronics Cooling, Mathematical Model			15. NUMBER OF PAGES 175
			16. PRICE CODE
17. SECURITY CLASSIFICATION OF REPORT UNCLASSIFIED	18. SECURITY CLASSIFICATION OF THIS PAGE UNCLASSIFIED	19. SECURITY CLASSIFICATION OF ABSTRACT UNCLASSIFIED	20. LIMITATION OF ABSTRACT UL

FOREWORD

The information in this report was assembled for contract F33615-92-C-2276 with Aero Propulsion and Power Directorate, Wright Laboratory and SDIO/IST as the supporting agencies. The work was carried out at the Department of Mechanical and Materials Engineering at Wright State University.

From June 1992-December 1993, four tasks were completed as outlined in the Table of Contents. The various tasks dealt with performance characteristics of micro/miniature heat pipes systems. Four journal publications and four conference papers were produced from the present work. Dr. John Leland from Wright Laboratory was the technical supervisor for this contract, and the authors are grateful to him for various detailed technical assistance and discussions. We greatly appreciate him for his time and effort in all phases of the contract. Support from Dr. Tom Mahefkey and Dr. Jerry Beam to initiate this contract is also acknowledged.

Accession For	
NTIS CRA&I	<input checked="" type="checkbox"/>
DTIC TAB	<input type="checkbox"/>
Unannounced	<input type="checkbox"/>
Justification	
By	
Distribution /	
Availability Codes	
Dist	Avail and/or Special
A-1	

Amir Faghri

Dmitry Khrustalev

Contents

List of Figures	viii
List of Tables	xiii
List of Symbols	xiv
 1 MICRO/MINIATURE HEAT PIPES AND OPERATING LIMITA-	
TIONS	1
1.1 Summary	1
1.2 Literature Review	2
1.3 Vapor Continuum Limitation	12
1.4 Capillary Limitation	21
1.5 Conclusions and Remarks	31
 2 THERMAL ANALYSIS OF A MICRO HEAT PIPE	33
2.1 Summary	33
2.2 Introduction	34

2.3	Mathematical Model	35
2.4	Heat Transfer in the Condenser Section	44
2.5	Heat Transfer in the Evaporator Section	49
2.6	Liquid Flow in a Capillary Groove	55
2.7	Numerical Treatment	56
2.8	Results and Discussion	61
2.9	Conclusions	72
3	EVAPORATION AND CONDENSATION ON GROOVED STRUCTURES	74
3.1	Summary	74
3.2	Introduction	75
3.3	Formation of and Heat Transfer in Thin Liquid Films	79
3.4	Heat Transfer in the Thin-Film Region of the Evaporator	85
3.5	Heat Transfer in the Thin Film Region of the Condenser	92
3.6	Heat Conduction in the Metallic Fin and Meniscus Region Film	95
3.7	Numerical Treatment	98
3.8	Results and Discussion	99
3.9	Conclusions	111
4	ANALYSIS OF MINIATURE GROOVED HEAT PIPES	115

4.1	Summary	115
4.2	Introduction	116
4.3	AGHP Mathematical Model	118
4.4	Fluid Circulation in an AGHP and the Capillary Limitation	120
4.5	Boiling Limitation and Heat Transfer Coefficients	126
4.6	Numerical Treatment	132
4.7	Results and Discussion	133
4.8	Conclusions	142
	References	146

List of Figures

1.1	The flat heat pipe developed by ITOH Research and Development Corporation	4
1.2	The heat pipe tested by Babin et al. (1989).	6
1.3	Miniature heat pipe tested by Plesch et al. (1991) (Dimensions in mm)	7
1.4	Transition temperature for sodium as the heat pipe working fluid (Cao and Faghri, 1994)	14
1.5	Transition temperatures for water and methanol as heat pipe working fluids (Cao and Faghri, 1994)	16
1.6	Boiling limits as a function of liquid thickness for $T_v = 80^\circ\text{C}$, $R_b = 2.54 \times 10^{-7}$ m (Cao and Faghri, 1994)	19
1.7	Boiling limits as a function of R_b for $T_v = 80^\circ\text{C}$, $\delta = 10^{-5}$ m (Cao and Faghri, 1994)	20
1.8	Evaporating, nonevaporating regions and coordinate system (not to scale)	25

1.9	Dimensionless heat sink as a function of working fluids for $\Delta T = 0.1^\circ\text{C}$ (Cao and Faghri, 1994)	29
1.10	Schematic of liquid film distributions in the micro heat pipe	30
2.1	Schematic of the micro heat pipe and coordinate systems for analysis	36
2.2	Details of the micro heat pipe cross section in (a) the evaporator, (b) the condenser	38
2.3	Cross section of the end of the extended meniscus region near a heated wall	50
2.4	Comparison of the performance of the micro heat pipe with and without shear stress at the vapor-liquid interface for the case of no excess liquid in the MHP ($\theta_0 = 10^\circ$) (a) liquid cross sectional area, (b) radius of curvature of the meniscus, (c) pressure variation	62
2.5	Dependence of the maximum heat transfer on (a) meniscus contact angle at the evaporator end cap, (b) mass of circulating liquid in the case of insufficient liquid fill ($\theta_0 = 10^\circ$, $R_{m0} = 50\mu\text{m}$)	64
2.6	Maximum heat transfer versus operating temperature (a) copper-water MHP, (b) silver-water MHP	66
2.7	Performance characteristics of the copper-water MHP (a) radius of the liquid surface curvature, (b) temperature distribution	67

2.8	Influence of total heat input on the thermal resistance and liquid blocking length (copper-water MHP)	68
2.9	Variation of the contact angle in the condenser	70
2.10	New configuration cross section of a flat MHP	71
3.1	Cross sections of the characteristic elements of an axially-grooved heat pipe (a) condenser, (b) evaporator	77
3.2	Thin evaporating film on a fragment of the rough solid surface	78
3.3	Characteristics of the evaporating film along the solid-liquid interface (ammonia, $T_v = 250$ K) (a) free liquid surface temperature, (b) thickness of the film, (c) generalized capillary pressure	101
3.4	Heat flux through the evaporating film (ammonia, $T_v = 250$ K, $\alpha = 1$) (a) along the solid-liquid interface (microfilm region), (b) along the fin axis ($R_r = 0.33 \mu\text{m}$, $\Delta T = 1$ K)	102
3.5	Local heat transfer coefficient in the evaporator of the ammonia-Al heat pipe ($T_v = 250$ K) (a) versus roughness size, (b) versus heat flux ($R_r = 1 \mu\text{m}$)	103

3.6	Effect of the meniscus contact angle on the local evaporative heat transfer coefficients ($\Delta T = 1$ K) (a) ammonia-Al heat pipe by Schlitt et al. (1974), ($T_v = 250$ K), (b) ethane-Al heat pipe by Schlitt et al. (1974), ($T_v = 200$ K), (c) water-copper evaporator by Ivanovskii et al. (1984), ($T_v = 300$ K)	107
3.7	Effect of the meniscus contact angle in the heat pipe condenser on (a) liquid film thickness variation along the surface of the fin top (ammonia, $\Delta T = 1$ K, $T_v = 250$ K), (b) local heat transfer coefficient for ammonia ($T_v = 250$ K), (c) local heat transfer coefficient for ethane ($T_v = 200$ K)	112
4.1	Flat miniature axially-grooved heat pipe cross sections	117
4.2	Performance characteristics of the ammonia-Al heat pipe ($T_v = 250$ K) (a) meniscus contact angle and fluid pressure, (b) local heat transfer coefficients, (c) wall and vapor temperatures	135
4.3	Temperature drop in the evaporator versus heat load (a) ammonia-Al heat pipe ($T_v = 250$ K), (b) ethane-Al heat pipe ($T_v = 200$ K), (c) water-copper planar evaporator ($T_v = 300$ K) and flat miniature AGHP ($T_v = 378$ K)	137
4.4	Temperature drop in the condenser versus heat load: (a) ammonia-Al heat pipe ($T_v = 250$ K), (b) ethane-Al heat pipe ($T_v = 200$ K)	139

4.5	Maximum heat transfer versus elevation height (a) ammonia-Al heat pipe ($T_v = 203$ K), (b) ethane-Al heat pipe ($T_v = 200$ K), (c) water-copper flat miniature heat pipe	140
4.6	Maximum heat transfer of the flat miniature heat pipe versus groove depth (vertical orientation) (a) $T_v = 55^\circ$, (b) $T_v = 105^\circ$	143
4.7	Maximum heat transfer of the flat miniature heat pipe versus groove depth (horizontal orientation) (a) $T_v = 55^\circ$, (b) $T_v = 105^\circ$	144

List of Tables

3.1	Comparison of the predicted \bar{h}_e with existing experimental data . . .	108
3.2	Comparison of the results with simplified models	110

NOMENCLATURE

a, b, B, C	constants
A	cross sectional area, [m ²], or Hamaker constant ($6\pi\overline{A}$)
A'	dispersion constant [J]
B	width of inner wall [m]
c_p	specific heat at constant pressure [J/(kg-K)]
c_v	specific heat at constant volume [J/(kg-K)]
C	modification constant
D	minimum space dimension [m]
D_h	hydraulic diameter [m]
f	friction coefficient
f_v	friction coefficient
F	dimensionless shear stress
g	gravity constant [m/s ²]
h	heat transfer coefficient [W/(m ² -K)]
h_{fg}	latent heat of vaporization [J/kg]
H	meniscus height or elevation [m]
k	thermal conductivity [W/(m-K)]
K	wick permeability [m ²]
K	curvature [1/m]

Kn	Knudsen number
L	length [m]
L_t	total length of the heat pipe [m]
L_{eff}	effective heat pipe length [m]
L_1	half-length of thin film or dry zone in Section 2 [m]
L_1	half-width of the top of the fin in Sections 3 and 4 [m]
L_2	length of the condensate film [m]
\dot{m}'	interfacial flux [kg/(s · m ²)]
\dot{m}	mass flow rate [kg/s]
M	molecular weight in Section 1, [kg/kmol], or mass [kg]
Ma	$\bar{w}_{v,a}/\sqrt{\gamma_0 R_g T_v}$, Mach number
\dot{n}	number of active sites per square centimeter
N	number of corners or grooves
p	pressure [Pa]
p_d	disjoining pressure [Pa]
q	heat flux [W/m ²]
Q	integral heat sink for the contact line region in Section 1 [W] or axial heat flow through the heat pipe cross section in Sections 2-4 [W]
Q_a	total heat input [W]

Q'	heat flow rate per unit length [W/m]
Q^*	dimensionless contact line heat sink
Q_{\max}	maximum heat transport rate [W]
r	thermal resistance [K/W]
r_b	radius of vapor bubble at the liquid-wall interface [m]
r_h	hydraulic radius [m]
r_{eff}	effective capillary radius of the wick pores at the liquid-vapor interface [m]
R	gas constant, [J/(kg-K)], or radius [m]
Re	Reynolds number, UD_h/ν or $\bar{w}_v D_{h,v}/\nu_v$, vapor axial Reynolds number
Re_r	$\bar{v}_{v,\delta} D_{h,v}/\nu_v$, radial Reynolds number
R_g	gas constant [J/(kg-K)]
R_m	radius of curvature of the meniscus [m]
R_o	outer pipe radius [m]
R_r	characteristic roughness size [m]
R_v	vapor space radius [m]
s	coordinate along the solid-liquid interface [m]
t	heat pipe thickness [m]
t_g	groove depth [m]

t_t	height of the curved top of the fin [m]
t_w	wall thickness [m]
T	temperature [K]
T_w	temperature of the solid-liquid thin film interface [K]
u	velocity of microfilm flow along the s -coordinate [m/s]
v	radial velocity or vapor velocity along the η -coordinate [m/s]
\bar{v}	mean radial velocity [m/s]
V	dimensionless volume flux
V_ℓ	molar volume of liquid [m ³ /kmol]
w	axial velocity [m/s]
\bar{w}	mean axial velocity [m/s]
W	heat pipe width in Section 1 [m]
W	half-width of meniscus in Section 2 [m]
W	half-width of a groove in Sections 3 and 4 [m]
x, y	coordinates [m]
\dot{x}, \dot{y}	coordinates (Fig. 2.3) [m]
Y	curvature of meniscus [1/m]
z	axial coordinate [m]

Greek symbols

α	accommodation coefficient
β	liquid geometric shape parameter in eqn. (1.13)
β	momentum flux coefficient
γ	half-angle of the corner or of the groove
γ_0	c_p/c_v , ratio of specific heats
δ	liquid film thickness [m]
δ_0	equilibrium (nonevaporating) thickness [m]
Δ_a	absolute error
Δp	$p - p_{v0} + \sigma/R_{m0} + 1$, pressure drop [N/m ²]
Δ_r	relative error
ΔQ	heat flow per unit groove length [W/m]
ΔT	$ T_w - T_v $, temperature drop [K]
ϵ	emissivity
η	coordinate normal to the solid-liquid interface [m] or dimensionless thickness
θ	meniscus contact angle
θ_f	contact angle obtained from the smooth-surface model
θ_{\min}	minimum wetting contact angle
θ_0	minimum wetting contact angle in Section 2
κ	Boltzmann's constant in eqn. (1.2) [J/K]

	or characteristic angle of the fin top
λ	vapor mean free path, [m], or dimensionless group defined in eqn. (1.21)
μ	dynamic viscosity [Pa-s]
ν	kinematic viscosity [m ² /s]
ρ	density [kg/m ³]
σ	collision diameter in eqn. (1.2), [Å], or liquid surface tension [N/m]
σ_0	Stefan-Boltzmann constant [W/(m ² -K ⁴)]
χ	π/N , angle (for circular geometry)
τ	shear stress at the interface [Pa]
φ	inclination angle from horizontal

Subscripts

a	adiabatic
b	vapor bubble, blocking
bot	bottom of a groove
c	condenser
cap	capillary
crit	critical
e	evaporator

<i>eff</i>	effective
<i>ex</i>	external
<i>f</i>	thin film
<i>fin</i>	fin
<i>g</i>	groove
<i>l</i>	liquid
<i>lv</i>	liquid-vapor interface
<i>max</i>	maximum
<i>men</i>	meniscus
<i>mic</i>	microfilm region
<i>o</i>	outer
<i>pc</i>	phase change
<i>rf</i>	reference
<i>s</i>	wall-liquid interface in Section 1
<i>sat</i>	saturation
<i>t</i>	total
<i>tr</i>	transition region
<i>v</i>	vapor
<i>w</i>	wall
δ	liquid film free surface

ω_1	interface between the liquid and the side of a groove
ω_2	liquid-vapor interface
ω_3	interface between the liquid and the bottom of a groove

Chapter 1

MICRO/MINIATURE HEAT PIPES AND OPERATING LIMITATIONS

1.1 Summary

A literature review related to miniature and micro heat pipes is given. It is found that longitudinal groove designs are crucial to increase the heat transport capacity of miniature heat pipes. In addition to the operational limitations of conventional heat pipes, micro heat pipes may be subject to the vapor continuum limitation, which may prevent micro heat pipes from operating under lower working temperatures. An

analysis of the capillary limit reveals that the disjoining pressure may play a role in heat transfer for the micro heat pipe and may increase its heat transfer capacity.

1.2 Literature Review

Thermal management is one of the most critical technologies in electronic product development, and directly influences the cost, reliability, and performance of the finished product. As the number of circuits on a computer chip increases, it becomes more difficult to dissipate the heat which is generated. The chip heat fluxes in mainframe computers, for example, have reached 60 W/cm^2 , and are expected to exceed 100 W/cm^2 by the year 2000 (Jacobs and Hartnett, 1991). In addition to the limitations on the maximum chip temperature, there may be further requirements on the level of temperature uniformity. Because of the high heat fluxes and temperature uniformity considerations, it is necessary to develop new methods for distributing and removing heat from modern electronic devices. The micro heat pipe is one of the promising technologies for the achievement of high local heat removal rates and uniform temperatures in computer chips. Micro heat pipe structures can be fabricated on the surface of the substrate of electronic chips using the same technology that forms the circuitry. These thermal structures can be an integral part of the electronic chip and remove heat directly from the area where maximum dissipation occurs (Jacobs and Hartnett, 1991). Micro heat pipes can also find applications in cooling the leading

edge of stator vanes in turbines and in space waste heat radiator panels by increasing the effective thermal conductivity of phase-change materials.

Cotter (1984) was the first to propose the micro heat pipe concept for the cooling of electronic devices. The micro heat pipe was defined as a heat pipe in which the mean curvature of the vapor-liquid interface is comparable in magnitude to the reciprocal of the hydraulic radius of the total flow channel. Typically, micro heat pipes have convex but cusped cross sections (for example, a polygon), with hydraulic diameters in the range of 10 to 500 μm .

Based on the original idea proposed by Cotter (1984), a silver and a copper flat micro heat pipe with dimensions 0.6 (W) x 0.1 (T) x 25 (L) mm were manufactured by the ITOH Research & Development Corporation (Japan). A heat transport rate of 0.3 W was reportedly obtained, which corresponds to a heat flux on the order of 1 W/cm². Flat heat pipes with dimensions on the order of 10 (W) x 10 (T) x 50 (L) mm were also built for the cooling of semiconductor elements (Fig. 1.1). The flat heat pipe can be installed on a semiconductor element or a semiconductor substrate with the flat surface of the heat pipe parallel to the substrate. On the inner surface of the flat wall which is in contact with the semiconductor surface, small grooves were made in the longitudinal direction to provide capillary pumping. The heat pipes manufactured by ITOH, by definition, are not actually micro heat pipes, but are in the miniature or semi-micro range. Since most microelectronic components are

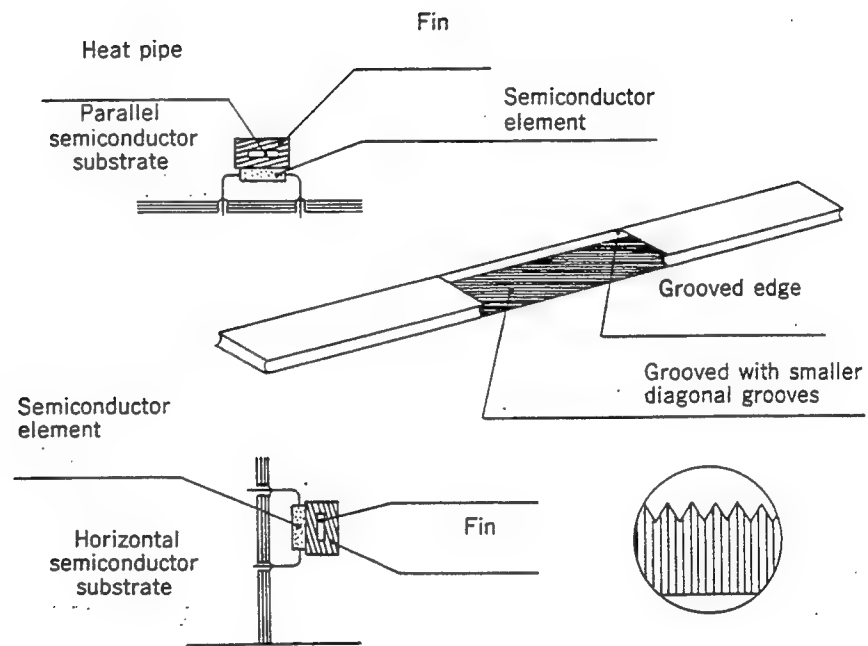


Figure 1.1: The flat heat pipe developed by ITOH Research and Development Corporation

shaped as thin plates with flat base plates, and the thermal conductivity of silicon is rather high, the heat transfer resistance in the transverse direction is relatively small. Therefore, a flat heat pipe attached on the component surface is advantageous in cooling microelectronic chips with moderate or high heat fluxes.

Babin et al. (1989) tested a trapezoidal heat pipe with a square cross section of 1 mm^2 and a length of 57 mm manufactured by ITOH, which is shown in Fig. 1.2. The case material was either copper or silver and the working fluid was ultrapure water. The triangular grooves in the four corners of the heat pipe served as arteries for the return of liquid. The maximum heat transport rate was about 0.5 W at working temperatures of 60 to 70°C , which corresponds to heat fluxes of about 1 W/cm^2 on the outer surface of the evaporator. Wu and Peterson (1990) tested a flat heat pipe with a cross section of $1 \text{ mm} \times 2 \text{ mm}$ and a length of 60 mm with ultrapure deionized water as the working fluid. The heat pipe was specifically designed for use in the thermal control of ceramic chip carriers. In this application, the heat pipe is fitted securely under the chip and is attached to the chip carrier. A maximum heat transport rate of 1.3 W was obtained which corresponds to a heat flux of 5 W/cm^2 .

Plesch et al. (1991) tested two types of miniature flat heat pipes for heat removal from microelectronic circuits, both having overall dimensions of 7 (W) \times 2 (T) \times 120 (L) mm. The first type of heat pipe (Fig. 1.3(a)) has two arteries which are formed by the spars of an inserted frame and the wall of the casing. Transverse grooves

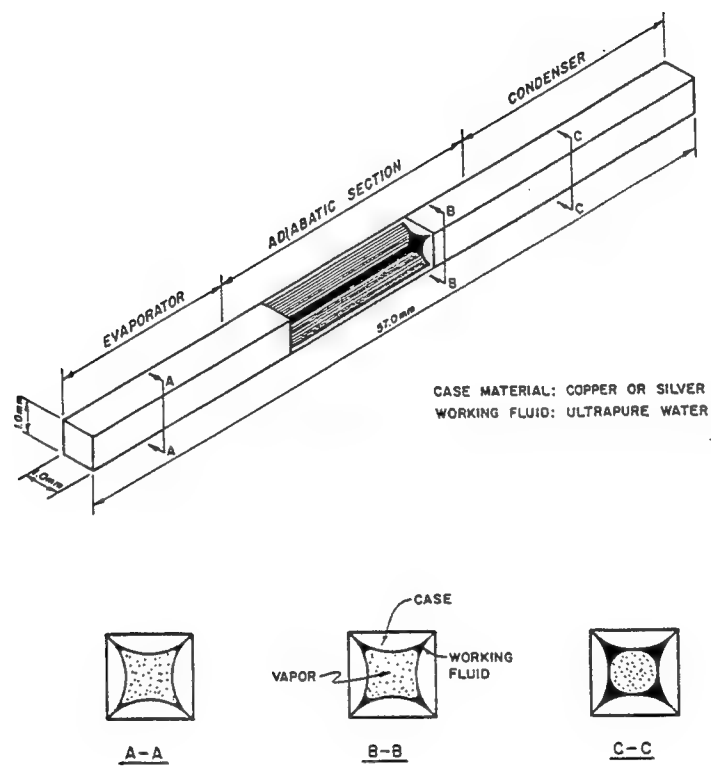


Figure 1.2: The heat pipe tested by Babin et al. (1989).

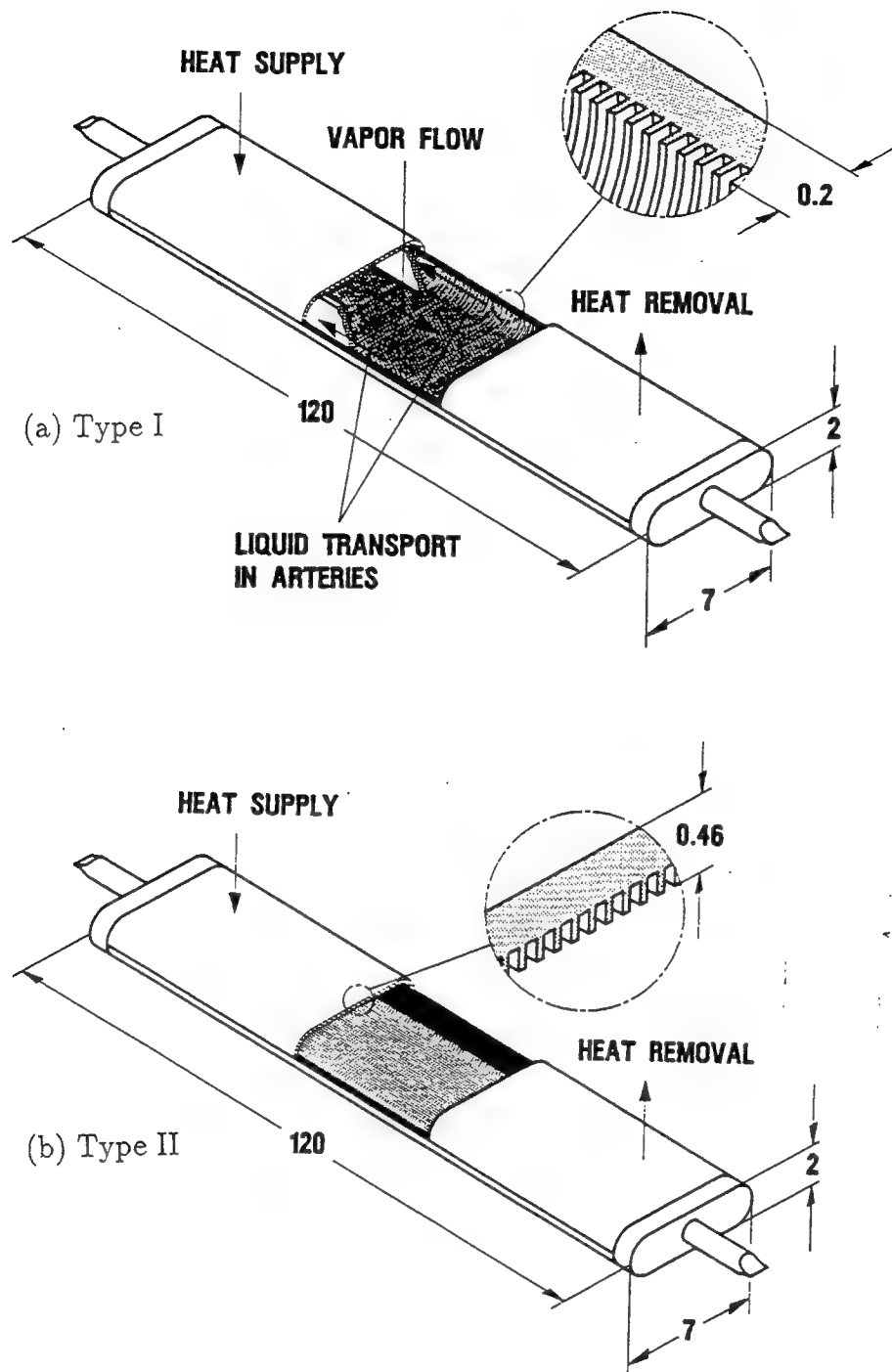


Figure 1.3: Miniature heat pipe tested by Plesch et al. (1991) (Dimensions in mm)

were provided to allow transverse transport of liquid working fluid in the heating and cooling zones. The second type (Fig. 1.3(b)), however, has longitudinal grooves over its entire length. For the first type, a maximum heat transport rate of about 16.5 W was obtained in a horizontal arrangement with a cooling water temperature of 67°C. The temperature drop over the heat pipe length in this case was about 25°C. For the second type, the maximum heat transport rate obtained was nearly 70 W, which corresponds to a heat flux of about 35 W/cm² in a horizontal arrangement with a cooling water temperature of 42°C. The temperature drop over the heat pipe in this case was about 35°C. For the vertical arrangement of the heat pipe with the cooling zone on top, the heat transport capacity was even higher, where the maximum heat flux reached 60 W/cm². Compared to the miniature heat pipes built by ITOH, which were tested by Babin et al. (1989), Wu and Peterson (1990), Itoh and Polasek (1990a; 1990b), the maximum heat fluxes obtained by Plesch et al. (1991) were much higher. This difference may be due to the different inner surface configurations of the heat pipes, which provide capillary forces for liquid to flow back to the evaporator. For the heat pipe tested by Plesch et al. (1991), many fine axial grooves were manufactured on the inner wall of the surface which contacts the electronic device. For the heat pipes by ITOH, however, only four corners provide capillary pumping. Since the circumferential length of the heat pipe cross section is relatively large, the capillary force provided by the four corners is obviously not large enough to pump a sufficient

amount of liquid back to the evaporator. Further investigations have been completed recently in the area of miniature heat pipes. These include Kojima et al. (1992), Lee et al. (1992), Chen et al. (1992), Zhou et al. (1992), Li et al. (1992) and Zhang et al. (1992). Kojima et al. (1992) developed and investigated a new cooling system with miniature heat pipes, which collects and removes heat from several large-scale integrated circuits (LSIs). The diameter of the heat pipes studied was 3 mm. The cooling system was mounted on every surface of the LSIs and cooling fins were connected to the heat pipes. The performance of the cooling system with miniature heat pipes was several times higher than the normal mounting style.

Lee et al. (1992) reported a visual and experimental study on the two-phase flow and heat transfer characteristics of small two-phase closed thermosyphons with wire inserts. The inside diameters of the tested thermosyphons were 1.0 ~ 3.6 mm, and the wire diameters were 0.4 ~ 1.5 mm. They concluded that for a two-phase closed thermosyphon made of a very small diameter tube ($ID < 2.3$ mm), it is necessary to have wire inserts to achieve normal operation as a heat transfer element. Also, the heat transfer characteristics of such two-phase closed thermosyphons with wire inserts were very similar to those of two-phase closed thermosyphons made of large diameter tubes without wire inserts.

Chen et al. (1992) conducted visualization experiments for a glass heat pipe. The outside diameter of the glass capillary is 2 mm, the wall thickness is 0.25 to 0.3

mm, and the total tube length was 113 to 118 mm. Four basic two-phase flow patterns were observed: (a) liquid projectile flow, (b) slug flow, (c) suspended liquid column, and (d) annular flow. The concept of the two-phase flow in porous media employing modified relative permeabilities was used to calculate the maximum performance of a micro heat pipe. The calculated maximum performance for vertical orientation is about three times larger than that for horizontal orientation.

Zhou et al. (1992) experimentally studied the operational characteristics of a copper/acetone miniature heat pipe. They found that the maximum operating power of the heat pipe was limited by the capillary limit, which was independent of the cooling air velocity. However, the cooling air temperature had an important effect on the maximum power.

Li et al. (1992) experimentally studied cylindrical miniature heat pipes with inner diameters of 1.2 mm and 2.5 mm, and lengths of 100 mm and 120 mm. They found that the effects of the amount of the working fluid on the heat transfer performance for small heat pipes were larger than those for conventional heat pipes, and the influence of entrainment on the capillary limit is more important for a small diameter heat pipe than a larger one.

The minimum cross sectional dimension of the above miniature heat pipes was on the order of 1 mm, and the heat pipes were attached to the electronic components to be cooled. Since the minimum dimension of the heat pipes is not very

small, the performance characteristics should not deviate significantly from those of conventional heat pipes. Recently, attempts were being made to etch micro heat pipes directly into the silicon and use them as thermal spreaders (Peterson, 1990; Gerner et al., 1992). These heat pipes are expected to have hydraulic diameters on the order of $10\text{ }\mu\text{m}$, which are classified as actual or “true” micro heat pipes. As the size of heat pipes diminishes, some performance characteristics are expected to be different from those of conventional heat pipes.

Recently Khrustalev and Faghri, (1993) developed a detailed mathematical model in which the heat and mass transfer processes in a micro heat pipe (MHP) are examined. This model describes the distribution of the liquid in an MHP and its thermal characteristics depending upon the liquid charge and the applied heat load. The liquid flow in the triangular-shaped corners of an MHP with polygonal cross section is considered by accounting for the variation of the curvature of the free liquid surface and the interfacial shear stresses due to liquid-vapor frictional interaction. The predicted results obtained by Khrustalev and Faghri (1993) are compared to existing experimental data. The importance of the liquid fill, minimum wetting contact angle, and the shear stresses at the liquid-vapor interface in predicting the maximum heat transfer capacity and thermal resistance of the MHP is also demonstrated.

1.3 Vapor Continuum Limitation

As the size of the micro heat pipe decreases, the vapor in the heat pipe core will lose its continuum characteristics. The continuum criterion is usually expressed in terms of the Knudsen number (Cao and Faghri, 1992a)

$$Kn = \frac{\lambda}{D} = \begin{cases} \leq 0.01 & \text{continuum vapor flow} \\ > 0.01 & \text{rarefied or free molecular flow} \end{cases} \quad (1.1)$$

where λ is the mean free path of the vapor, and D is the minimum dimension of the vapor flow passage. For a circular vapor space, D is the vapor core diameter. The heat transport capability of a heat pipe operating under the rarefied or free molecular vapor condition is very limited, and a large temperature gradient exists along the heat pipe length. As a result, the micro heat pipe will lose its advantages as an effective cooling method for microelectronic devices. Therefore, this heat transport limitation is referred to as the vapor continuum limitation in this paper.

The mean free path given by Tien and Lienhard (1979), based on the kinetic theory of dilute gases, is

$$\lambda = \frac{1.051 \kappa T}{\sqrt{2} \pi \sigma^2 p} \quad (1.2)$$

where σ is the collision diameter, and κ is the Boltzmann constant.

By combining eqns. (1.1) and (1.2) and applying the equation of state

$$p = \rho R T \quad (1.3)$$

for pressure p , one can obtain the transition density from continuum to rarefied or free molecular vapor flow as

$$\rho = \frac{1.051 \kappa}{\sqrt{2\pi} \sigma^2 R D Kn} \quad (1.4)$$

Assuming that the vapor is in the saturation state, the transition vapor temperature corresponding to the transition density can be obtained by using the Clausius-Clapeyron equation combined with the equation of state

$$T_{tr} = \frac{p_{rf}}{\rho R} \exp \left[\frac{-h_{fg}}{R} \left(\frac{1}{T_{tr}} - \frac{1}{T_{rf}} \right) \right] \quad (1.5)$$

where p_{rf} and T_{rf} are the reference (saturation) pressure and temperature, and the vapor density ρ is given by eqn. (1.4).

Equation (1.5) can be rewritten as (Cao and Faghri, 1992a)

$$\ln(T_{tr} \rho R / p_{rf}) + \frac{h_{fg}}{R} \left(\frac{1}{T_{tr}} - \frac{1}{T_{rf}} \right) = 0 \quad (1.6)$$

and solved iteratively for T_{tr} using the Newton-Raphson/secant method (Pletcher et al., 1988).

Figure 1.4 shows the transition temperature for a sodium heat pipe as a function of minimum vapor space dimension. When the minimum vapor space di-

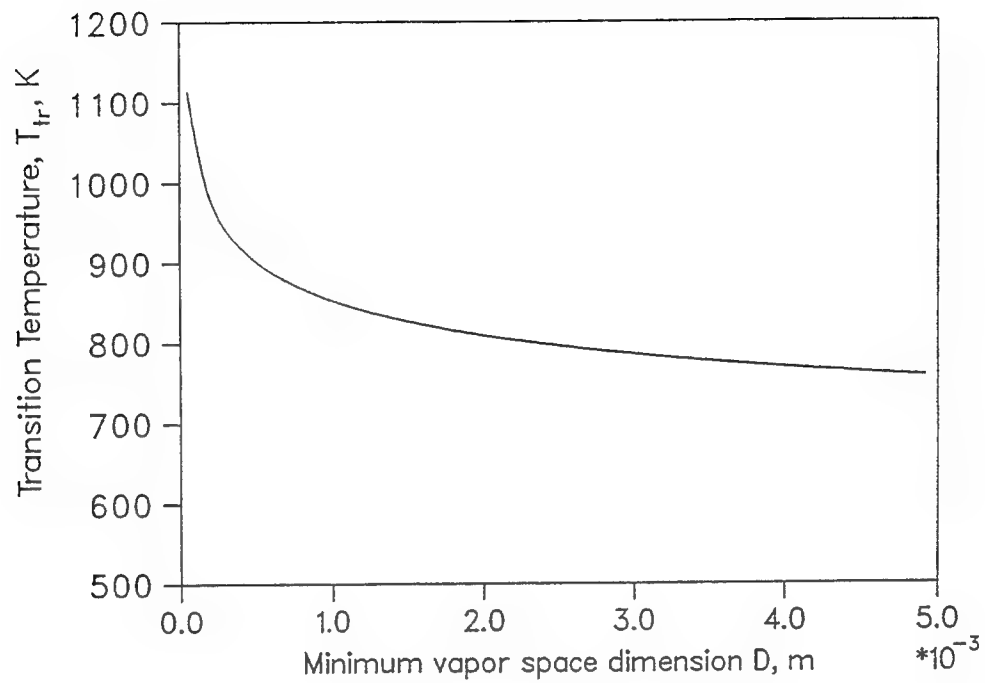


Figure 1.4: Transition temperature for sodium as the heat pipe working fluid (Cao and Faghri, 1994)

mension reduces to less than 1 mm, the transition temperature rises sharply. A higher transition temperature will make the startup of the heat pipe from the frozen state more difficult. However, even at a minimum vapor space of 50 μm , the transition temperature is nearly 1100 K, which is in the normal operating temperature range of 800 to 1400 K. This means that once the heat pipe startup is completed, the micro heat pipe will be operational in the upper operating temperature range.

Figure 1.5 shows the transition temperatures for water and methanol as heat pipe working fluids. As the minimum vapor space dimension approaches the micro heat pipe range ($D < 100 \mu\text{m}$), the transition temperature for water rises to more than 50°C. In this case, a micro heat pipe with water as the working fluid is apparently not suitable for cooling electronic devices, which work at temperatures preferably lower than 50°C. Even if the working temperature of the micro heat pipe is higher than the transition temperature, when a electronic device starts up from the room temperature, the heat pipe will temporarily experience the rarefied or free molecular vapor flow stage, in which the temperature gradient in the axial direction is substantially higher than that of the normal working condition. This continuum limitation is less severe for methanol as the working fluid. At a minimum vapor space $D = 50 \mu\text{m}$, the transition temperature is only about 20°C. However, the vapor pressure of methanol is higher than that of water. At a working temperature of about 80°C, for example, the vapor pressure of methanol is about $1.72 \times 10^5 \text{ Pa}$, in

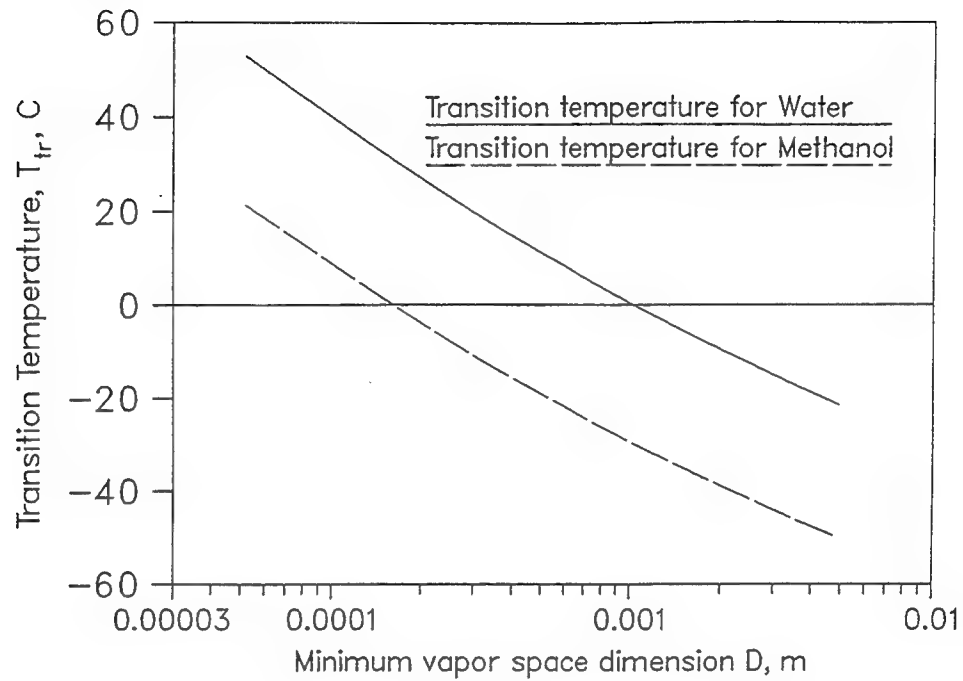


Figure 1.5: Transition temperatures for water and methanol as heat pipe working fluids (Cao and Faghri, 1994)

comparison with the vapor pressure of about 0.47×10^5 Pa for water. A working vapor pressure higher than the ambient pressure may result in additional structural requirements for the silicon chip.

Boiling Limitation

The critical temperature drop across the heat pipe wick for the boiling limit is (Cao and Faghri, 1992b)

$$\Delta T_{\text{crit}} = T_s - T_v = \frac{R T_v T_s}{h_{fg}} \ln \left[1 + \frac{2\sigma}{p_v} \left(\frac{1}{r_b} - \frac{1}{R_m} \right) + \frac{2\sigma \rho_v}{p_v r_b \rho_l} \right] \quad (1.7)$$

where T_s is the wall-liquid interface temperature, T_v is the heat pipe vapor temperature, r_b is the effective radius of small vapor or noncondensable gas bubbles trapped at the inner wall, and R_m is the radius of the liquid-vapor meniscus. For the wickless micro heat pipe, ΔT_{crit} is the critical temperature drop across the liquid film. Since $T_s = T_v + \Delta T_{\text{crit}}$, eqn. (1.7) can be written as

$$\Delta T_{\text{crit}} = \frac{\left\{ \frac{R T_v^2}{h_{fg}} \ln \left[1 + \frac{2\sigma}{p_v} \left(\frac{1}{r_b} - \frac{1}{R_m} \right) + \frac{2\sigma \rho_v}{p_v r_b \rho_l} \right] \right\}}{\left\{ 1 - \frac{R T_v}{h_{fg}} \ln \left[1 + \frac{2\sigma}{p_v} \left(\frac{1}{r_b} - \frac{1}{R_m} \right) + \frac{2\sigma \rho_v}{p_v r_b \rho_l} \right] \right\}} \quad (1.8)$$

The maximum heat flux related to the boiling limit, assuming heat conduction is dominant in the thin liquid film, is given by

$$q_{\text{crit}} = k_\ell \Delta T_{\text{crit}} / \delta \quad (1.9)$$

It can be seen from eqns. (1.8) and (1.9) that the critical heat flux strongly depends on the heat pipe working condition. The dominant term in eqn. (1.8) is $2\sigma(1/r_b - 1/R_m)/p_v$. For a fixed r_b , a higher vapor temperature results in a much higher vapor pressure p_v , and therefore a much lower critical heat flux. Since for many mainframe computers, the maximum operating junction temperature for functionality is about 80°C, the boiling limit was examined under this working temperature. Figure 1.6 shows the boiling limits as a function of liquid thickness δ at $T_v = 80^\circ\text{C}$ and $r_b = 2.54 \times 10^{-7}\text{m}$. For water as the working fluid, the critical heat flux is generally high for most of the range of δ in the figure.

For a larger liquid film thickness ($\delta > 5 \times 10^{-5}\text{ m}$), however, the critical heat flux drops below 100 W/cm². For methanol as the working fluid, the critical heat flux is generally low. When the film thickness becomes larger, the critical heat flux even drops to below 10 W/cm². In the above calculation, the radius of the liquid-vapor meniscus was assumed to be much larger than r_b , and its effect on the critical heat flux was neglected. For high temperature heat pipes with liquid metal working fluids, the boiling limit rarely occurs (Cao and Faghri, 1992b), so it was not considered here.

The boiling limit also largely depends on the effective radius of small vapor or noncondensable gas bubbles, r_b . Figure 1.7 presents the boiling limits as a function of r_b for $T_v = 80^\circ\text{C}$ and $\delta = 10^{-5}\text{ m}$. Both critical heat fluxes for water and methanol drop to low values for relatively larger r_b , even for a relatively thin liquid

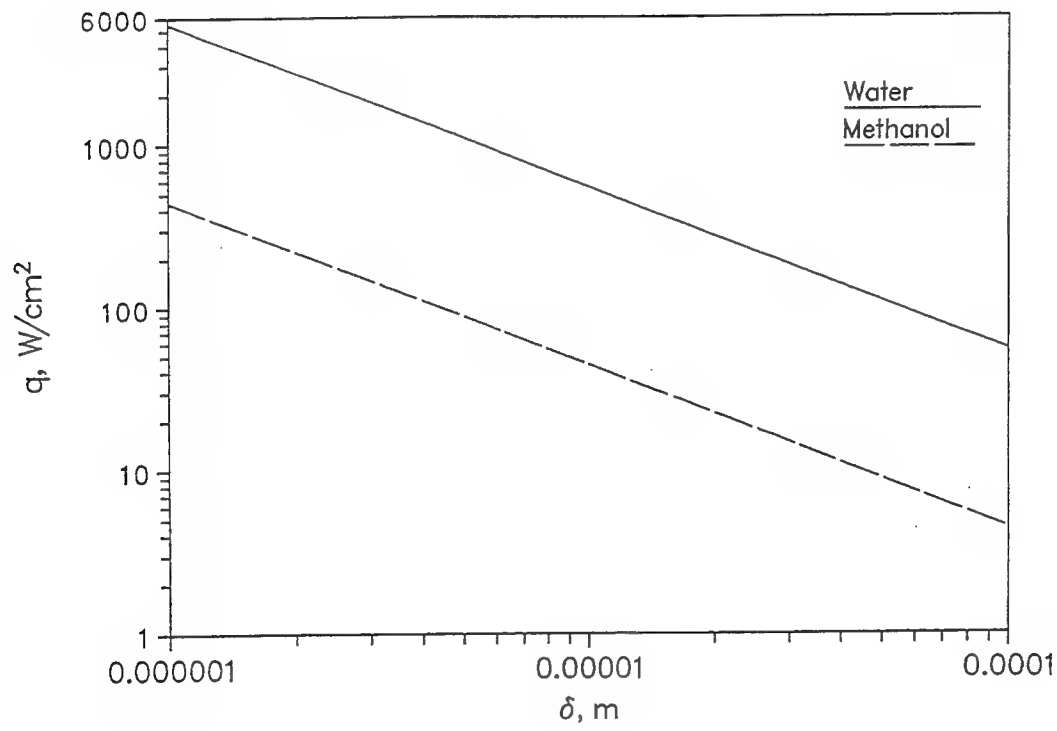


Figure 1.6: Boiling limits as a function of liquid thickness for $T_v = 80^\circ\text{C}$, $R_b = 2.54 \times 10^{-7}$ m (Cao and Faghri, 1994)

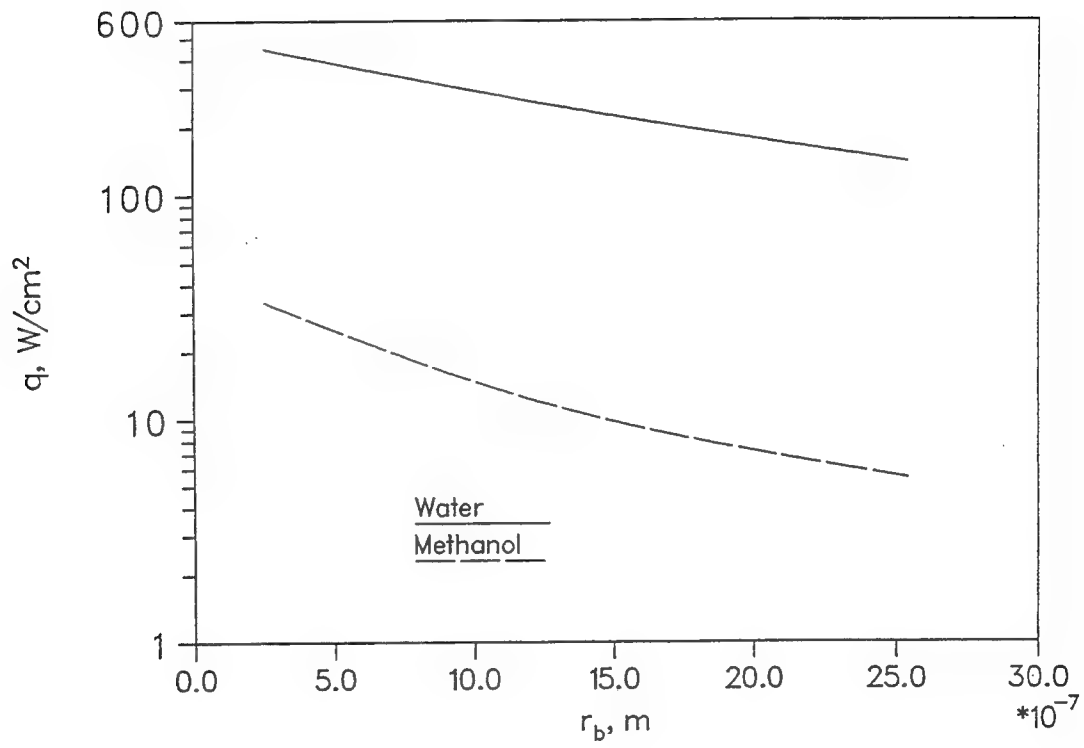


Figure 1.7: Boiling limits as a function of R_b for $T_v = 80^\circ\text{C}$, $\delta = 10^{-5} \text{ m}$ (Cao and Faghri, 1994)

film thickness. To reduce the value of r_b , complete cleaning and degassing of the heat pipe inner wall surface are needed. Since the vapor space of a micro heat pipe is very small, difficulties related to the heat pipe cleaning and degassing are expected.

1.4 Capillary Limitation

Like conventional heat pipes, the capillary limit remains one of the major operating limits for miniature and micro heat pipe designs. Cotter (1984) pointed out that the heat transport capacity of micro heat pipes depends more critically on the volume of working fluid available than conventional heat pipes with wicks. The mean radius of curvature R is given by

$$\frac{1}{R} = \frac{1}{R_1} + \frac{1}{R_2} \quad (1.10)$$

where R_1 and R_2 are two principal radii of curvature for the surface. If the surface tension is denoted by σ , and the pressures in the liquid and vapor are p_ℓ and p_v , then

$$p_v - p_\ell = \frac{\sigma}{R} \quad (1.11)$$

$$\frac{d}{dz}(p_v - p_\ell) = \frac{d}{dz} \left(\frac{\sigma}{R} \right) \quad (1.12)$$

The approximate maximum heat transport for steady-state derived by Cot-

ter (1984), including the use of eqn. (1.12), is

$$Q_{\max} = \left(\frac{0.16\beta (K_\ell/K_v)^{1/2}}{8 \pi H(1)} \right) \left(\frac{\sigma h_{fg}}{\nu_\ell} \right) \left(\frac{\nu_\ell}{\nu_v} \right)^{1/2} \left(\frac{A^{0.75}}{L_t} \right) \quad (1.13)$$

where K_ℓ and K_v are the flow shape factors, $H(1)$ is an integral over the length of the pipe as given by Cotter (1984), A is the total cross sectional area of the heat pipe, and β is a dimensionless geometrical factor. As an illustrative case, Cotter (1984) considered a micro heat pipe with an equilateral triangular cross section filled with the optimum amount of methanol to operate at 50°C with a uniformly heated evaporator and uniformly cooled condenser. For a triangular pipe with a side of 0.02 cm and a length of 1 cm, the maximum heat transport Q_{\max} was found to be 0.03 W. If placed closely together on a surface, micro heat pipes of this size could provide a few watts per square centimeter of cooling. Cotter concluded that micro heat pipes are candidates for thermal control of micromechanical and microelectronic devices in cases where thermal loads are modest, and where a high standard of temperature constancy and uniformity are required.

Babin et al. (1989) compared the maximum heat transport (Q_{\max} , eqn. (1.13)) from Cotter (1984), with their experimental data related to the capillary limit. They found that eqn. (1.13) underpredicted the heat transport limit substantially, especially when the operating temperature was relatively high. The maximum heat transport relation based on the conventional larger heat pipe was also presented

and compared with related experimental data by Babin et al. (1989). Unlike the micro heat pipe, the conventional method involves defining vapor pressure and liquid pressure separately, and then combining them to obtain the maximum heat flux. The relation obtained by Babin et al. (1989) based on Chi (1976) is

$$Q_{\max} = \frac{2\sigma/r_{\text{eff}} - \rho_{\ell}gL_t \sin \varphi}{L_{\text{eff}} \left[\frac{\mu_{\ell}}{KA_g h_{fg} \rho_{\ell}} + \frac{C(f_v Re_v) \mu_v}{2(r_{h,v})^2 A_v \rho_v h_{fg}} \right]} \quad (1.14)$$

where φ is the heat pipe tilt angle, K is the wick permeability, $r_{h,v}$ is the hydraulic radius of the vapor space, and C is a modification coefficient. The values of C and $f_v Re_v$ depend on the vapor flow regime. Good agreement was obtained between eqn. (1.14) and the related experimental data (Babin et al., 1989). The agreement may be due to the relatively large size of the heat pipe tested. Experimental data related to actual micro heat pipes are needed for further examination of eqns. (1.13) and (1.14).

Gerner et al. (1992) derived a correlation for the maximum heat transport in the form

$$Q_{\max} = C \frac{3\pi}{2048} \frac{\sigma h_{fg}}{\nu_v L_t} D_h^3 \quad (1.15)$$

The constant C was determined, using the experimental data from Babin et al. (1989), to be 2.38. Therefore, eqn. (1.15) can be written as

$$Q_{\max} = 0.01 \frac{\sigma h_{fg} D_h^3}{\nu_v L_t} \quad (1.16)$$

For a water heat pipe with hydraulic diameter of 100 μm and length of 2.54 cm, for example, heat transport on the order of 1 mW can be expected per device. If 127 of these micro heat pipes per inch are used, and assuming that all of the energy is transferred through the end of the evaporator, a heat flux up to 15 W/cm² can be dissipated under a working temperature of 70°C (Gerner et al., 1992).

Since micro heat pipes are very small, the evaporation in the liquid “micro-layer” region may play a role during heat transfer in micro heat pipes. The microlayer region is also referred to as the contact line region. A thin film of liquid on a horizontal solid surface is schematically shown in Fig. 1.8. For a very thin film on the surface, the pressure gradient for the liquid flow is due to the conventional capillary force and the disjoining pressure, which results from the repulsion of the vapor phase by the solid and the liquid from long range intermolecular forces. The chemical potential of an evaporating thin film differs from that of the bulk liquid by an amount often referred to as the excess potential due to the solid/liquid/vapor intermolecular force field. This potential is defined in units of pressure (disjoining pressure). The pressure change at the liquid-vapor interface is (Schonberg and Wayner, 1990; Dasgupta et al., 1991)

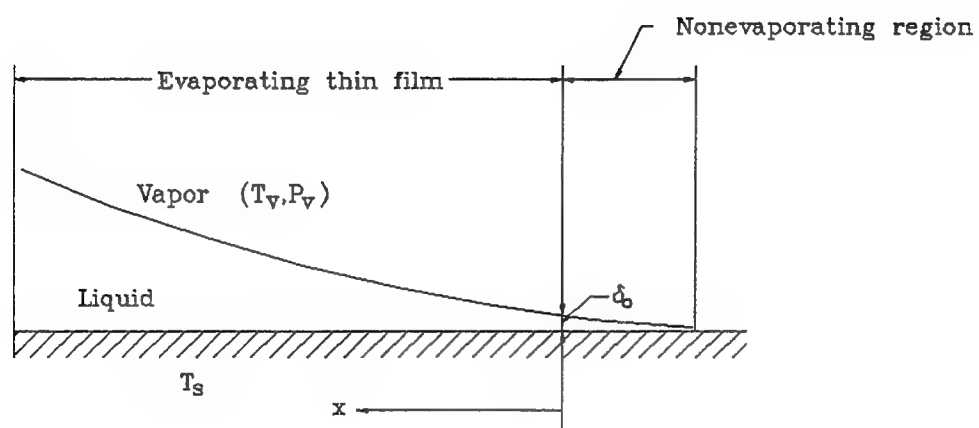


Figure 1.8: Evaporating, nonevaporating regions and coordinate system (not to scale)

$$p_v - p_\ell = \frac{\bar{A}}{\delta^3} + \sigma K_c \quad (1.17)$$

where $\bar{A} = A/6\pi$, A is the Hamaker constant, σ is the surface tension, and K_c is the curvature of the interface. When the liquid film is thin with a relatively flat surface, the second term in eqn. (1.17) can always be neglected compared to the first term. For a very thin film, $\delta \leq \delta_0$, where δ_0 is the nonevaporating film thickness shown in Fig. 1.8, a thin film region persists at equilibrium with its saturated vapor, even though it is superheated. The film does not evaporate due to the reduced vapor pressure of the film caused by the disjoining pressure. This region is called the nonevaporating region where $\delta \leq \delta_0$. Beyond this region is the microlayer region where evaporation and liquid flow occur. The mass flux of vapor leaving the liquid/vapor interface is modeled as (Schonberg and Wayner, 1990)

$$\dot{m}' = a (T_{\ell v} - T_v) + b (p_\ell - p_v) \quad (1.18)$$

where

$$a = 2.0 \left(\frac{M}{2\pi R T_{\ell v}} \right)^{1/2} \left(\frac{p_v M h_{fg}}{R T_v T_{\ell v}} \right)$$

$$b = 2.0 \left(\frac{M}{2\pi R T_{\ell v}} \right)^{1/2} \left(\frac{V_\ell p_v}{R T_{\ell v}} \right)$$

$T_{\ell v}$ is the temperature of the liquid at the liquid-vapor interface, and V_ℓ is the molar volume of the liquid. A closed-form solution for the dimensionless integral contact line heat sink was obtained by neglecting the interface curvature and applying the lubrication theory related to the mass flow in the thin film (Schonberg and Wayner, 1990)

$$Q^* = [18(1 + \lambda^3) \ln \left[\frac{\eta(1 + \lambda)}{1 + \lambda\eta} \right] + 6(\eta^{-3} - 1) + 9\lambda(1 - \eta^{-2}) + 18\lambda^2(\eta^{-1} - 1)]^{1/2} \quad (1.19)$$

The integral heat sink for the contact line region, which is defined as the heat absorbed by the microlayer region between $\eta = 1$ and η , is directly related to Q^* , which is

$$Q = \frac{\bar{A}_{hfg}}{3\nu_\ell x_o} Q^* \quad (1.20)$$

where

$$\lambda = \frac{a h_{fg} \delta_0}{k} \quad (1.21)$$

$$\eta = \frac{\delta}{\delta_0} \quad (1.22)$$

$$x_o = \frac{\bar{A}}{\nu_\ell a \Delta T} \quad (1.23)$$

$$\delta_0 = \left(\frac{bA'}{a\Delta T} \right)^{1/3} \quad (1.24)$$

$$\Delta T = T_s - T_v \quad (1.25)$$

Figure 1.9 presents Q^* as a function of η for sodium, water and methanol as heat pipe working fluids. For relatively large values of $\eta = \delta/\delta_0$, Q^* approaches a constant, which is the maximum dimensionless contact line heat sink Q_{\max}^* . Q_{\max}^* corresponds to a maximum dimensionless liquid film thickness, η_{\max} , in the microlayer region in which the capillary pressure is negligible. The corresponding maximum liquid film thickness is

$$\delta_{\max} = \eta_{\max} \delta_0 \quad (1.26)$$

From Fig. 1.9, the maximum thickness of the microlayer is on the order of $0.5 \sim 1.0 \mu\text{m}$. For a micro heat pipe with hydraulic radius on the order of $10 \mu\text{m}$, the liquid film thickness in the axial direction close to the evaporator end cap should be on the order of $1 \mu\text{m}$, which is in the microlayer region. Therefore, the disjoining pressure may help to draw liquid toward the evaporator end cap and increase heat transport capacity. In the circumferential direction, as shown in Fig. 1.10 for a micro heat pipe with a triangular cross section, the disjoining pressure may help to spread liquid from the corners to the rest of the inner wall surface and improve the cooling condition at

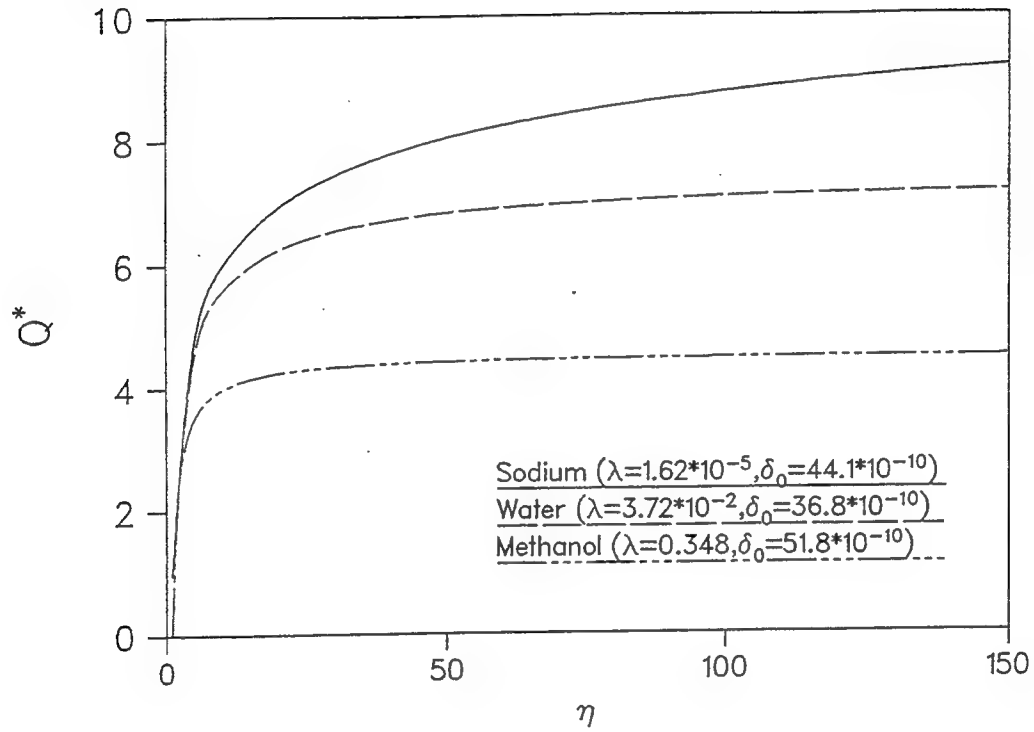


Figure 1.9: Dimensionless heat sink as a function of working fluids for $\Delta T = 0.1^\circ\text{C}$

(Cao and Faghri, 1994)

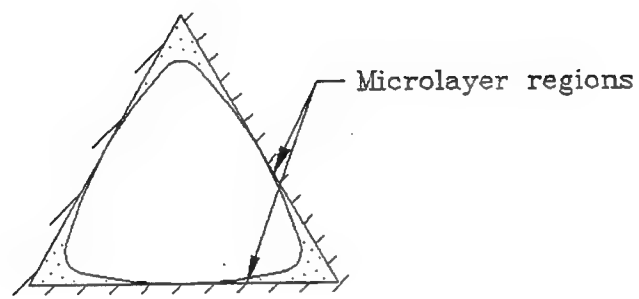


Figure 1.10: Schematic of liquid film distributions in the micro heat pipe

the evaporator. As a result, the heat transport capacity for a micro heat pipe may be somewhat larger than the capillary limit derived based on conventional larger heat pipes. It should be pointed out that the above arguments are based on a simplified theory, and are qualitative in nature. A detailed experimental study is needed for estimating the increase in the heat transport capacity quantitatively.

1.5 Conclusions and Remarks

The literature review revealed that the miniature flat heat pipes developed by Plesch et al. (1991) and other investigators were capable of removing heat fluxes as high as 60 W/cm^2 under the thermal siphon operating mode. The maximum heat flux obtainable may be further increased by optimizing the longitudinal grooves on the inner flat surface. Further performance improvements can also be made by reducing the contact resistance between the heat pipe and the electronic chip. Since micro electronic components are shaped as thin plates with flat base surfaces, and the heat resistance in the transverse direction is small due to the high thermal conductivity of silicon (on the order of 100 W/(m-K)), most of the heat generated in the electronic component can be transferred to the flat heat pipe and dissipated via the heat pipe condenser without causing large temperature gradients in the electronic component. For the current highest chip heat fluxes on the order of 60 W/cm^2 , these miniature flat heat pipes can be expected to have a large commercial application.

As the size of the heat pipe decreases, the micro heat pipe may encounter the vapor continuum limitation. This limitation may prevent the micro heat pipe from working under lower temperatures. For a heat pipe operating at higher working temperatures, this limitation is temporary and will disappear when the heat pipe temperature increases. In addition to the vapor continuum limitation, the micro heat pipe is also subject to the operating limits of the conventional heat pipe. Of these operating limits, the capillary limit remains the most important for the micro heat pipe. The maximum heat flux based on the conventional formulation is on the order of 10 W/cm^2 , which is relatively low. However, since the size of micro heat pipes is very small, the disjoining pressure may help to increase the heat transport capacity of the heat pipe. Further study is needed to quantify this effect. Finally, in order for micro heat pipes to find commercial application in microelectronic cooling, it must compete with other cooling methods such as forced convection, impingement and two-phase direct cooling in areas such as manufacturing cost and reliability. Because of the extremely small dimension of micro heat pipes, difficulties in manufacturing and the subsequent cleaning and degassing are expected. Furthermore, the "true" micro heat pipe built directly into the silicon must compete with the miniature heat pipe attached on the chip surface in this area, which is much less costly. Also, the operating conditions of the miniature heat pipe could be further improved by reducing the contact resistance between the heat pipe and the electronic chip.

Chapter 2

THERMAL ANALYSIS OF A MICRO HEAT PIPE

2.1 Summary

A detailed mathematical model is developed in which the heat and mass transfer processes in a micro heat pipe (MHP) are examined. The model describes the distribution of the liquid in an MHP and its thermal characteristics depending upon the liquid charge and the applied heat load. The liquid flow in the triangular-shaped corners of an MHP with polygonal cross section is considered by accounting for the variation of the curvature of the free liquid surface and the interfacial shear stresses due to liquid-vapor frictional interaction. The predicted results obtained are compared to existing

experimental data. The importance of the liquid fill, minimum wetting contact angle, and the shear stresses at the liquid-vapor interface in predicting the maximum heat transfer capacity and thermal resistance of the MHP is demonstrated.

2.2 Introduction

In an MHP, condensate return is accomplished by the flow of liquid in the corners of the polygonal heat pipe container; the condensate being held in the corners by surface tension. The objective of the present study is to develop a mathematical model which can determine the maximum heat capacity and thermal resistance of MHPs. The present model incorporates the following new features:

- The influence of the liquid charge on the length of the liquid blocking zone and on the liquid distribution.
- The heat transfer through a liquid film in the evaporator is described with respect to the disjoining pressure.
- The heat transfer through a film of condensate in the condenser is considered and the closed-form solutions are obtained using an approach similar to that developed for axially-grooved heat pipes.
- The influence of shear stresses at the free liquid surface in a corner due to the frictional vapor-liquid interaction on the liquid flow is taken into consideration.

- The possibility of the variation of the meniscus contact angle in the condenser is treated by considering the condensate film formation.
- The model describes MHP operation in the case of convective heat transfer outside the evaporator and condenser as well as that for a prescribed heat flux distribution.

2.3 Mathematical Model

The present model deals with a polygonal MHP having N triangular corners, which can easily be extended for cross sections having different corner configurations. Figure 2.1 presents cross sections of the triangular micro heat pipe used to illustrate the methodology of the present study. The heat load is uniformly distributed between all of the corners. Near the evaporator end cap, if the heat load is sufficient, the liquid meniscus is depressed in the corner, and its cross sectional area and radius of curvature of the free surface are extremely small. Most of the wall is dry or is covered by a nonevaporating liquid film. In the adiabatic section, the liquid cross sectional area is comparatively larger. The inner wall surface may be covered with a thin liquid film due to the disjoining pressure. At the beginning of the condenser, a film of condensate is present on the wall, and liquid flows through this film toward the meniscus region under the influence of surface tension. For normal operation, the

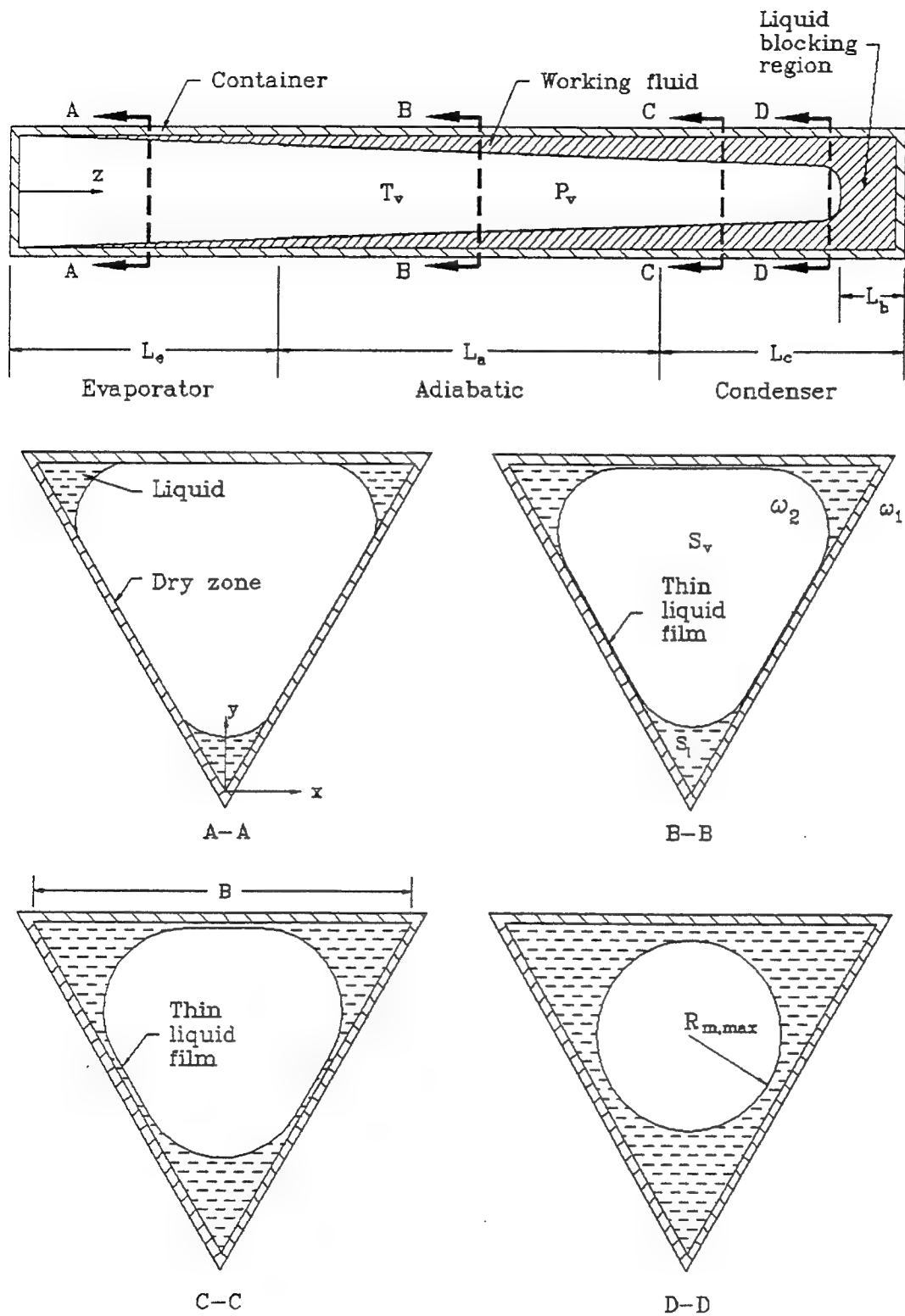


Figure 2.1: Schematic of the micro heat pipe and coordinate systems for analysis

contact angle of the meniscus θ is constant and equal to the minimum wetting contact angle θ_0 in the evaporator and adiabatic sections and the beginning of the condenser zone, which is fixed for a specific working-fluid/container combination. In Fig. 2.1, the possibility of liquid blocking the end of the condenser is shown. The details of the evaporator and condenser sections are shown in Fig. 2.2.

The fluid flow and heat transfer within a micro heat pipe operating under steady-state conditions are modeled, neglecting axial heat conduction in the wall and liquid. The conservation equations for the steady-state operation of an MHP are the continuity, momentum and energy equations for the liquid, vapor and wall, and the Laplace-Young equation for the radius of curvature at the liquid-vapor interface. At any axial location, the following mass conservation equation must hold over the cross section of the MHP:

$$\bar{w}_v \rho_v A_v = N \bar{w}_\ell \rho_\ell A_\ell \equiv N \dot{m}_\ell \quad (2.1)$$

where \dot{m}_ℓ is the mass flow rate through a corner. The average liquid and vapor velocities in the axial direction in Eq. 2.1 are:

$$\bar{w}_\ell = \frac{1}{A_\ell} \int \int_{A_\ell} w_\ell(x, y) dx dy, \quad \bar{w}_v = \frac{1}{A_v} \int \int_{A_v} w_v(x, y) dx dy \quad (2.2)$$

A MHP contains a definite amount of a working fluid M_t , which is distributed in accordance to the following relation:

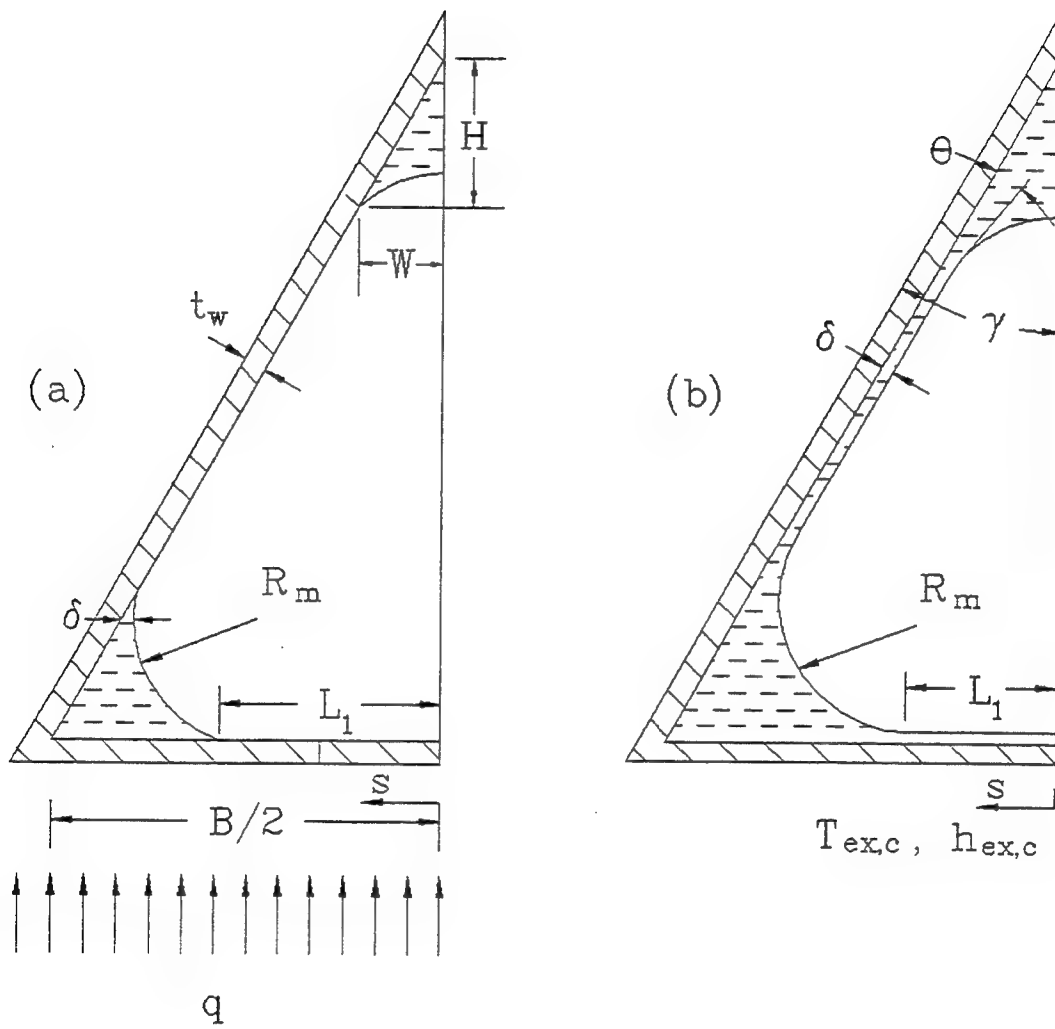


Figure 2.2: Details of the micro heat pipe cross section in (a) the evaporator, (b) the condenser

$$M_t = N \int_0^{L_t-L_b} \rho_\ell A_\ell dz + \int_0^{L_t-L_b} \rho_v A_v dz + M_b + M_\delta \quad (2.3)$$

where M_b and L_b are the mass and length of the liquid which blocks the condenser, and M_δ is the mass of the thin liquid films in the condenser and adiabatic sections in the interval $0 \leq s \leq L_1$ (see Fig. 2.2(b)) for all of the MHP walls, while A_ℓ doesn't include the thin film existing in this interval. It is anticipated that the excessive liquid, the amount of which depends upon the operating conditions, is contained at the end of the condenser because of the MHP small inner diameter and the effect of the vapor flow on the liquid (Fig. 2.1).

The axial conservation of momentum equation for an incompressible vapor flow using the one-dimensional boundary-layer approximation is:

$$\frac{d}{dz}(P_v + \rho_v g z \sin \varphi + \rho_v \beta_v \bar{w}_v^2) = -f_v \frac{2\rho_v \bar{w}_v^2}{D_{h,v}} \quad (2.4)$$

where β_v is the momentum flux coefficient, f_v is the friction coefficient, and $D_{h,v}$ is the hydraulic diameter of the vapor channel. The values of these coefficients can be determined using the results of previous investigators for the two-dimensional, laminar boundary-layer equations with suction and injection. For example, for the small radial Reynolds numbers usually seen in MHPs ($0 \leq \text{Re}_r < 2$), in the evaporator and adiabatic sections, the results given by Bankston and Smith (1972) can be approximated as follows:

$$f_v = \left(\frac{16 + 0.25\text{Re}_r^2}{\text{Re}} \right), \quad \beta_v = 1.33 - 0.0075\text{Re}_r^2$$

In the condenser section (Bowman and Hitchcock, 1988; Jang et al., 1991):

$$f_v = 16[1.2337 - 0.2337\exp(-0.0363\text{Re}_r)][\exp(1.2\text{Ma})]/\text{Re}, \quad \beta_v = 1.33$$

The velocity of the liquid phase is very small in comparison to that of the vapor flow, so the interfacial shear for the vapor is computed by assuming the liquid to be stationary (Longtin et al., 1992).

The axial transport of condensate in an MHP takes place in the corners, where most of the liquid resides. The thickness of the liquid films in the condenser and adiabatic sections in the interval $0 \leq s \leq L_1$ (see Fig. 2.2(b)) is assumed to be too small to contribute to the axial mass transport. Since the axial Reynolds number for liquid flow in an MHP is usually less than 1, it can be considered to be viscous and quasi-one-dimensional. Thus, the conservation of momentum equation for the liquid flow in a corner with cross sectional area A_ℓ is:

$$\frac{dP_\ell}{dz} + \frac{\rho_\ell}{2A_\ell} \frac{d}{dz}(\bar{w}_\ell^2 A_\ell) + \rho_\ell g \sin \varphi = \mu_\ell \left(\frac{\partial^2 w_\ell}{\partial x^2} + \frac{\partial^2 w_\ell}{\partial y^2} \right) \quad (2.5)$$

The second term in Eq. 2.5 is the contributions of the dynamic component of the flow rate and the axial variation of the cross sectional area on the liquid pressure gradient.

The present numerical results have shown that this term changes the liquid pressure gradient by less than 0.1 percent.

The conservation of energy equation is cast into a form which reflects the change in the axial mass flow rate of liquid due to evaporation and condensation:

$$\frac{d}{dz}(\rho_\ell \bar{w}_\ell A_\ell) = \begin{cases} \frac{B}{h_{fg}} h_{ex,e} (T_{ex,e} - T_v) \left(1 + \frac{h_{ex,e}}{\bar{h}_e}\right)^{-1}, & 0 \leq z \leq L_e \\ 0 & \text{(adiabatic section)} \quad L_e < z < L_e + L_a \\ \frac{B}{h_{fg}} h_{ex,c} (T_{ex,c} - T_v) \left(1 + \frac{h_{ex,c}}{\bar{h}_c}\right)^{-1}, & L_e + L_a \leq z \leq L_t - L_b \end{cases} \quad (2.6)$$

where \bar{h}_e and \bar{h}_c are the mean internal heat transfer coefficients between the wall and vapor, and $h_{ex,e}$ and $h_{ex,c}$ are the heat transfer coefficients between the wall and the ambient. The mean coefficients \bar{h}_e and \bar{h}_c for evaporation and condensation, respectively, include the resistances of the wall and liquid film, which are given by the heat transfer analysis for each of the heat loaded sections at every point on z . The vapor temperature is denoted by T_v . For a given axial heat load function $Q(z)$, Eq. 2.6 can be rewritten as:

$$\frac{d}{dz}(\rho_\ell \bar{w}_\ell A_\ell) = \frac{1}{h_{fg} N} \frac{dQ(z)}{dz} \quad (2.7)$$

For the case of radiative heat transfer in the condenser region, the heat transfer coefficient in Eq. 2.6 is:

$$h_{ex,c} = \sigma_0 \epsilon (T_v + T_{ex,c})(T_v^2 + T_{ex,c}^2) \quad (2.8)$$

An iterative procedure can be used to determine $h_{ex,c}$ from Eq. 2.8, since it is a strong function of T_v in the case of a radiative boundary condition.

The interfacial meniscus radius of curvature is related to the pressure difference between the liquid and vapor by the Laplace-Young equation, which, in differential form, is:

$$\frac{dP_\ell}{dz} = \frac{dP_v}{dz} - \frac{d}{dz} \left(\frac{\sigma}{R_m} \right) \quad (2.9)$$

The vapor temperature and pressure are related by the perfect gas equation:

$$P_v = \rho_v R_g T_v \quad (2.10)$$

Equation 2.10 is accurate enough for comparatively low pressure values for the conditions considered in the present study (the maximum error value was 0.73%). However, in the general case, one should use an empirical equation based on saturation conditions and the Clausius-Clapeyron equation instead of Eq. 2.10.

The mean axial liquid and vapor velocities at the evaporator and condenser end caps are:

$$\bar{w}_\ell|_{z=0} = \bar{w}_v|_{z=0} = 0 \quad (2.11)$$

$$\overline{w}_\ell|_{z=L_t-L_b} = \overline{w}_v|_{z=L_t-L_b} = 0 \quad (2.12)$$

Referring to Fig. 2.1, the liquid in the corner is attached to two walls, ω_1 , and interacts with the vapor flow at the liquid-vapor interface, ω_2 . Therefore, the no-slip condition and relation for the equality of tangential shear stress on these surfaces are:

$$w_\ell|_{\omega_1} = 0; \quad \left. \frac{\partial w_\ell}{\partial n} \right|_{\omega_2} = -\frac{f_v}{2\mu_\ell} \rho_v \overline{w}_v^2 \quad (2.13)$$

The second boundary condition in Eq. 2.13 is an essential feature of the present model. Here n is the normal vector on the free surface of the liquid meniscus. The cross section of the vapor channel has a complicated shape and the assumption of a circular cross section is not completely exact for $N \leq 3$, but it is very close for $N > 3$, where the vapor channel is nearly circular.

The vapor and liquid pressures at the evaporator end cap are:

$$P_v|_{z=0} = P_{v0}, \quad P_\ell|_{z=0} = P_{v0} - \frac{\sigma}{R_{m0}} \quad (2.14)$$

The values of P_{v0} and R_{m0} are to be determined using additional conditions. When solving Eq. 2.6, where $T_v(z)$ is also unknown and depends on P_v , the value of P_{v0} must be chosen such as to satisfy Eq. 2.12. When $Q(z)$ and T_{v0} are known, $P_{v0} = P_v(T_{v0})$, which can be obtained using the perfect gas law, Eq. 2.10. The radius of curvature of the meniscus at the evaporator end cap, R_{m0} , is found using Eq. 2.3, since the value

of R_{m0} influences the axial distribution of liquid. In general, the radius of curvature of the meniscus is bounded by $R_{m,\min} \leq R_{m0} \leq R_{m,\max}$. When liquid blocks part of the condenser section, R_{m0} is specified such that $R_m \simeq R_{m,\max}$ at the location where the liquid blocking begins, where $R_{m,\max}$ is approximately the radius of the largest circle which can be inserted in the inner MHP cross section, (Fig. 2.1). For the case in which no liquid blocks the condenser, the value of R_{m0} is given by Eq. 2.3 where $M_b = 0$ and $L_b = 0$, or $R_{m0} = R_{m,\min}$ when $Q_a = Q_{\max}$.

To determine the heat transfer coefficients \bar{h}_e and \bar{h}_c in Eq. 2.6, the heat transfer during evaporation and condensation in a triangular capillary groove is examined.

2.4 Heat Transfer in the Condenser Section

The equation for the condensate film thickness distribution, $\delta(s)$, shown in Figs. 2.1 and 2.2, is given by Kamotani (1976a) for a low-temperature heat pipe with axial grooves:

$$\frac{\rho_\ell \sigma \delta^3}{3\mu_\ell} \frac{d^3\delta}{ds^3} = \frac{k_\ell(T_v - T_w)}{h_{fg}} \int_0^s \frac{ds}{\delta} \quad (2.15)$$

For the case of a polygonal MHP, the boundary conditions are:

$$\left. \frac{d\delta}{ds} \right|_{s=0} = 0; \quad \left. \frac{d^3\delta}{ds^3} \right|_{s=0} = 0; \quad \left. \frac{d^2\delta}{ds^2} \right|_{s=L_1} = \frac{1}{R_m}; \quad \left. \frac{d\delta}{ds} \right|_{s=L_1} = \tan \theta \quad (2.16)$$

Equation 2.15 has been derived from the conservation of mass, momentum and energy equations for the flow of a thin film and the relation between the thickness and the curvature. The interfacial thermal resistance is usually neglected in comparison to the resistance of the liquid film, but it can be accounted for in the expression for the condenser heat resistance. Equation 2.15 can be solved for the film thickness by numerical methods. In the present paper, however, an approximate closed-form solution is obtained using the assumption that the liquid film thickness variation along the s -direction is small in comparison to its thickness; i.e., the film is assumed to be nearly planar. The film thickness in the middle region of the wall (see Fig. 2.2(b)) can be approximated by:

$$\frac{\delta}{B} = C_0 + C_1 \frac{s}{B} + C_2 \frac{s^2}{B^2} + C_3 \frac{s^3}{B^3} + C_4 \frac{s^4}{B^4} \quad (2.17)$$

From the boundary conditions in Eq. 2.16, the coefficients are:

$$C_1 = C_3 = 0; \quad C_4 = \frac{L_1/R_m - \tan \theta}{8(L_1/B)^3}, \quad C_2 = \frac{B}{2R_m} - 6 \left[\frac{L_1}{B} \right]^2 C_4 \quad (2.18)$$

The value of C_0 is obtained by differentiating Eq. 2.15, inserting Eq. 2.17 and neglecting the term which contains the first derivative of δ . The mean heat transfer

coefficient of the thin film region, $\bar{h}_{c,f} = k_\ell / \bar{\delta}$, is approximated as:

$$\bar{h}_{c,f} = \frac{k_\ell}{BC_0} = \left[\frac{h_{fg} \rho_\ell \sigma k_\ell^3 (L_1/R_m - \tan \theta)}{\mu_\ell L_1^3 (T_v - T_w)} \right]^{0.25} \quad (2.19)$$

From Fig. 2.2(b), the value of L_1 is defined as:

$$L_1 = \frac{B}{2} - R_m \frac{\cos(\gamma + \theta)}{\sin \gamma} - \frac{C_0}{\tan \gamma} B \quad (2.20)$$

Equations 2.19 and 2.20 are solved for C_0 and L_1 using an iterative procedure. The increase of the liquid film thickness along the s coordinate in the interval $s = 0$ to $s = L_1$ in the numerical experiments is less than 8.0 percent, so Eq. 2.19, where it is assumed that $\bar{\delta} = BC_0$, gives $\bar{h}_{c,f}$ to within 4.0 percent.

The heat transfer coefficient in the meniscus region can be estimated as follows. For $s > L_1$, the film thickness increases sharply (see Fig. 2.2(b)):

$$\delta = \delta|_{s=L_1} - R_m + \left[R_m^2 + (s - L_1)^2 + 2(s - L_1)R_m \sin \theta \right]^{0.5} \quad (2.21)$$

Then, for the mean heat transfer coefficient in the meniscus region, $\bar{h}_{c,men}$, we have:

$$\bar{h}_{c,men} = \int_{L_1}^{B/2} \frac{k_\ell ds}{(B/2 - L_1)\delta} \quad (2.22)$$

For $\theta > 20^\circ$ there is a simple analytical approximation for $\bar{h}_{c,men}$:

$$\bar{h}_{c,men} = \frac{k_\ell}{B/2 - L_1 \sin \theta} \frac{1}{\sin \theta} \ln \left[1 + \left(\frac{B}{2} - L_1 \right) \frac{\sin \theta}{\delta|_{s=L_1}} \right] \quad (2.23)$$

Equation 2.23 is obtained from Eqs. 2.21 and 2.22 by approximating the film thickness as

$$\delta = \delta|_{s=L_1} + s \frac{d\delta}{ds} \Big|_{s=L_1} \quad (2.24)$$

The mean heat transfer coefficient in the condenser section for a given z can be obtained by combining $\bar{h}_{c,f}$ and $\bar{h}_{c,men}$ with their respective areas, and including the thermal resistance of the wall:

$$\bar{h}_c = \left(\left[\frac{2L_1}{B} \bar{h}_{c,f} + \left(1 - \frac{2L_1}{B} \right) \bar{h}_{c,men} \right]^{-1} + \frac{t_w}{k_w} \right)^{-1} \quad (2.25)$$

The wall temperature in Eq. 2.19 is determined by the thermal resistance between the vapor temperature and the ambient temperature:

$$T_w = T_{ex,c} + (T_v - T_{ex,c}) \frac{1}{h_{ex,c}} \left(\frac{1}{h_{ex,c}} + \frac{1}{\bar{h}_c} \right)^{-1} \quad (2.26)$$

Therefore, Eqs. 2.19 – 2.26 are solved for \bar{h}_c and T_w using an iterative procedure.

Depending on the amount of working fluid within the MHP, part of the condenser may be blocked with liquid. In this case, the effective condenser length is $L_c - L_b$, where L_b is the length blocked by liquid.

$$L_b = \frac{M_b}{(A_v + NA_\ell)\rho_\ell} \equiv \frac{M_b}{A_t\rho_\ell} \quad (2.27)$$

The overall thermal resistance of the condenser can then be determined as follows:

$$r_c = \frac{1}{Q_a(L_c - L_b)} \int_{(L_e+L_a)}^{(L_t-L_b)} \frac{dQ}{dz} \frac{1}{BN} \frac{1}{\bar{h}_c} dz \quad (2.28)$$

In the numerical procedure, for the case of convective heat transfer outside the MHP, dQ/dz is defined using Eq. 2.7.

Now, the variation of the contact angle of the meniscus along the condenser is to be considered. At the inlet of the condenser, the contact angle is $\theta = \theta_0$. In the region near the liquid blocking zone, $\theta = 0$. Therefore, variation of the contact angle within the condenser takes place. At the beginning of the condenser, usually $L_1/R_m > \tan \theta$ and the liquid film is very thin. Along the condenser, while L_1/R_m is decreasing, there is a z location where $L_1/R_m \approx \tan \theta$. In the vicinity of this location, Eq. 2.15 cannot be solved; that is, the conservation of mass and energy in the film cannot be satisfied. This causes the contact angle θ to begin changing, starting from this particular z location in the condenser. In the present model, it is assumed that the θ variation after this location along the z -axis in the condenser is described by the relation:

$$\frac{L_1}{R_m} - \tan \theta = 0.01 \quad (2.29)$$

The value 0.01 is taken from both physical and numerical considerations. The choice of this value is made since it is very close to zero in comparison to that given by the right hand side of Eq. (2.29) at the beginning of the condenser, which can be greater than unity. This value, unlike zero, still provides a physically reasonable solution for Eqs. 2.15 and 2.16. This method allows for the approximate equality of the contact angles of the liquid flow in the corner and at the beginning of the liquid blocking zone.

2.5 Heat Transfer in the Evaporator Section

Following the approaches of Stephan and Busse (1992), Solov'yev and Kovalev (1984) and Holm and Goplen (1979) for the description of the heat transfer in the meniscus/thin-film transition region, an approximate thermal analysis of evaporative heat transfer in an MHP can be provided. The liquid flow in a thin evaporating liquid film toward the point $\dot{x} = 0$, as shown in Fig. 2.3, takes place under the influence of surface tension and the solid-liquid-vapor interfacial force field (disjoining pressure). The heat flux due to conduction through the liquid in the microlayer region of the meniscus is approximated as (Stephan and Busse, 1992):

$$q = \left[\frac{\delta}{k_\ell} + \frac{T_v(2\pi R_g T_v)^{0.5}(2 - \alpha)}{h_{fg}^2 \rho_v} \frac{1}{2\alpha} \right]^{-1} (T_w - T_{\delta,v}) \quad (2.30)$$

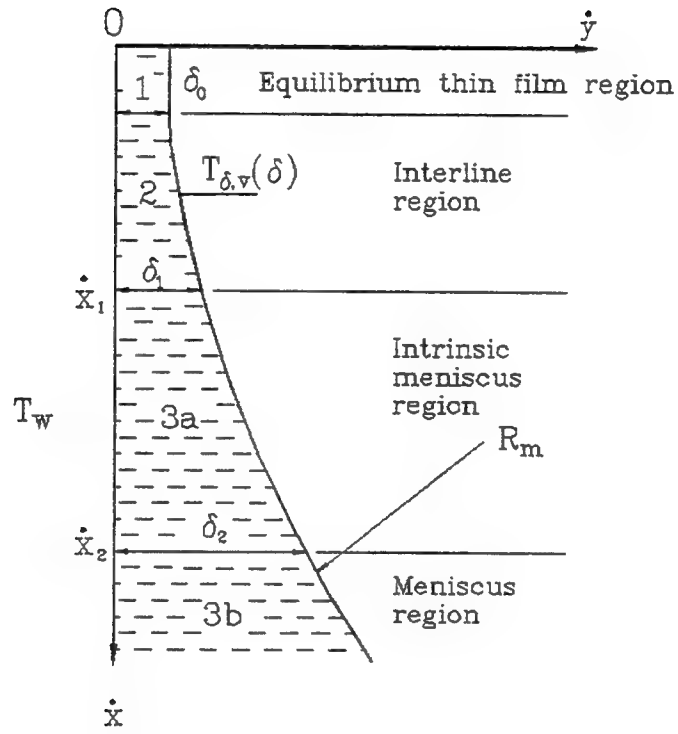


Figure 2.3: Cross section of the end of the extended meniscus region near a heated wall

where the interfacial thermal resistance is included. The disjoining pressure is (Derjaguin, 1955):

$$P_d = -\frac{A'}{\delta^3} \quad (2.31)$$

It is more convenient, however, to describe the disjoining pressure for extremely thin films by the following relation (Solov'yev and Kovalev, 1984; Holm and Goplen, 1979):

$$P_d = \rho_\ell R_g T_{\delta,v} \ln \left[a \left(\frac{\delta}{3.3} \right)^b \right] \quad (2.32)$$

where a and b are constants. Equation 2.32 was initially obtained by Potash and Wayner (1972). For pure water on quartz glass, $a = 1.534$ and $b = 0.0243$ (Holm and Goplen, 1979). In the adiabatic section, the thickness of the liquid film, which is extremely small, can be obtained from the relation $P_d = -\sigma/R_m$ by combining with Eq. 2.32.

It is essential to describe the difference between the temperature $T_{\delta,v}$ at the vapor side of the liquid-vapor interface and the saturation temperature T_v due to the disjoining pressure of the film. The following expression for the pressure drop at the surface of the film in the interline region is used by Solov'yev and Kovalev (1984), which is consistent to that by Carey (1992).

$$\ln \left[\frac{P_{\delta,v}}{P_{sat}(T_{\delta,v})} \right] = \frac{P_d}{\rho_\ell R_g T_{\delta,v}} \quad (2.33)$$

Solov'yev and Kovalev (1984) obtained closed-form solutions for q for three regions of an evaporating film, as shown in Fig. 2.3 (see also Carey, 1992), which are used in the present analysis. Region 1 represents the equilibrium (nonevaporating) thin film, and Region 2 (interline) is dominated by the disjoining pressure. In Region 3a (intrinsic meniscus), the curvature of the film varies under the influence of surface tension. In Region 3b (meniscus), the curvature is constant. The solutions by Solov'yev and Kovalev were obtained using the boundary-layer approximation for a liquid flow, and the relation between the thickness and the curvature of the film. The heat fluxes per unit groove length can then be estimated as:

$$\Delta Q_2 = 1.6\rho_v h_{fg}(T_w - T_v) \left[\frac{h_{fg}\rho_\ell R_g^2 b(\delta_1^4 - \delta_0^4)}{\nu_\ell k_\ell (T_w - T_v)} \right]^{0.5} \quad (2.34)$$

δ_0 is the equilibrium (nonevaporating) thin film thickness, which can be obtained from Eqs. 2.32 and 2.33 at $P_{\delta,v} = P_v$ and $T_{\delta,v} = T_w$, where the subscript v denotes the bulk conditions of the saturated vapor. For pure water on quartz glass, $\delta_0 = 1.8 \times 10^{-9}$ m. δ_1 is defined from the relation $a\delta_1^b = 1$; for water, $\delta_1 = 9.28 \times 10^{-9}$ m.

$$\begin{aligned} \Delta Q_{3a} &= \int_{\dot{x}_1}^{\dot{x}_2} \frac{(T_w - T_v)}{1/h_{pc} + \delta(\dot{x})/k_\ell} d\dot{x} \\ &= 1.5\rho_v h_{fg}(T_w - T_v) \left(\frac{R_g}{T_v} \right)^{0.5} \left(\frac{h_{fg}\sigma\delta_2^5}{\nu_\ell k_\ell (T_w - T_v)} \right)^{0.25} \end{aligned} \quad (2.35)$$

$$\begin{aligned}
\Delta Q_{3b} &= \int_{\dot{x}_2}^{W/\sin\gamma} \frac{(T_w - T_v)}{1/h_{pc} + \dot{x}^2/2R_m k_\ell} d\dot{x} \\
&= 1.4(T_w - T_v)(h_{pc} k_\ell R_m)^{0.5} \left[\frac{\pi}{2} - \arctan\left(\frac{h_{pc} \delta_2}{k_\ell}\right)^{0.5} \right] \quad (2.36)
\end{aligned}$$

where h_{pc} is the phase-change heat transfer coefficient at the liquid-vapor interface for the intensive evaporation process:

$$h_{pc} = 3.2\rho_v h_{fg} \sqrt{\frac{R_g}{T_v}} \quad (2.37)$$

where it has been assumed $\alpha = 1$.

In Eqs. 2.35 and 2.36, δ_2 is the radius of the effective influence of surface tension forces. For water, $\delta_2 \approx 10^{-7}$ m (Solov'yev and Kovalev, 1984). The heat transfer coefficient of the wetted zone for a given cross section is:

$$h_{e,men} = \frac{\Delta Q_2 + \Delta Q_{3a} + \Delta Q_{3b}}{T_w - T_v} \cdot \frac{\sin\gamma}{R_m \cos(\gamma + \theta)} \quad (2.38)$$

It should be mentioned that the third term in Eq. 2.38 is dominant. Then, for heat input from a hot fluid, taking the dry zone into account, it is possible to estimate the mean heat transfer coefficient in the evaporator as follows:

$$\bar{h}_e = \left(\left[\frac{2R_m \cos(\gamma + \theta)}{B \sin\gamma} h_{e,men} \right]^{-1} + \frac{t_w}{k_w} \right)^{-1} \quad (2.39)$$

The effective wall temperature in the evaporator in Eqs. 2.34 – 2.38 is obtained in a manner similar to that in the condenser (Eq. 2.26):

$$T_w = T_{ex,e} + (T_v - T_{ex,e}) \frac{1}{h_{ex,e}} \left(\frac{1}{h_{ex,e}} + \frac{1}{\bar{h}_e} \right)^{-1} \quad (2.40)$$

When a heat input in the evaporator is given by $Q(z)$, the dry zone of the wall can be overheated (see Figs. 2.1 and 2.2(a)). To estimate the overheating, the thermal conductance equation is considered:

$$k_w t_w \frac{d^2 T}{ds^2} = \frac{1}{2N(B/2 + t_w)} \frac{dQ}{dz} \quad (2.41)$$

where T is the mean cross sectional wall temperature at each point on s . In deriving Eq. 2.41, it is assumed that the heat flux on the wall at each point on z is constant. The boundary conditions are:

$$T|_{s=L_1} = T_w; \quad \left. \frac{dT}{ds} \right|_{s=0} = 0 \quad (2.42)$$

Solving Eq. 2.41, the overheat can be expressed as

$$\Delta T_{e,w} = T|_{s=0} - T|_{s=L_1} = \frac{L_1^2}{2N(B/2 + t_w)k_w t_w} \frac{dQ}{dz} \quad (2.43)$$

Therefore, the maximum thermal resistance of the evaporator is:

$$r_e = \frac{T_{w,max} - T_v}{Q_a} = \frac{1}{Q_a L_e N} \int_0^{L_e} \frac{dQ}{dz} \left[\frac{L_1^2}{2(B/2 + t_w)k_w t_w} + \frac{1}{B\bar{h}_e} \right] dz \quad (2.44)$$

2.6 Liquid Flow in a Capillary Groove

The problem of liquid flow in triangular grooves (Eqs. 2.5 and 2.13) was solved in dimensionless form by Ayyaswamy et al. (1974) and Khrustalev (1981). Ayyaswamy et al. (1974) neglected the effects of shear stresses at the liquid-vapor interface. Since the effects of shear stresses at a free liquid surface may be important for MHPs, the results of Khrustalev (1981) are used, where this two-dimensional boundary-value problem was solved by the Ritz method in terms of R-functions. The solution gives the values of the dimensionless volume flux through a triangular groove, which is defined similar to that given by Kamotani (1976b):

$$V(\gamma, \theta, F) = \int \int_{A_\ell} \frac{w_\ell(x, y) \mu_\ell}{HW^3 \left(\frac{dP_\ell}{dz} + \frac{\rho_\ell}{2A_\ell} \frac{d}{dz} (\bar{w}_\ell^2 A_\ell) + \rho_\ell g \sin \varphi \right)} dx dy \quad (2.45)$$

where

$$F = - \frac{f_v \rho_v \bar{w}_v^2}{2W \left(\frac{dP_\ell}{dz} + \frac{\rho_\ell}{2A_\ell} \frac{d}{dz} (\bar{w}_\ell^2 A_\ell) + \rho_\ell g \sin \varphi \right)} \quad (2.46)$$

The variable $1/V$ represents the hydraulic resistance of the groove. Then, using Eqs. 2.2 and 2.45, the pressure gradient can be defined as:

$$\frac{dP_\ell}{dz} + \frac{\rho_\ell}{2A_\ell} \frac{d}{dz} (\bar{w}_\ell^2 A_\ell) + \rho_\ell g \sin \varphi = \frac{\mu_\ell \bar{w}_\ell A_\ell}{W^3 H V} \quad (2.47)$$

where

$$W = R_m \cos(\gamma + \theta), \quad H = W / \tan \gamma \quad (2.48)$$

and

$$A_\ell = R_m^2 \left[\cos(\gamma + \theta) \left(\sin(\gamma + \theta) + \frac{\cos(\gamma + \theta)}{\tan \gamma} \right) - \left(\frac{\pi}{2} - \gamma - \theta \right) \right] \quad (2.49)$$

For $\gamma = 30^\circ$ and relatively small values of F , the results given by Khrustalev (1981) can be approximated as follows:

$$V(\theta, F) = (a_0 + a_1 \theta + a_2 \theta^2) e^F \quad (2.50)$$

where $a_0 = 0.0241$, $a_1 = 0.000905$, $a_2 = 8.75 \times 10^{-6}$, and θ is in arc degrees. This approximation is in agreement with the results of Ayyaswamy et al. (1974) for $F = 0$.

2.7 Numerical Treatment

The four main variables dependent on z to be found are as follows:

$Y = R_m^{-1}$: curvature of the free surface of the meniscus,

$\dot{m} = \bar{w}_\ell \rho_\ell A_\ell$: mass flow rate of liquid in one corner,

p_ℓ : liquid pressure,

p_v : vapor pressure.

The following system of four ordinary differential equations were solved numerically using the fourth-order Runge-Kutta procedure:

$$\frac{dY}{dz} = \frac{1}{\sigma} \left(\frac{dp_v}{dz} - \frac{dp_\ell}{dz} \right) \quad (2.51)$$

$$\frac{dG}{dz} = \frac{B}{h_{fg}} h_{ex,i} (T_{ex,i} - T_v) \left(1 + \frac{h_{ex,i}}{\bar{h}_i} \right)^{-1}, \quad i = e, c, a \quad (2.52)$$

or for a given heat-load function $Q(z)$

$$\frac{d\dot{m}}{dz} = \frac{1}{h_{fg} N} \frac{dQ(z)}{dz} \quad (2.53)$$

$$\frac{dP_\ell}{dz} = \frac{\mu_\ell \dot{m}}{W^3 H V \rho_\ell} - \rho_\ell g \sin \varphi - \frac{1}{2 A_\ell \rho_\ell} \frac{d}{dz} \left(\frac{\dot{m}^2}{A_\ell} \right) \quad (2.54)$$

$$\frac{dP_v}{dz} = -\frac{d}{dz} \left(\beta_v \frac{N^2 \dot{m}^2}{A_v^2 \rho_v} \right) - f_v \frac{2}{D_{h,v}} \frac{N^2 \dot{m}^2}{A_v^2 \rho_v} - \rho_v g \sin \varphi \quad (2.55)$$

The boundary conditions at $z = 0$ are:

$$Y = R_{m0}^{-1}, \quad \dot{m} = 0, \quad p_v = p_{v0}, \quad p_\ell = p_{v0} - \frac{\sigma}{R_{m0}} \quad (2.56)$$

The following expressions were also used: Eqs. 2.3, 2.10, 2.18 – 2.27, 2.34 – 2.40, 2.44, 2.46, 2.48, 2.49 and 2.50.

For the case of a known heat load, it is convenient to use the approximation for the vapor pressure distribution given by Faghri (1989), instead of numerically solving Eq. 2.55:

$$p = p_{v,0} + \rho_v \left[-8 \left| \frac{\text{Re}_r}{2} \right| - \frac{16}{3} \left| \frac{\text{Re}_r}{2} \right|^2 \right] \left(\frac{4z\nu_v}{D_{h,v}^2} \right)^2, \quad 0 \leq z \leq L_e \quad (2.57)$$

$$p = p_{0,a} + \rho_v \bar{w}_{v,a} \left(-\frac{32(z - L_e)\nu_v}{D_{h,v}^2} \right), \quad L_e \leq z \leq L_e + L_a \quad (2.58)$$

$$p = p_{0,c} + 8\rho_v \bar{w}_{v,a}^2 \left(1 - \frac{2}{3} \left| \frac{\text{Re}_r}{2} \right| \right) \left(\left| \frac{\text{Re}_r}{2} \right| \right) \left[\frac{4(z - L_e - L_a)\nu_v}{\bar{w}_{v,a} D_{h,v}^2} \right]^2$$

$$- 8\rho_v \bar{w}_{v,a}^2 \left(1 - \frac{2}{3} \left| \frac{\text{Re}_r}{2} \right| \right) \left[\frac{4(z - L_e - L_a)\nu_v}{\bar{w}_{v,a} D_{h,v}^2} \right], \quad L_e + L_a \leq z \leq L_t - L_b \quad (2.59)$$

where $p_{0,a}$ and $p_{0,c}$ are the values of the pressure at the inlets of the adiabatic and condenser zones, respectively. The agreement of the results of the numerical solution of Eq. 2.55 and Eqs. 2.57 – 2.59 is within several percent of the total vapor pressure drop for the given MHP parameters.

An iterative procedure was used to obtain the maximum heat transfer capacity, Q_{\max} , and the overall thermal resistance, r_t , of an MHP. The overall thermal resistance is:

$$r_t = r_e + r_c + r_v \quad (2.60)$$

where r_v is the thermal resistance of the vapor flow, which is defined as

$$r_v = \frac{1}{Q_a} \left[\frac{1}{L_e} \int_0^{L_e} T_v dz - \frac{1}{L_c - L_b} \int_{L_e+L_a}^{L_t-L_b} T_v dz \right] \quad (2.61)$$

The mass of circulating fluid, $M_\ell = M_t - M_b$, which represents the right-hand side of Eq. 2.3 minus M_b , and the meniscus radius $R_m = Y^{-1}$ are obtained as functions of several parameters:

$$M_\ell = M_\ell(R_{m0}, Q_a, \theta, T_v, \varphi, \dots) \quad (2.62)$$

$$R_m = R_m(z, R_{m0}, Q_a, \theta, T_v, \varphi, \dots) \quad (2.63)$$

Analyzing these functions and taking into account Eq. 2.3, some conclusions concerning r_t , L_b , and Q_{\max} can be made. For the distribution of the liquid in an MHP, it is logical to assume that, at the maximum heat load ($Q_a = Q_{\max}$), R_{m0} has the smallest value possible, provided that Eqs. 2.51 – 2.55 can still be solved successfully and Eq. 2.3 is satisfied. It should be noted that the variation of the maximum heat

transport due to decreasing R_{m0} is very small when $R_{m0} < 0.1D_{h,v}$. The exact value of $R_{m,\min}$, which is different for each MHP design, can be obtained by comparison of the predicted and experimental results for Q_{\max} for MHP operation against gravity. To obtain the value for L_b and r , an iterative procedure is used, varying the effective condenser length and R_{m0} .

The numerical results for the maximum heat transfer capacity Q_{\max} are obtained with the following procedure:

1. For a definite small R_{m0} and Q'_a , the system of Eqs. 2.51 – 2.55 is solved, and the obtained values of M_ℓ and $R_m(L_t)$ are analyzed. If $M_\ell \ll M_t$ and $R_m(L_t) < R_{m,\max}$, liquid may be blocking part of the condenser. Therefore, the length of the liquid blocking zone L_b is estimated and the new effective condenser length $L'_c = L_c - L_b$ is set.
2. The value of the total heat load is increased, $Q''_a = Q'_a + \Delta Q_a$, and step 1 is repeated until $R_m(L_t) \simeq R_{m,\max}$, and the variation of the meniscus contact angle θ occurs near the beginning of the blocking zone. This total heat load is Q_{\max} .
3. The validity of Q_{\max} is checked by decreasing R'_{m0} . If no change occurs, go to step 4. Otherwise, repeat steps 1 and 2.
4. If there is a lack of liquid in the MHP and $M_\ell = M_t$ is obtained in the

first two steps for $R_m(L_t) < R_{m,\max}$, the corresponding maximum value of Q_a is considered to be Q_{\max} , provided that decreasing R_{m0} has no effect on the results.

2.8 Results and Discussion

To verify the numerical results obtained, the experimental data provided by Wu and Peterson (1991) were used. Therefore, the presented results refer to an MHP with the following characteristics: $L_e = 0.013$ m, $L_a = 0.031$ m, $L_c = 0.013$ m, $B = 0.0007$ m, $\gamma = 30^\circ$, $\varphi = 0$, $M_t = 0.0032$ g, $N = 4$, $t_w = 0.00019$ m, $\alpha = 1$. The working fluid was water, and two containers, made of copper and silver, were examined. The axial heat distribution, $Q(z)$, was specified as:

$$Q = \begin{cases} Q_a z / L_e, & 0 \leq z \leq L_e \\ Q_a, & L_e < z < L_e + L_a \\ Q_a \left(1 + \frac{L_e + L_a - z}{L_c - L_b} \right), & L_e + L_a \leq z \leq L_t - L_b \end{cases} \quad (2.64)$$

and Eq. 2.53, instead of Eq. 2.52, was used in the numerical procedure.

Most of the results of the present analysis are for heat loads close to the performance limitations. The data in Figs. 2.4, 2.5 and 2.7–2.9 were obtained for a vapor temperature at the evaporator end cap of $T_{v0} = 60^\circ\text{C}$. The hydrodynamic performance characteristics of the MHP with no excess liquid is shown in Fig. 2.4.

Dashed lines correspond to the case of neglecting shear stresses in the liquid at the

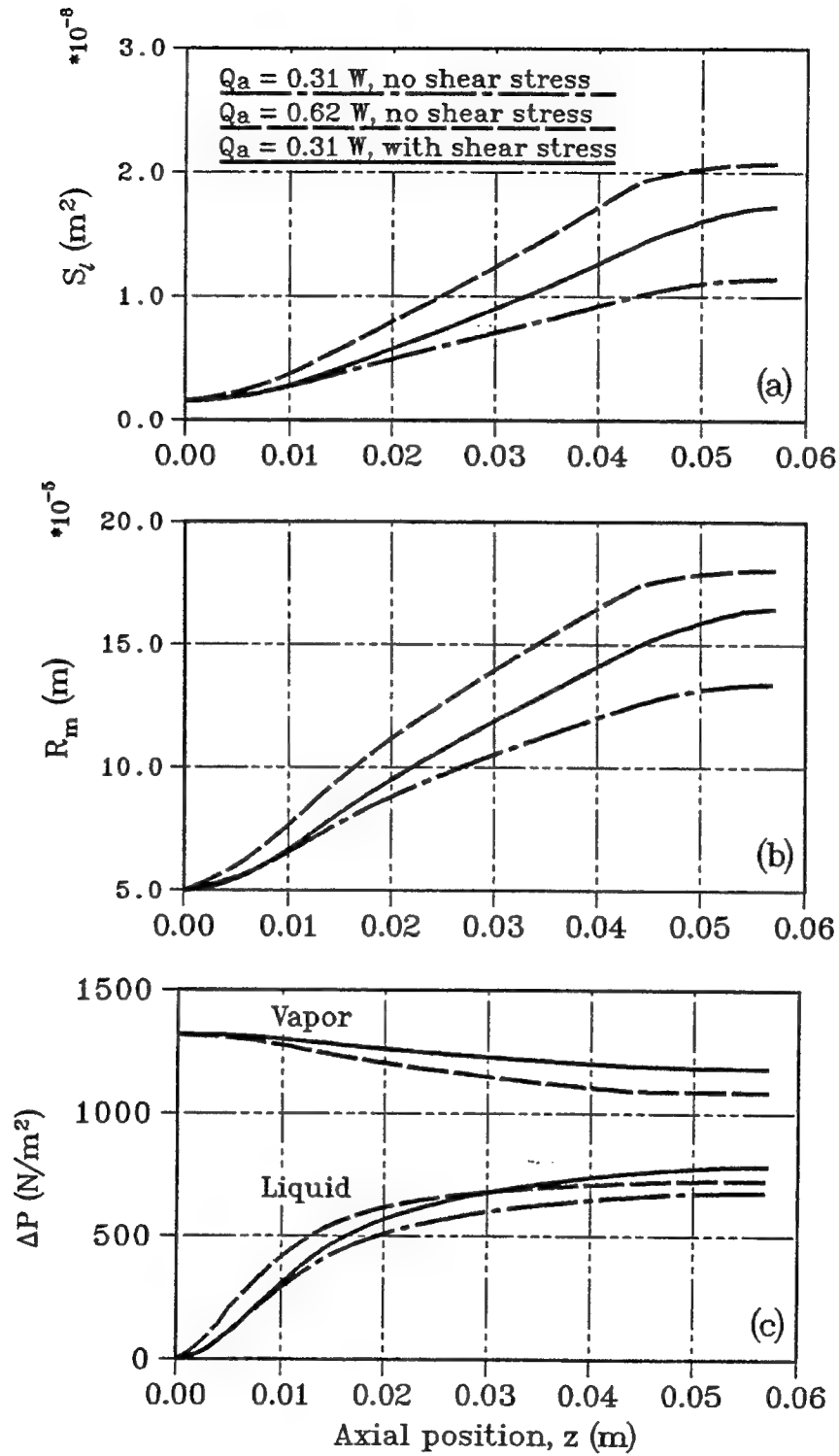


Figure 2.4: Comparison of the performance of the micro heat pipe with and without shear stress at the vapor-liquid interface for the case of no excess liquid in the MHP ($\theta_0 = 10^\circ$) (a) liquid cross sectional area, (b) radius of curvature of the meniscus, (c) pressure variation.

liquid-vapor interface, and solid lines refer to the case of including the effects of shear stresses (in both cases the vapor distribution is the same). One of the distinguishing features of an MHP is the variable liquid cross sectional area along the axis. As seen in Fig. 2.4(a) for $\theta_0 = 10^\circ$, A_ℓ increased by more than ten times along the length of the MHP, while the radius of the meniscus, R_m , changed by only four times, as shown in Fig. 2.4(b). For an inclination angle of $\varphi = 0$, the meniscus curvature increased monotonically along the z direction. The pressure drop in the liquid was several times higher than that of the vapor, which is illustrated in Fig. 2.4(c). The liquid pressure increased drastically in the evaporator, where the cross sectional area of the liquid was small. Thus, extending the cross sectional area of the liquid, due to the decrease of that of the vapor, may increase the maximum heat transfer capacity of the MHP. The results in Fig. 2.4 are given to show some basic information concerning the hydrodynamic characteristics of the MHP when the radius of curvature R_{m0} is held constant at $50 \mu\text{m}$. It should be noted that, in this example, the mass of liquid within the heat pipe is not fixed, but the value of R_{m0} was the same for all curves, which gave the opportunity to show the influence of the vapor-liquid interaction on the hydraulic MHP characteristics more clearly.

The influence of the liquid charge on Q_{\max} in the case when there is a lack of liquid in the MHP is illustrated in Fig. 2.5 ($\theta_0 = 10^\circ$). For the considered MHP, this situation only occurs in the absence of shear stress at the free liquid surface

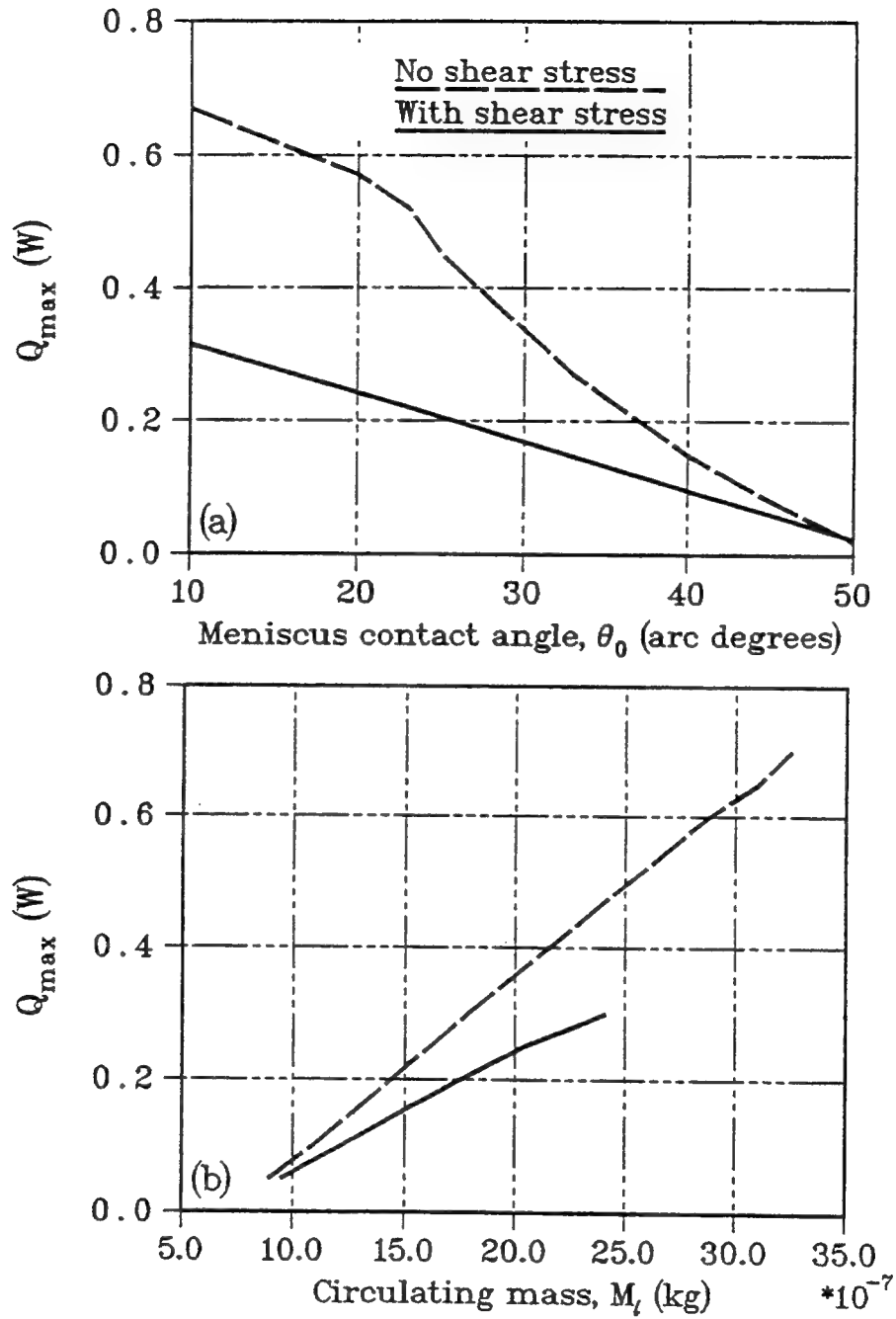


Figure 2.5: Dependence of the maximum heat transfer on (a) meniscus contact angle at the evaporator end cap, (b) mass of circulating liquid in the case of insufficient liquid fill ($\theta_0 = 10^\circ$, $R_{m0} = 50\mu\text{m}$)

and for small θ_0 . The minimum contact angle, θ_0 , has a significant influence on the performance of the MHP, especially on the maximum heat transfer capacity, as shown in Fig. 2.5 for small liquid charges. According to Stepanov et al. (1977), $\theta_0 = 33^\circ$ for copper-water and 38° for silver-water pairs, and Wu and Peterson (1991) gave these values to be 55° and 45° , respectively.

The comparison of the numerical results and the experimental data reported by Wu and Peterson (1991) for the maximum heat transfer capacity are shown in Fig. 2.6 for MHPs with copper and silver casings. While the data for the minimum contact angles are contradictory and can be influenced by many physical factors, the numerical results are presented for $\theta_0 = 33^\circ$, 38° and 45° . The agreement between the experimental results of the onset of dryout and the present numerical prediction is good. Neglecting the shear stress at the free surface of the liquid due to vapor/liquid frictional interaction ("no shear stress" in Figs. 2.6 and 2.8) can lead to an overestimation of the maximum heat transfer capacity. The shear stress at the free liquid surface influences the liquid distribution along the heat pipe, which can result in an increase of the liquid blocking of the condenser end in comparison with the case of neglecting this shear stress. The liquid distribution in an MHP is affected by the heat load, as shown in Fig. 2.7(a) ($\theta_0 = 33^\circ$). The liquid distribution and the heat load determine the temperature variation along a heat pipe (Fig. 2.7(b)).

As seen in Fig. 2.8 ($\theta_0 = 33^\circ$), the overall thermal resistance of the MHP

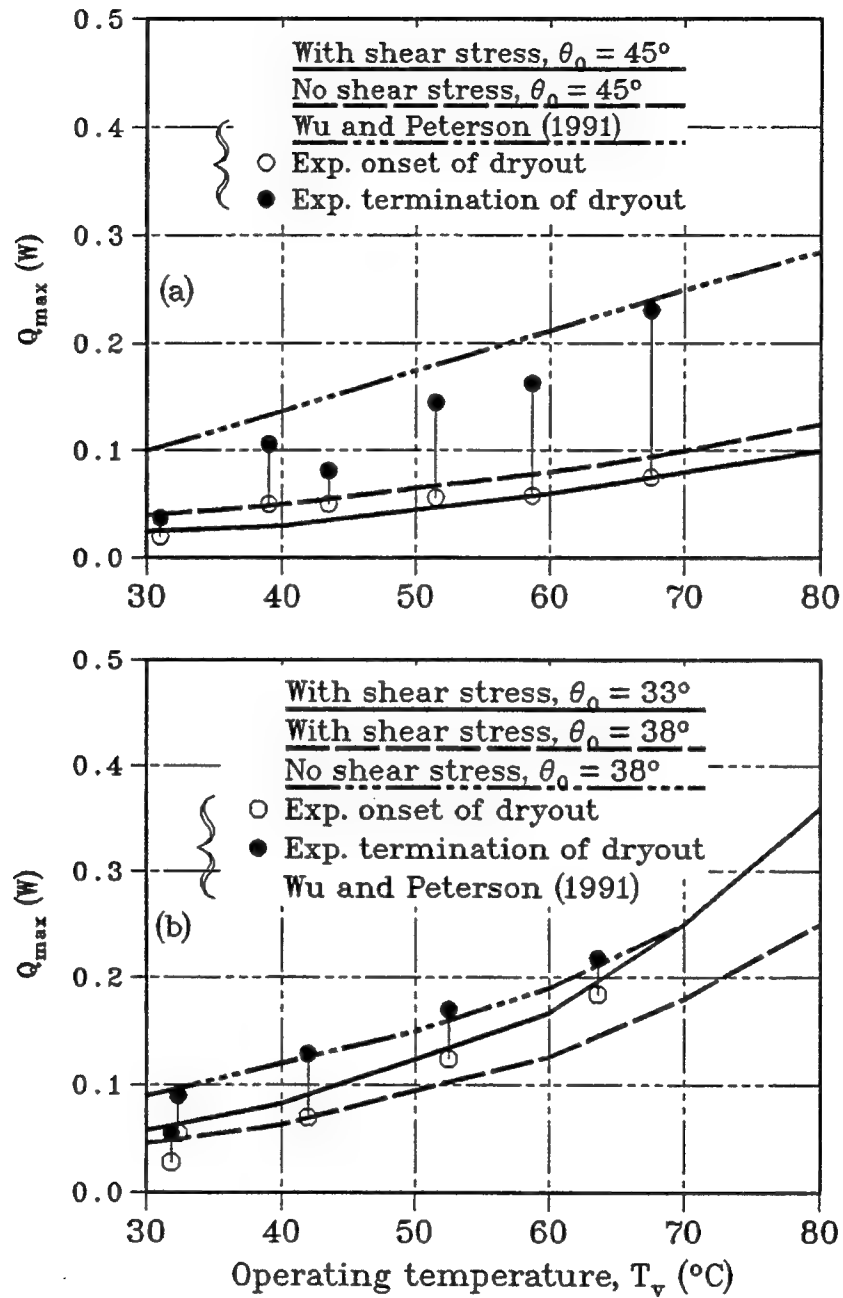


Figure 2.6: Maximum heat transfer versus operating temperature (a) copper-water MHP, (b) silver-water MHP

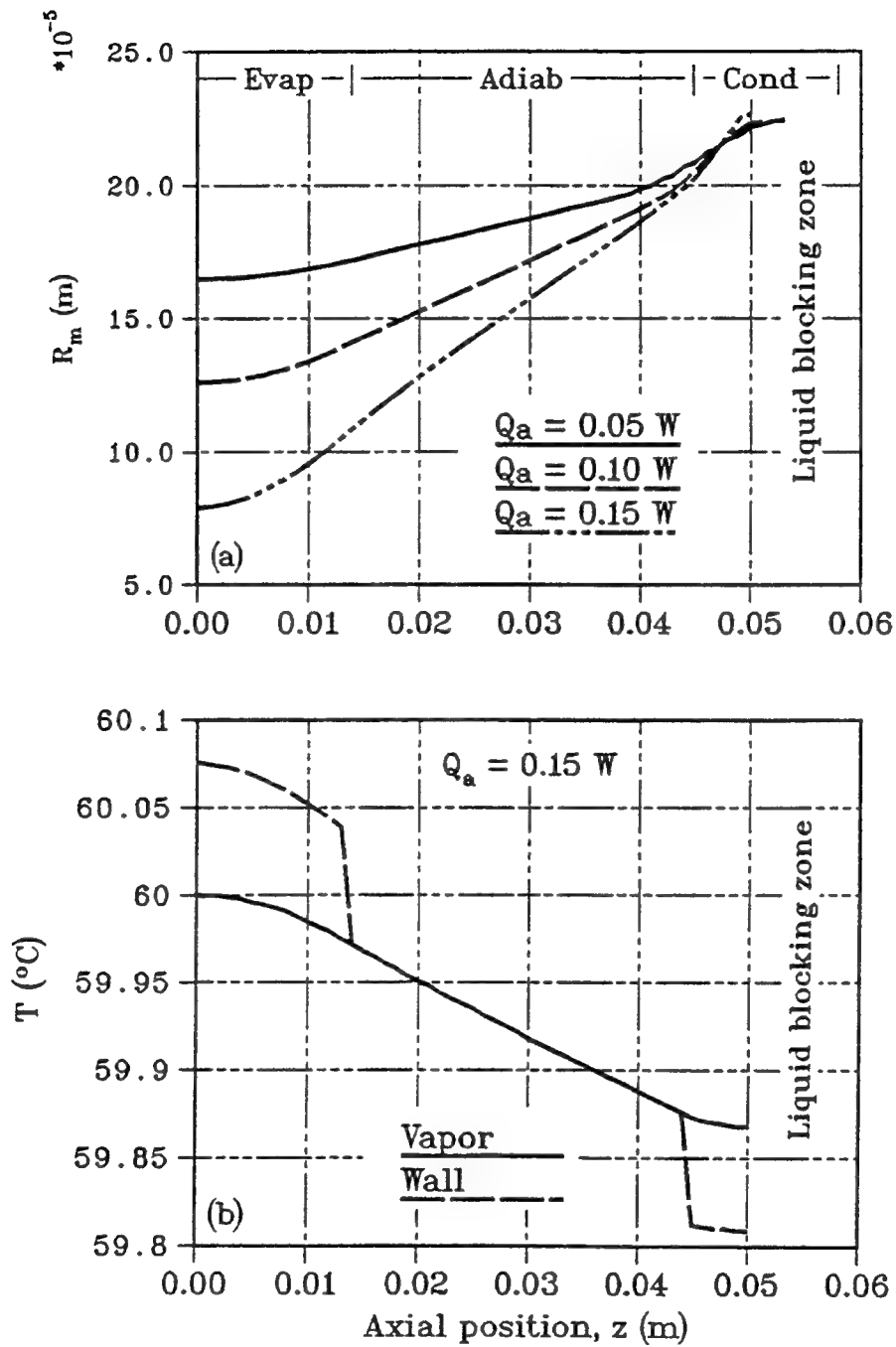


Figure 2.7: Performance characteristics of the copper-water MHP (a) radius of the liquid surface curvature, (b) temperature distribution

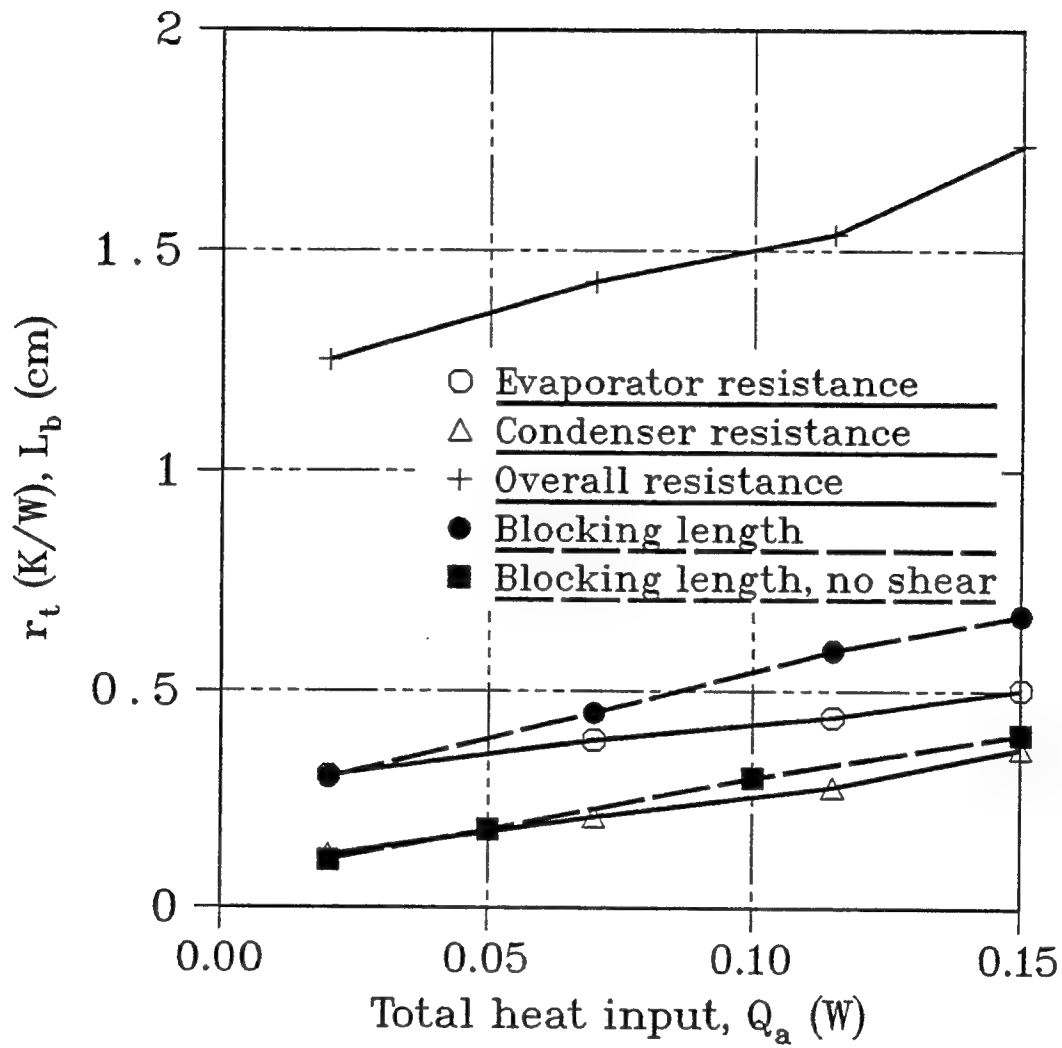


Figure 2.8: Influence of total heat input on the thermal resistance and liquid blocking length (copper-water MHP)

is summarized by three terms: r_e , r_c , r_v , which must be taken into consideration, although the resistance of the vapor flow is the greatest for the conditions studied. It should be noted that, according to experimental data by Wu and Peterson (1991), the thermal resistance of the MHP which was not charged with working fluid (empty tube) was approximately 150 K/W.

The variation of the meniscus contact angle in the condenser is shown in Fig. 2.9. In this region, where progressive variation of the contact angle occurred, the liquid cross sectional height H increased sharply. Therefore, the second radius of curvature of the liquid surface, R_2 , becomes significant in this region. In the present paper, its influence on the distribution of liquid along the MHP was neglected for all zones. However, to complete the physical model, it can be assumed that the free surface of the liquid blocking zone has a curvature with a main radius of R_b , which should be estimated as:

$$\frac{2}{R_b} = \left(\frac{1}{R_2} + \frac{1}{R_m} \right)_{z=L_t-L_b} \quad (2.65)$$

From the results of the MHP mathematical model, a new flat MHP configuration with an increased liquid cross sectional area for electronic cooling applications is proposed, as shown in Fig. 2.10. Due to surface tension forces, liquid is contained in the narrow passages separating the vapor spaces, and is also distributed along the flat heat-loaded walls. The advantages of this configuration are

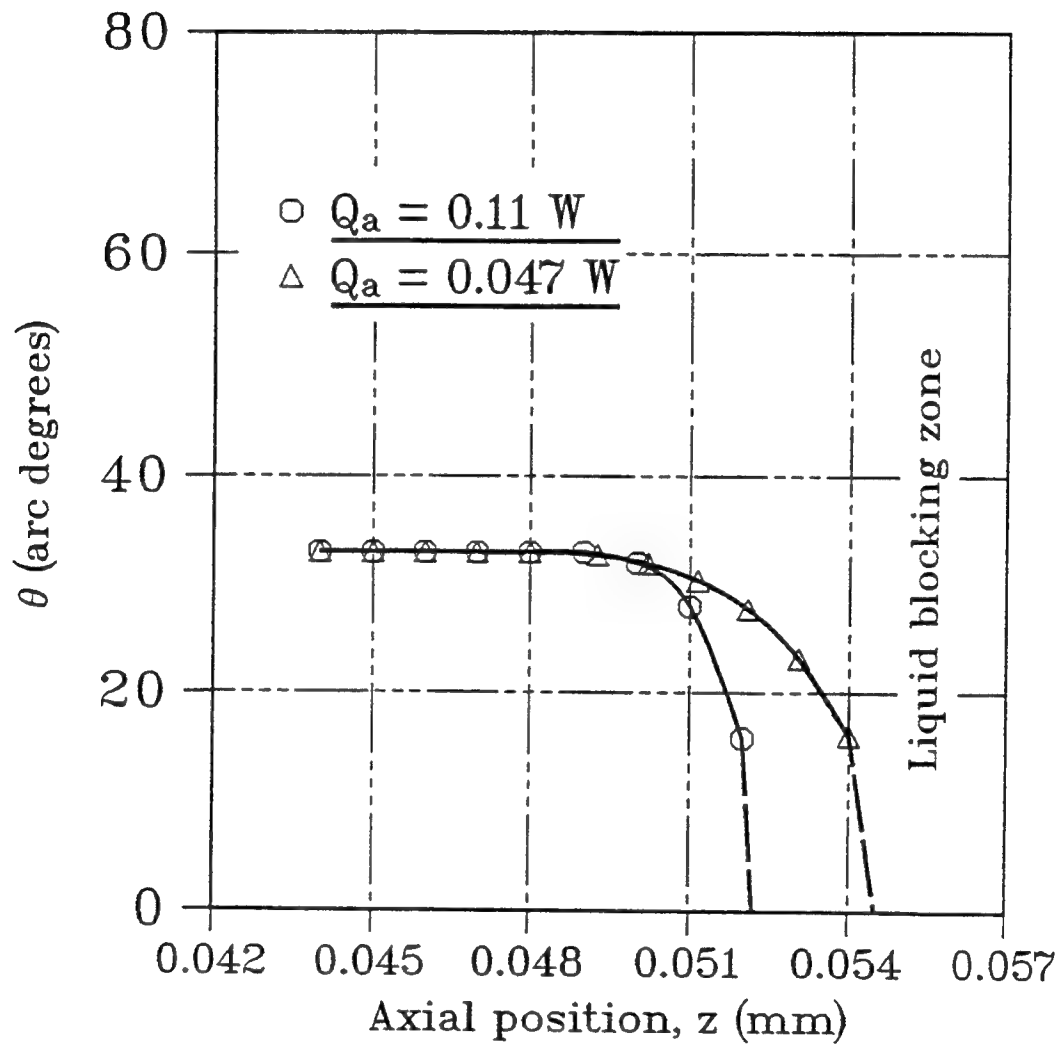


Figure 2.9: Variation of the contact angle in the condenser

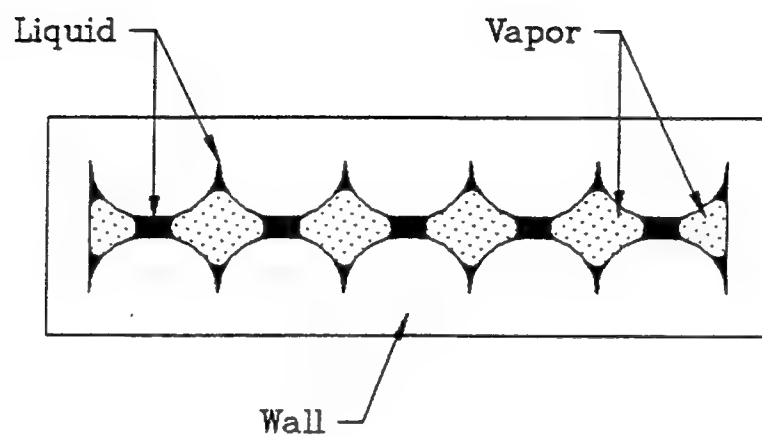


Figure 2.10: New configuration cross section of a flat MHP

an increase in the maximum heat transfer capacity and a lower manufacturing price in compared to several MHPs investigated by Wu and Peterson (1991).

2.9 Conclusions

The numerical results of the mathematical model describing the fluid flow and heat transfer within a micro heat pipe are summarized as follows:

1. Shear stresses in the liquid at the liquid-vapor interface due to frictional interaction significantly influenced the maximum heat transfer capacity.
2. Accounting for shear stresses at the liquid free surface increased the length of the liquid blocking zone in the condenser.
3. The dynamic component of the pressure gradient in the liquid had no pronounced effect on the performance characteristics of the MHP.
4. For nearly maximum heat loads, the largest portion of the liquid pressure drop occurred in the evaporator and the beginning of the adiabatic section, where the liquid cross sectional area was several times smaller than that in the condenser.
5. The dominant thermal resistances within the MHP were those of the vapor flow and the liquid film in the evaporator and condenser.
6. The amount of working fluid and the minimum wetting contact angle strongly influenced the performance characteristics of the MHP.

7. The variation of the meniscus contact angle in the condenser occurred near the liquid blocking zone.

Chapter 3

EVAPORATION AND CONDENSATION ON GROOVED STRUCTURES

3.1 Summary

A detailed mathematical model is developed which describes heat transfer through thin liquid films in the evaporator and condenser of heat pipes with capillary grooves. The model accounts for the effects of interfacial thermal resistance, disjoining pressure and surface roughness for a given meniscus contact angle. The free surface temperature of the liquid film is determined using the extended Kelvin equation and the

expression for interfacial resistance given by the kinetic theory. The numerical results obtained are compared to existing experimental data. The importance of the surface roughness and interfacial thermal resistance in predicting the heat transfer coefficient in the grooved evaporator is demonstrated.

3.2 Introduction

In an axially-grooved heat pipe (AGHP), condensate return is accomplished by the flow of liquid in the grooves under the influence of surface tension, and the maximum heat flux in the evaporator is restricted by the fluid transport limit or by the boiling limitation. The value of the evaporative heat transfer coefficient is related to the maximum heat flux by the superheat of the evaporating liquid film, which is critical for the onset of nucleate boiling. Therefore, a detailed mathematical model is developed which includes both the heat transfer through the thin liquid films and heat conduction in the fin between grooves and in the meniscus region film. With this model, the local heat transfer coefficients in the evaporator and condenser sections of low-temperature AGHPs are determined. The present analysis, which incorporates several one-dimensional boundary-value problems, has the following comparatively new features:

- The heat transfer through the liquid films in both the evaporator and condenser is described with respect to the disjoining pressure, interfacial thermal resistance and surface roughness or curvature (Figs. 3.1 and 3.2).
- The free surface temperature of the liquid film is determined using the extended Kelvin equation and the expression for interfacial resistance given by the kinetic theory.
- Heat conduction in the fin between grooves and the liquid meniscus is considered for both the evaporator and condenser sections using a one-dimensional approximation.

Because of these features the proposed model is a significant contribution over the previous investigators' attempts (Kamotani, 1976b, 1978; Vasiliev et al., 1981; and Stephan and Busse, 1992). Also, the model of ultra-thin film evaporation is employed which is consistent with that given by Carey (1992) and Wayner et al. (1976). The present model is developed for rectangular, triangular and trapezoidal grooves in a circular tube, but flat evaporators and condensers are also described by the presented equations. Heat transfer processes in the heat pipe container and working fluid were considered to be one-dimensional in the radial direction, such that axial heat conduction was neglected. The emphasis has been placed on the formation of the thin liquid films affected by the operational conditions. During the

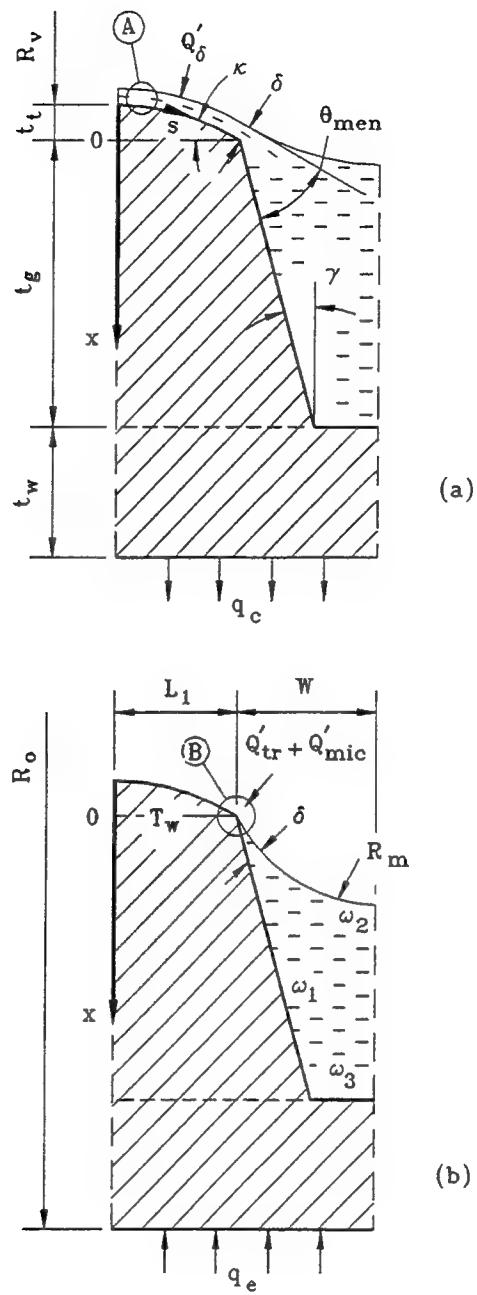


Figure 3.1: Cross sections of the characteristic elements of an axially-grooved heat pipe (a) condenser, (b) evaporator

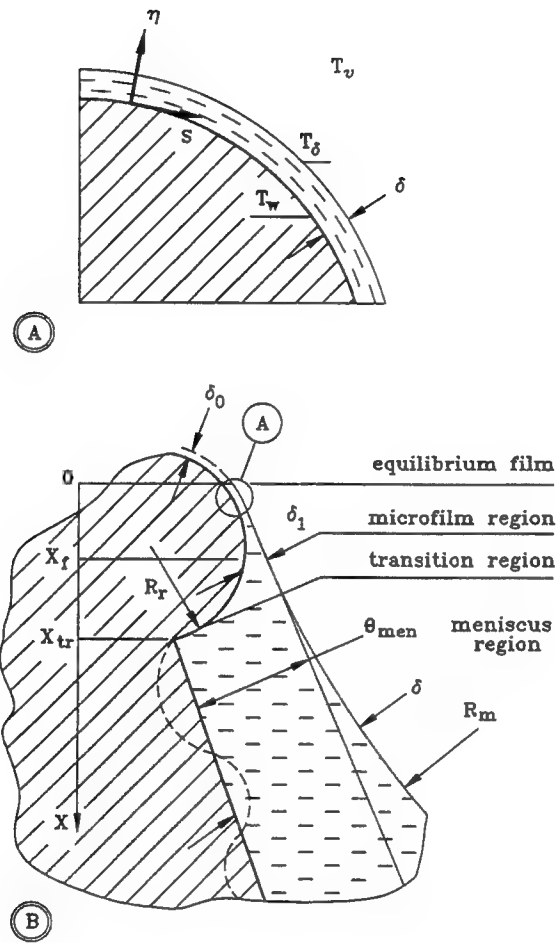


Figure 3.2: Thin evaporating film on a fragment of the rough solid surface

condensation process, liquid in the subcooled thin film flows towards the meniscus region along the s -coordinate, as shown in Fig. 3.1(a). During evaporation, liquid in the superheated thin film flows from the meniscus region in the opposite direction, as presented in Figs. 3.1(b) and 3.2. The numerical results were obtained using an iterative mathematical procedure which involved the following boundary-value problems:

1. Formation of and heat transfer in thin films.
2. Heat transfer in the evaporating film on a rough surface.
3. Heat transfer in the condensate film on the fin top surface.
4. Heat conduction in a metallic fin and liquid meniscus.

These problems are described in detail in the following sections.

3.3 Formation of and Heat Transfer in Thin Liquid Films

The thermal resistance of a low-temperature AGHP depends mostly on the thickness of the thin films in the condenser and evaporator sections. Since the heat transfer and fluid dynamics processes in a thin film are similar in both sections, it is possible to describe the formation of the films by the same equations, but taking into account the

different directions of the temperature potential. In this section a thin evaporating film on a heat-loaded surface with curvature K_w is considered, as shown in Fig. 3.2(b). The local heat flux through the film due to heat conduction is

$$q = k_\ell \frac{T_w - T_\delta}{\delta} \quad (3.1)$$

where the local thickness of the liquid layer δ and the temperature of the free liquid film surface T_δ are functions of the s -coordinate. For small Reynolds numbers, an assumption of a fully developed laminar liquid flow velocity profile is valid:

$$u_\ell = -\frac{1}{2\mu_\ell} \frac{dp_\ell}{ds} (2\eta\delta - \eta^2) \quad (3.2)$$

where η is the coordinate normal to the solid-liquid interface. The vapor pressure is assumed to be constant along the s -coordinate, and the liquid flow is driven mainly by the surface tension and the adhesion forces.

$$\frac{dp_\ell}{ds} = -\sigma \frac{dK}{ds} + \frac{dp_d}{ds} - K \frac{d\sigma}{dT_\delta} \frac{dT_\delta}{ds} + \frac{d}{ds} (\rho_v^2 v_{v,\delta}^2) \left(\frac{1}{\rho_v} - \frac{1}{\rho_\ell} \right) \quad (3.3)$$

K is the local interface curvature, p_d is the disjoining pressure (Derjaguin, 1955) and the last term is the kinetic reaction of the evaporating fluid pressure. The impact of the last two terms on the results was found to be negligible in the present analysis, therefore they are omitted in the following equations.

The continuity equation for the evaporating liquid layer is

$$\frac{d}{ds} \int_0^\delta u_\ell d\eta = \frac{q}{h_{fg}\rho_\ell} \quad (3.4)$$

Substituting equations (3.1)–(3.3) into equation (3.4) gives the following relation for the thickness of the evaporating film, $\delta(s)$:

$$\frac{1}{3\mu_\ell} \frac{d}{ds} \left[\delta^3 \frac{d}{ds} (p_d - \sigma K) \right] = \frac{k_\ell (T_w - T_\delta)}{h_{fg}\rho_\ell \delta} \quad (3.5)$$

The film surface curvature K is expressed in terms of the solid surface curvature K_w and film thickness as

$$K = K_w + \frac{d^2\delta}{ds^2} \left[1 + \left(\frac{d\delta}{ds} \right)^2 \right]^{-3/2} \quad (3.6)$$

Following Potash and Wayner (1972), a power-law dependence of p_d on δ is given for nonpolar liquids.

$$p_d = -A'\delta^{-B} \quad (3.7)$$

For water, however, the logarithmic dependence is preferable (Holm and Goplen, 1979).

It is assumed that the absolute value of the vapor core pressure at any z -location along the groove is related to vapor temperature by the saturation conditions

$$p_v = p_{\text{sat}}(T_v) \quad (3.8)$$

and therefore can be defined for a given T_v using the saturation tables.

The temperature of the interface T_δ is affected by the disjoining and capillary pressures, and also depends on the value of the interfacial resistance, which is defined for the case of a comparatively small heat flux by the following relation.

$$q = - \left(\frac{2\alpha}{2 - \alpha} \right) \frac{h_{fg}}{\sqrt{2\pi R_g}} \left[\frac{p_v}{\sqrt{T_v}} - \frac{(p_{\text{sat}})_\delta}{\sqrt{T_\delta}} \right] \quad (3.9)$$

p_v and $(p_{\text{sat}})_\delta$ are the saturation pressures corresponding to T_v in the bulk vapor and at the thin liquid film interface, respectively.

While equation (3.9) is used in the present analysis, it seems useful to mention that for the case of extremely high heat fluxes during intensive evaporation in thin films, Solov'ev and Kovalev (1984) have approximated the interfacial heat flux by the following expression:

$$q = 3.2\sqrt{R_g T_v} [(p_{\text{sat}})_\delta - p_v] \quad (3.10)$$

Equation (3.10) was derived with the assumption that the accommodation coefficient $\alpha = 1$ from the expressions given by Labuntsov and Krukov (1977).

The relation between the vapor pressure over the thin evaporating film, $(p_{\text{sat}})_\delta$, affected by the disjoining pressure, and the saturation pressure corresponding

to T_δ , $p_{\text{sat}}(T_\delta)$, is given by the extended Kelvin equation (Carey, 1992, p. 323):

$$(p_{\text{sat}})_\delta = p_{\text{sat}}(T_\delta) \exp \left[\frac{(p_{\text{sat}})_\delta - p_{\text{sat}}(T_\delta) + p_d - \sigma K}{\rho_\ell R_g T_\delta} \right] \quad (3.11)$$

Equation (3.11) reflects the fact that under the influence of the disjoining and capillary pressures, the liquid free surface saturation pressure $(p_{\text{sat}})_\delta$ is different from the normal saturation pressure $p_{\text{sat}}(T_\delta)$ and varies along the thin film (or s -coordinate), while p_v and T_v are the same for any value of s at a given z -location. This is also due to the fact that T_δ changes along s .

For a thin evaporating film, the difference between $(p_{\text{sat}})_\delta$ given by equation (3.11) and that for a given T_δ using the saturation curve table is larger. This difference is the reason for the existence of the thin nonevaporating superheated film, which is in the equilibrium state in spite of the fact that $T_\delta > T_v$.

Under steady-state conditions the right-hand sides of equations (3.1) and (3.9) can be equated.

$$T_\delta = T_w + \frac{\delta}{k_\ell} \left(\frac{2\alpha}{2 - \alpha} \right) \frac{h_{fg}}{\sqrt{2\pi R_g}} \left[\frac{p_v}{\sqrt{T_v}} - \frac{(p_{\text{sat}})_\delta}{\sqrt{T_\delta}} \right] \quad (3.12)$$

Equations (3.11) and (3.12) determine the interfacial temperature, T_δ , and pressure, $(p_{\text{sat}})_\delta$. T_w has to be provided as an input to the solution procedure, resulting from the solution of the heat conduction problem in the fin between the grooves. The four boundary conditions for equations (3.5) and (3.6) must be developed taking the

physical situation into account, as shown in the following sections.

As the liquid film thins, the disjoining pressure, p_d , and the interfacial temperature, T_δ , increase. Under specific conditions, a nonevaporating film thickness is present which gives the equality of the liquid-vapor interface and the solid surface temperatures, $T_\delta = T_w$. This is the thickness of the equilibrium nonevaporating film δ_0 , which can be determined from equations (3.11) and (3.12). For a nonevaporating equilibrium film ($q = 0$), it follows from equation (3.12) that

$$(p_{\text{sat}})_\delta = p_v \sqrt{\frac{T_w}{T_v}} \quad (3.13)$$

Substitution of equations (3.7) and (3.13) into equation (3.11) gives

$$\delta_0 = \left\{ \frac{1}{A'} \left[p_v \sqrt{\frac{T_w}{T_v}} - p_{\text{sat}}(T_w) - \rho_\ell R_g T_w \ln \left(\frac{p_v}{p_{\text{sat}}(T_w)} \sqrt{\frac{T_w}{T_v}} \right) - \sigma K \right] \right\}^{-1/B} \quad (3.14)$$

For water, the following equation for the disjoining pressure was used (Holm and Goplen, 1979)

$$p_d = \rho_\ell R_g T_\delta \ln \left[a \left(\frac{\delta}{3.3} \right)^b \right] \quad (3.15)$$

where $a = 1.5336$ and $b = 0.0243$. The thickness of the equilibrium film is given for water by

$$\delta_0 = 3.3 \left\{ \frac{1}{a} \exp \left[\frac{p_{\text{sat}}(T_w) - p_v \sqrt{T_w/T_v} + \sigma K}{\rho_\ell R_g T_w} + \ln \left(\frac{p_v}{p_{\text{sat}}(T_w)} \sqrt{\frac{T_w}{T_v}} \right) \right] \right\}^{1/6} \quad (3.16)$$

3.4 Heat Transfer in the Thin-Film Region of the Evaporator

This problem has been treated numerically and experimentally by different authors, whose results are mentioned here to understand the basis of the present model. Kamotani (1978), Holm and Goplen (1979), and Stephan and Busse (1992) modeled an evaporating extended meniscus in a capillary groove (Fig. 3.1). In all of the above papers, it is emphasized that most of the heat is transferred through the region where the thickness of the liquid layer is extremely small. The significance of the temperature difference between the saturated vapor core and the interface has been stressed by Solov'yev and Kovalev (1984) and Stephan and Busse (1992). In the mathematical models of the above authors, the solid surface was assumed to be smooth. Kamotani (1978) noted that this assumption and, generally including of the heat transfer in the microfilm region in the model could lead to an overestimation of the total heat transfer coefficient. The same concern has been expressed by Vasiliev et al. (1981).

In light of these findings, in the present analysis the difference between the

saturated vapor temperature and that of the free liquid surface was considered, and the existence of the surface roughness and its influence on evaporative heat transfer was taken into consideration. In general, manufacturing processes always leave some degree of roughness on the metallic surface. Alloys of copper, brass, steel and aluminum invariably have some distinct grain structure, resulting from processing the materials. In addition, corrosion and deposition of some substances on the surface can influence its microrelief. This means the solid surface is totally covered with microroughnesses, where the characteristic size may vary from, for example, $R_r = 10^{-8}$ to 10^{-6} m. Apparently, the thin liquid film formation can be affected by some of these microroughnesses. It can be assumed that at least some part of a single roughness fragment, on which the thin film formation takes place, has a circular cross section and is extended in the z -direction due to manufacturing the axial grooves (Fig. 3.2).

In the present analysis the free liquid surface is divided into four regions (Fig. 3.2). The first region is the equilibrium nonevaporating film. The second (microfilm) region ranges in the interval $\delta_0 \leq \delta \leq \delta_1$, where the increase of the liquid film thickness up to the value δ_1 is described by equations (3.5) and (3.6). In this region, the generalized capillary pressure $p_{\text{cap}} \equiv \sigma K - p_d$ (here p_{cap} was defined so that its value is positive) is changing drastically along the s -coordinate from the initial value up to an almost constant value at point s_1 , where the film thickness, δ_1 , is large enough to neglect the capillary pressure gradient. It is useful to mention that some

investigators have denoted this microfilm region as the "interline region." The third (transition) region, where the liquid-vapor interface curvature is constant, is bounded by $\delta_1 < \delta \leq R_r + \delta_0$, and the local film thickness is determined by the geometry of the solid surface relief and the value of the meniscus radius R_m . In the fourth (meniscus) region, where by definition $\delta > R_r + \delta_0$, the local film thickness can be considered independent of the solid surface microrelief. In the third and fourth regions, the heat transfer is determined by heat conduction in the meniscus liquid film and the metallic fin between the grooves. However, in the second region, the temperature gradient in the solid body can be neglected in comparison to that in liquid due to the extremely small size of this region.

The total heat flow rate per unit groove length in the microfilm region is defined as

$$Q'_{\text{mic}}(s_1) = \int_0^{s_1} \frac{T_w - T_\delta}{\delta/k_\ell} ds \equiv \int_0^{s_1} q ds \quad (3.17)$$

Equations (3.5)–(3.8), (3.11) and (3.12) must be solved for four variables: δ , δ' , p_{cap} and $Q'_{\text{mic}}(s)$ in the interval from $s = 0$ to the point $s = s_1$, where p_{cap} can be considered to be constant. Now, instead of the two second-order equations (3.5) and (3.6), the following four first-order equations should be considered with their respective boundary conditions:

$$\frac{d\delta}{ds} = \delta' \quad (3.18)$$

$$\frac{d\delta'}{ds} = \left(1 + \delta'^2\right)^{3/2} \left(\frac{p_{\text{cap}} - A'\delta^{-B}}{\sigma} + \frac{1}{R_r} \right) \quad (3.19)$$

$$\frac{dp_{\text{cap}}}{ds} = -\frac{3\nu_\ell}{h_{fg}\delta^3} Q'_{\text{mic}}(s) \quad (3.20)$$

$$\frac{dQ'_{\text{mic}}}{ds} = \frac{T_w - T_\delta}{\delta/k_\ell} \quad (3.21)$$

$$\delta|_{s=0} = \delta_0 \quad (3.22)$$

$$\delta'|_{s=0} = 0 \quad (3.23)$$

$$p_{\text{cap}}|_{s=0} = -\frac{\sigma}{R_r + \delta_0} + A'\delta_0^{-B} \quad (3.24)$$

$$Q'_{\text{mic}}|_{s=0} = 0 \quad (3.25)$$

The value of δ_0 is found from equation (3.14), where $K = -1/R_r$.

Though the initial-value problem, equations (3.18)–(3.25) is completely determined, its solution must satisfy one more condition:

$$p_{\text{cap}}|_{s=s_1} = \frac{\sigma}{R_m} \quad (3.26)$$

Since the only parameter which is not fixed in this problem is connected with the surface roughness characteristics, the boundary condition (3.26) can be satisfied by the choice of R_r . Physically, it means that the beginning of the evaporating film is shifted along the rough surface depending on the situation so as to satisfy the conservation laws. However, in a smooth surface model ($R_r \rightarrow \infty$) the solution will probably not satisfy equation (3.26). As a result of this problem, the values of δ_1 and $Q'_{\text{mic}}(A_1)$ can be determined and the transition region can be considered, provided that $\delta_1 < R_r$, where the free liquid surface curvature is constant and its radius R_m is many times larger than R_r . Based on the geometry shown in Fig. 3.2, the following approximation for the liquid film thickness in the transition region $x_f \leq x \leq x_{tr}$ is given:

$$\delta = \delta_0 + R_r - \sqrt{R_r^2 - x^2} - R_m + \left(R_m^2 + x^2 + 2R_m x \sin \theta_f\right)^{1/2} \quad (3.27)$$

Equation (3.27) is valid for the rough surface model (θ_f can be set equal to zero for very small R_r) and also the smooth surface model in the meniscus region ($R_r \rightarrow \infty$ and θ_f is given as a result of the microfilm problem solution).

The heat flow rate per unit groove length in the transition region is

$$Q'_{tr} = \int_{x_f}^{x_{tr}} \frac{T_w - T_\delta}{\delta/k_\ell} dx \quad (3.28)$$

where x_f and x_{tr} are obtained from equation (3.27) provided $\delta = \delta_1$ and $\delta = R_r + \delta_0$, respectively.

Now the connecting point between the transition and meniscus regions must be considered. At this point, the film thickness, the free surface curvature, and the liquid surface slope angle must coincide from both sides. In the rough surface model, the last condition is always satisfied because the length of the microfilm region is smaller than R_r , and the rough fragment with the film can be “turned” around its center in the needed direction (see Fig. 3.2). In other words, because of the circular geometry of the rough fragment and the constant temperature of the solid surface in the microfilm region, the slope of the film free surface is not fixed in the mathematical model. On the contrary, in the smooth surface model the numerical results give θ_f which is generally not equal to θ_{men} determined by the fluid flow along the groove. Stephan (1992) seems to have answered this contradiction using a rounded fin corner, however, this explanation is not completely satisfactory. Note that in the situation when $\theta_f \neq \theta_{men}$, the smooth surface model can be used along with the rounded fin corner, where the radius is R_{fin} . In this case equation (3.27) can also be used provided R_r is changed to R_{fin} .

It is useful to mention here that the values of R_m and θ_{men} are connected

by the geometric relation $\theta_{\text{men}} = \arccos(W/R_m) - \gamma$ and should be given as a result of the solution of the problem for the fluid transport along the groove. The fin top temperature T_w should be defined from the consideration of the heat conduction problem in the fin between grooves and in the meniscus liquid film discussed below.

Simplified model of heat transfer in the evaporating thin film. The free liquid surface curvature K in the microfilm region varies from the initial value to that in the meniscus region. Its variation is described by equations (3.18)–(3.26) with respect to the p_{cap} and p_d definitions. In spite of a sharp maximum which the K function has in the microfilm region, its variation only slightly affects the total heat transfer coefficient. To check this hypothesis numerically, a simplified version of the heat transfer model of the microfilm region was developed, where it was assumed that the microfilm free surface curvature is equal to that in the meniscus region. Therefore, instead of solving equations (3.18)–(3.26), the microfilm thickness in this region (and also in the transition region) can be given by equation (3.27) for the interval $0 \leq x \leq x_{tr}$. In this case, the heat flow rate per unit groove length in both the microfilm and transition regions is

$$Q'_{\text{mic}} + Q'_{tr} = \int_0^{x_{tr}} \frac{T_w - T_\delta}{\delta/k_\ell} dx \quad (3.29)$$

3.5 Heat Transfer in the Thin Film Region of the Condenser

Heat transfer during condensation on a grooved surface has been considered by Kamotani (1976b) and Babenko et al. (1981) for the case of rectangular and trapezoidal fins with rounded corners, respectively, with the assumption that $T_\delta = T_v$. Analyzing their results, the following conclusions are made, which lead to the simplification of equations (3.5) and (3.6):

1. The surface of the liquid film is smooth and the film thickness variation along s -coordinate is weak (see Fig. 3.1):

$$\left(\frac{d\delta}{ds}\right)^2 \ll 1$$

2. The disjoining pressure gradient along the film flow can be neglected in comparison to that of the capillary pressure due to the surface tension force because of the large film thickness.

Taking the above points into consideration, and substituting equation (3.6) into equation (3.5) gives the following differential equation for the film thickness at the top of the fin between grooves:

$$\delta \frac{d}{ds} \left[\delta^3 \left(\frac{d^3 \delta}{ds^3} + \frac{dK_w}{ds} \right) \right] = \frac{3\mu_\ell k_\ell}{\sigma h_{fg} \rho_\ell} (T_\delta - T_w) \quad (3.30)$$

The boundary conditions for equation (3.30) at $s = 0$ are

$$\frac{d\delta}{ds} = 0; \quad \frac{d^3 \delta}{ds^3} = 0 \quad (3.31)$$

These conditions imply that the thickness and curvature of the film are symmetric around $s = 0$. For small κ (see Fig. 3.1(a)) at $s = L_2$, the curvature of the film and its surface slope angle are determined by the radius of the meniscus in the groove:

$$\frac{d^2 \delta}{ds^2} = \frac{1}{R_m} \quad (3.32)$$

$$\frac{d\delta}{ds} = \tan \left(\kappa - \arcsin \frac{W}{R_m} + \arcsin \frac{L_1}{R_v} \right) \quad (3.33)$$

where L_2 is the length of the film, which is equal to L_1 in the case of a flat fin top geometry (Fig. 3.1). The boundary value problem, equations (3.30)–(3.33), is solved approximately by introducing the following polynomial function for the film thickness:

$$\delta(s) = C_0 + C_1(s - L_2) + C_2(s - L_2)^2 + C_3(s - L_2)^3 + C_4(s - L_2)^4 \quad (3.34)$$

From the boundary conditions (3.31)–(3.33) the values of the coefficients are

$$C_1 = \tan \left(\kappa - \arcsin \frac{W}{R_m} + \arcsin \frac{L_1}{R_v} \right), \quad C_2 = \frac{1}{2R_m}$$

$$C_3 = \frac{2C_2L_2 - C_1}{2L_2^2}, \quad C_4 = \frac{C_3}{4L_2}$$

At the point $s = L_2$, where the thickness of the film is usually at a minimum, equation (3.30) must be satisfied exactly, and the total mass flow rate of the condensate due to the surface tension force must be equal to the total amount of fluid condensed in the region $0 \leq s \leq L_2$. Thus, integrating equation (3.30) we have

$$\frac{\sigma h_{fg} \rho_\ell}{3\mu_\ell} \left[\delta^3 \left(\frac{d^3 \delta}{ds^3} + \frac{dK_w}{ds} \right) \right]_{(s=L_2)} = k_\ell \int_0^{L_2} \frac{T_\delta - T_w}{\delta} ds \quad (3.35)$$

Substituting equation (3.34) into equation (3.35) and solving numerically for C_0 , the heat flow rate per unit groove length through the thin film region is

$$Q'_\delta = \int_0^{L_2} \frac{k_\ell(T_\delta - T_w)}{C_0 + C_1(s - L_2) + C_2(s - L_2)^2 + C_3(s - L_2)^3 + C_4(s - L_2)^4} ds \quad (3.36)$$

The fin top temperature T_w is given from the results of the heat conduction problem in the fin and the meniscus region. Equation (3.35) must also be solved within the following iterative procedure because of the influence of the film surface curvature and the disjoining pressure on T_δ . In the first iteration, T_δ is defined from equations (3.11) and (3.12) assuming that $K = \overline{K}_w$ and $p_d = 0$. In the second and following steps

$$K = \overline{K}_w + \frac{\overline{d^2 \delta}}{ds^2}$$

where the last term is calculated using the solution of the previous step for $\delta(s)$ and $p_d = p_d(\bar{\delta})$ (here the bar denotes an average value). While the influence of K on the presented results was negligible in comparison with the effect of the meniscus radius variation, it can be important for extremely thin films of condensate with large free surface curvatures, in which case the problem should be treated numerically in the frames of a more complicated analysis.

Now, the consideration of the meniscus region gives the opportunity to obtain the heat transfer coefficients.

3.6 Heat Conduction in the Metallic Fin and Meniscus Region Film

For low-temperature heat pipes, the thermal conductivity of the metallic casing is several hundred times higher than that of the liquid working fluid. Nearly all of the heat is transferred from the metallic fin between grooves to the saturated vapor or vice versa through a thin liquid film in the vicinity of the fin top. The temperature drop in the metallic fin is many times smaller than in the liquid film (Schneider et al., 1976; Stephan and Busse, 1992). Therefore, in the present analysis the temperature gradient in the metallic fin in the direction transverse to the x -coordinate is neglected (Fig. 3.1). The heat conduction in the metallic fin and meniscus liquid film is described

by the following equation, which was obtained as a result of an energy balance over a differential element (Vasiliev et al., 1981):

$$\frac{d^2T}{dx^2} + \frac{dT}{dx} \frac{\tan(\gamma + \chi)}{L_{\text{fin}}(x)} + (T_\delta - T) \frac{k_\ell}{k_w \delta(x) L_{\text{fin}}(x)} = 0 \quad (3.37)$$

The fin thickness variation is due to its wall inclination angle and the circular tube geometry

$$L_{\text{fin}}(x) = L_1 + x \tan(\gamma + \chi) \quad (3.38)$$

and the liquid film thickness is

$$\delta = \delta_2 - R_m + \left[R_m^2 + \frac{x^2}{\cos^2(\gamma + \chi)} + \frac{2R_m x}{\cos(\gamma + \chi)} \sin \theta_{\text{men}} \right]^{1/2} \quad (3.39)$$

where δ is measured perpendicularly from the liquid-vapor interface. Equations (3.37)–(3.39) are valid for the evaporator and condenser sections. However, the boundary conditions for equation (3.37) in these two sections are different, and the value of δ_2 should be chosen as follows:

$\delta_2 = R_r + \delta_0$ in the rough surface evaporation model,

$\delta_2 = \delta_1$ in the smooth surface evaporation model,

$\delta_2 = \delta|_{s=L_2}$ for the condenser heat transfer model.

The boundary conditions for equation (3.37) in the evaporator are

$$\left. \frac{dT}{dx} \right|_{x=0} = \frac{Q'_{\text{mic}} + Q'_{tr}}{k_w L_1} \quad (3.40)$$

$$\left. \frac{dT}{dx} \right|_{x=t_g} = \frac{q_e \pi R_o}{k_w N [L_1 + t_g \tan(\gamma + \chi)]} \quad (3.41)$$

where boundary condition (3.40) is written with the assumption that $x_{tr} \ll t_g$. For the simplified model, equation (3.37) was solved also in the microfilm and transition regions, where δ was given by equation (3.27) and the right-hand side of equation (3.40) was set equal to zero.

The boundary conditions for equation (3.37) in the condenser are

$$\left. \frac{dT}{dx} \right|_{x=0} = - \frac{Q'_\delta}{k_w L_1} \quad (3.42)$$

$$\left. \frac{dT}{dx} \right|_{x=t_g} = - \frac{q_c \pi R_o}{k_w N [L_1 + t_g \tan(\gamma + \chi)]} \quad (3.43)$$

While the values of Q'_{mic} , Q'_{tr} and Q'_δ depend on $T_w \equiv T|_{x=0}$, which is obtained from the solution of equations (3.37)–(3.43), this problem is to be solved in conjunction with those concerning heat transfer in the thin film regions.

The local heat transfer coefficient (for a given z) in the evaporator from the bottom of the groove surface to the vapor is

$$\bar{h}_{e,\text{bot}} = \frac{q_e}{[T|_{x=t_g} - T_v]} \frac{R_o}{R_v + t_t + t_g} \quad (3.44)$$

The local heat transfer coefficient from the external surface of the evaporator to the vapor is

$$\bar{h}_e = \left[\frac{R_o}{k_w} \ln \frac{R_o}{R_v + t_t + t_g} + \frac{1}{\bar{h}_{e,\text{bot}}} \frac{R_o}{R_v + t_t + t_g} \right]^{-1} \quad (3.45)$$

where the thermal resistance of the circular tube wall is taken into account.

For the condenser region, the heat transfer coefficients are defined in a similar manner:

$$\bar{h}_{c,\text{bot}} = - \frac{q_c}{[T|_{(x=t_g)} - T_v]} \frac{R_o}{R_v + t_t + t_g} \quad (3.46)$$

$$\bar{h}_c = \left[\frac{R_o}{k_w} \ln \frac{R_o}{R_v + t_t + t_g} + \frac{1}{\bar{h}_{c,\text{bot}}} \frac{R_o}{R_v + t_t + t_g} \right]^{-1} \quad (3.47)$$

3.7 Numerical Treatment

Equations (3.11) and (3.12) were simultaneously solved for T_δ (absolute error $\Delta_a = 0.0001$ K) and $(p_{\text{sat}})_\delta$ ($\Delta_a = 1$ Pa) for every point on s by means of Wegstein's iteration method (Lance, 1960). The system of the four first-order ordinary differential equations with four initial conditions and one constitutive condition describing the evap-

orating microfilm region, equations (3.18)–(3.26), were solved using the fourth-order Runge-Kutta procedure and the shooting method (on parameter R_r). The controlled relative error was less than 0.001% for each of the variables. The results obtained for comparatively small temperature drops through the thin film were compared with those from the simplified model. Since the agreement was good, the simplified model was used further in the prediction of the AGHP characteristics. Equation (3.35) was solved for C_0 by means of Muller's iteration method ($\Delta_a = 10^{-11}$ m), and the integration in equation (3.36) was made using Simpson's method. The heat conduction problem, equations (3.37)–(3.43), was also solved by the standard Runge-Kutta method ($\Delta_a = 0.0001$ K and $\Delta_r = 0.001\%$ for the functions T and dT/dx , respectively) along with equations (3.35) and (3.36) within the iterative procedure to find T_w ($\Delta_a = 0.0001$ K).

3.8 Results and Discussion

To verify the numerical results obtained, the experimental data provided by Schlitt et al. (1974) were used. Therefore, the presented results mostly refer to the AGHP with the following geometry: $L_t = 0.914$ m, $L_c = 0.152$ m, $0.15 \leq L_e \leq 0.343$ m, $W = 0.305$ mm, $t_g = 1.02$ mm, $L_1 = 0.215$ mm, $R_v = 4.43$ mm, $R_o = 7.95$ mm, $\gamma = 0$, $N = 27$, $\kappa = 0$, $t_t = 0$. The working fluids were ammonia and ethane, the casing material thermal conductivity was assumed to be $k_w = 170$ W/(m-K), $\alpha = 1$

(if another value is not indicated in the text), dispersion constant $A' = 10^{-21}$ J and $B = 3$.

The data in Figs. 3.3–3.5 were obtained for ammonia with a vapor temperature in the evaporator of $T_v = 250$ K and $\alpha = 1$. The solid surface superheat is $\Delta T = |T_w - T_v|$, and the results obtained using the simplified model for evaporating film are denoted as SIMPL.

Figure 3.3(a) shows the variations of the free liquid surface temperature along the evaporating film for $\Delta T = 0.047$ K, 0.070 K and 0.120 K, which are from the solutions of equations (3.7), (3.11)–(3.13), and (3.18)–(3.26) in the microfilm region. These results are compared to those obtained by the simplified model, where equations (3.7) and (3.11)–(3.13) were solved along with equations (3.27), (3.37) and (3.38) with the boundary conditions

$$T|_{x=0} = T_w, \quad \left. \frac{dT}{dx} \right|_{x=0} = 0$$

in the microfilm and transition regions for the same values of the roughness characteristic sizes ($R_r = 0.33 \mu\text{m}$, $1.0 \mu\text{m}$ and $R_r \rightarrow \infty$). It should be noted that the temperature drop in the solid body in these regions was negligible in the results of the simplified model in comparison to ΔT , and the equilibrium film thickness was defined within the assumption that its free surface curvature was equal to $1/R_m$. In the simplified model for the case of a smooth surface, the value of the contact angle

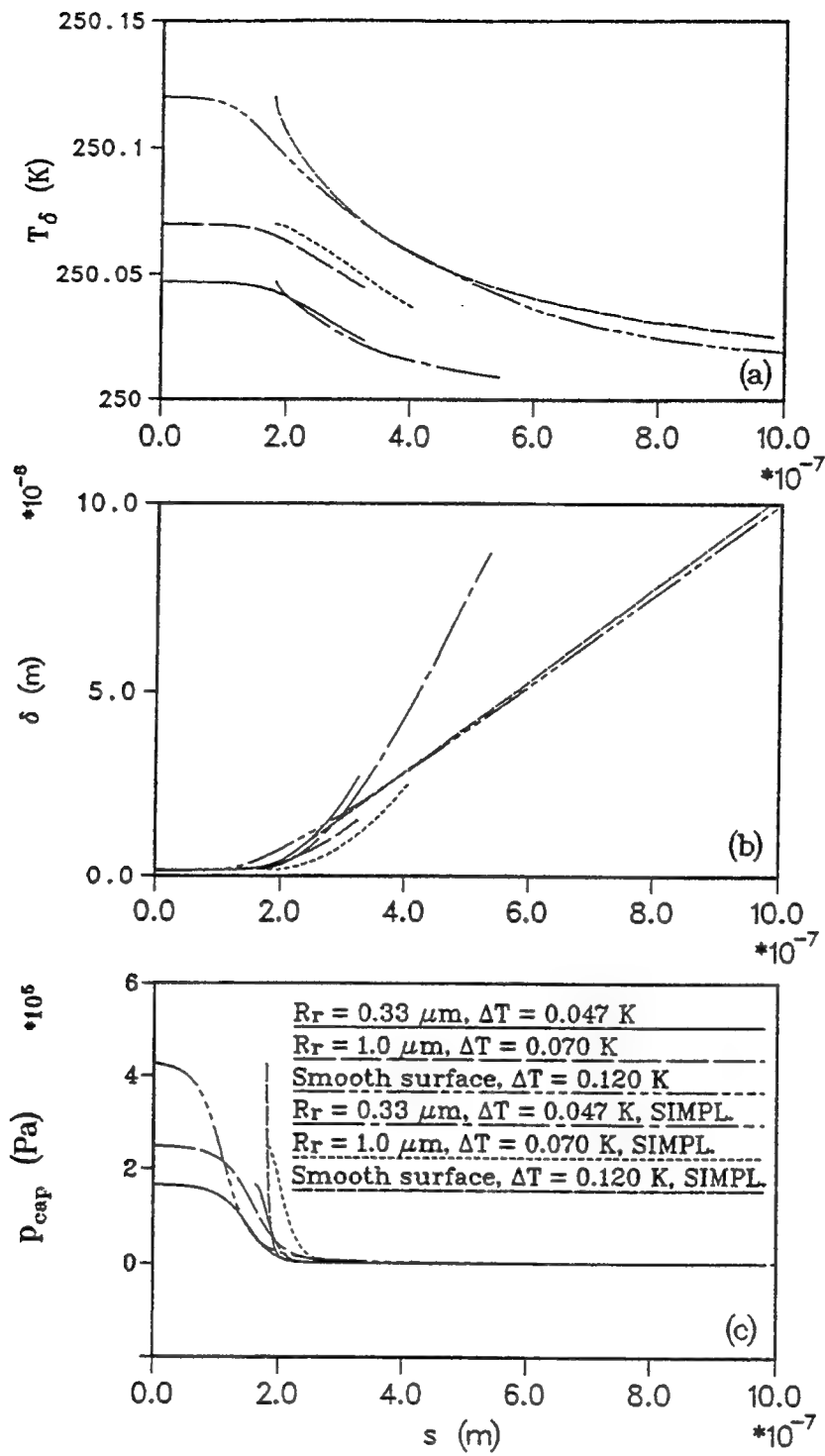


Figure 3.3: Characteristics of the evaporating film along the solid-liquid interface (ammonia, $T_v = 250$ K) (a) free liquid surface temperature, (b) thickness of the film, (c) generalized capillary pressure

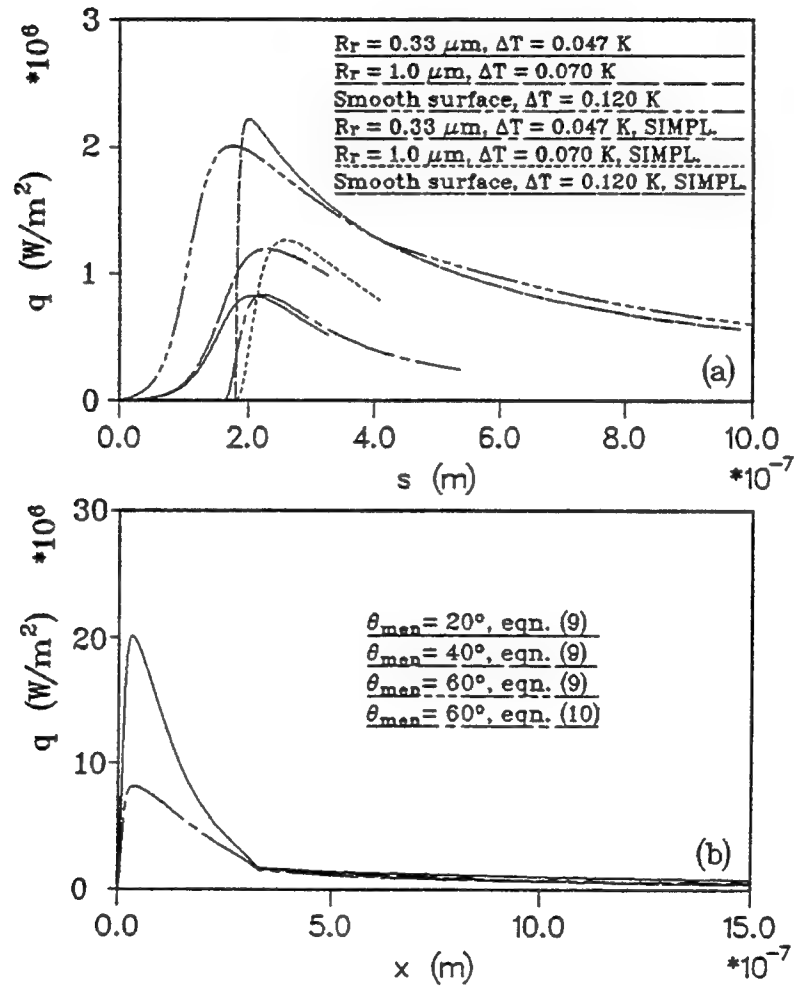


Figure 3.4: Heat flux through the evaporating film (ammonia, $T_v = 250 \text{ K}$, $\alpha = 1$)
(a) along the solid-liquid interface (microfilm region), (b) along the fin axis ($R_r = 0.33 \mu\text{m}$, $\Delta T = 1 \text{ K}$)

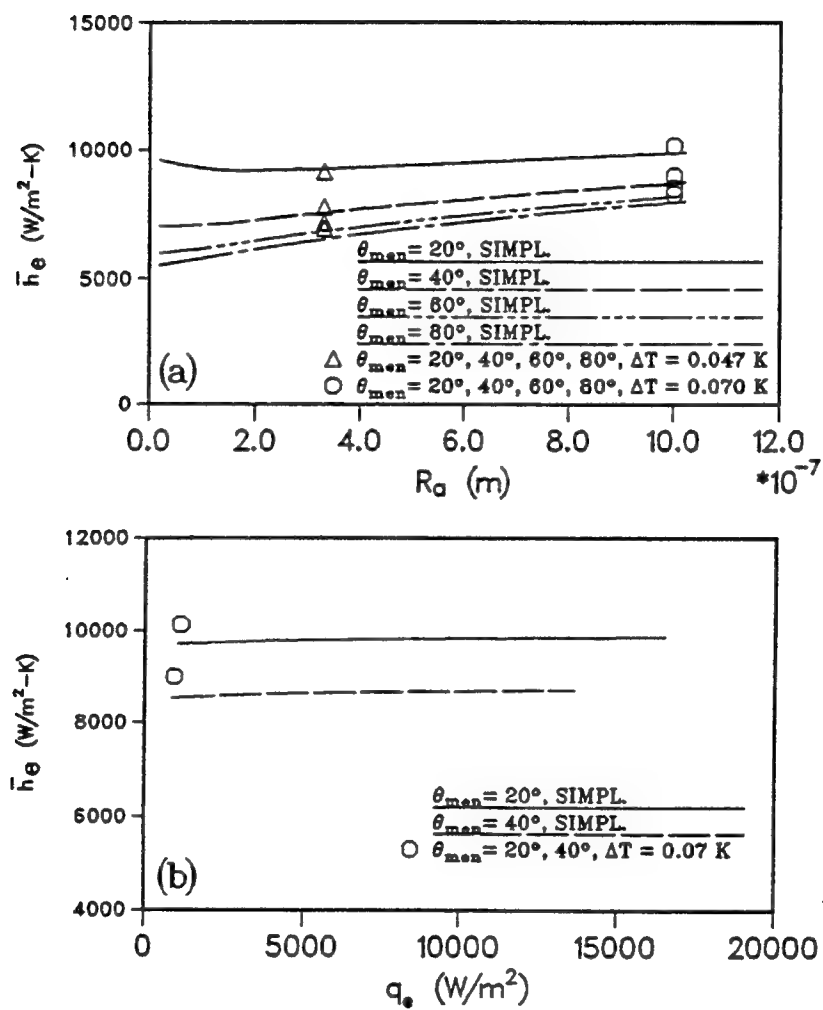


Figure 3.5: Local heat transfer coefficient in the evaporator of the ammonia-Al heat pipe ($T_v = 250$ K) (a) versus roughness size, (b) versus heat flux ($R_r = 1 \mu\text{m}$)

in the microfilm region was $\theta_f = 7^\circ$, which was given by the numerical solution of equations (3.18)–(3.26).

The corresponding variations of the film thickness δ and generalized capillary pressure p_{cap} are shown in the Figs. 3.3(b) and 3.3(c). The results obtained by the simplified model have been artificially shifted along the s -coordinate in these figures (and also in Fig. 3.4(a)) to make the comparison more understandable. Also, it should be noted that there is some difference between the s -coordinate and the x -coordinate used in the simplified model. The following relation has been used in the present paper: $s = R_r \arcsin(x/R_r)$.

In Fig. 3.3(a), the interval of T_δ variation along the evaporating film from the value of T_w to approximately T_v was more prolonged in comparison to the results by Stephan and Busse (1992), and the interfacial thermal resistance was still significant even when the film thickness was larger than $0.1 \mu\text{m}$. For a smaller characteristic size R_r , the film thickness increased more sharply along the solid surface (Fig. 3.3(b)), which is in agreement with equation (3.27). It should be mentioned that for the problem, equations (3.18)–(3.26) (unlike for the simplified model) R_r is not a parameter but the result of the numerical solution. The values of the maximum heat flux in the microfilm region were extremely high in comparison to those in the meniscus region (Fig. 3.4). For $\Delta T = 0.120 \text{ K}$, the generalized capillary pressure p_{cap} decreased from the initial value to the almost constant by approximately 5000

times (Fig. 3.3(c)). For a larger ΔT , this sharp decrease can cause some difficulties in the numerical treatment while solving equations (3.18)–(3.26); that is why the simplified model is useful. The simplified model has given the variation of p_{cap} along the film which is even more drastic because of the surface tension term is absent in the capillary pressure gradient (Fig. 3.3(c)). However, the decrease of the total heat flow rate in the microfilm region caused by this assumption was comparatively small, which is illustrated by Fig. 3.4(a). The distributions of the heat flux in the microfilm, transition and beginning of meniscus regions for different meniscus contact angles θ_{men} as predicted by the simplified model are presented in Fig. 3.4(b). The total heat flow through the meniscus region was significantly larger in comparison to that through the microfilm region. This means that while estimating the heat transfer coefficient for an evaporator element, shown in Fig. 3.1, the simplified model should provide the accuracy needed. To verify this, the numerical results for the local heat transfer coefficient \bar{h}_e in Fig. 3.5(a) have been obtained. The simplified model underestimated \bar{h}_e by only 5%, which enables its use when it is necessary to avoid the numerical difficulties mentioned above. The local evaporative heat transfer coefficient \bar{h}_e depends upon the meniscus contact angle θ_{men} , especially for small θ_{men} , and is practically independent of the heat flux on the external wall surface of the evaporator and also of ΔT , as shown in Fig. 3.5(b). The characteristic roughness size affected the value of \bar{h}_e , decreasing it up to 30% for $\alpha = 1$ in comparison to the value obtained

for the smooth solid surface. For large meniscus contact angle the influence of the roughness size on the heat transfer coefficient is at the maximum when R_r is close to the length of the microfilm region. For small values of the accommodation coefficient (for example for $\alpha = 0.05$) the effect of the surface roughness on the heat transfer is insignificant because the heat flux in the microfilm region in this case is comparatively small (Fig. 3.6).

The results of the present model were compared with the experimental data by Schlitt et al. (1974) and Ivanovskii et al. (1984) for the case of a small heat load applied to the AGHP (or evaporator). For a small heat load ($Q_a \ll Q_{\max}$) the values of the meniscus angle in both the evaporator and condenser of the AGHP under consideration are comparatively large: $\theta_{\text{men}} \geq 60^\circ$ in the evaporator and $\theta_{\text{men}} \geq 80^\circ$ in the condenser. This is valid because in the case without a heat load the grooves of an AGHP in the horizontal position are completely filled with liquid (i.e., the meniscus angle is close to 90°). For $\theta_{\text{men}} \geq 60^\circ$ the local evaporative heat transfer coefficients are practically independent on θ_{men} , as shown in Fig. 3.6. The values of the evaporative heat transfer coefficients (based on the outer tube diameter) obtained experimentally by Schlitt et al. (1974) and those reported by Ivanovskii et al. (1984) were also found to be independent of heat load, which resulted in a valid comparison, as given in Table 3.1. The agreement of the results for ammonia, ethane and water is good for $\alpha \ll 1$ since it was mentioned by Carey (1992, p. 119) that, for some

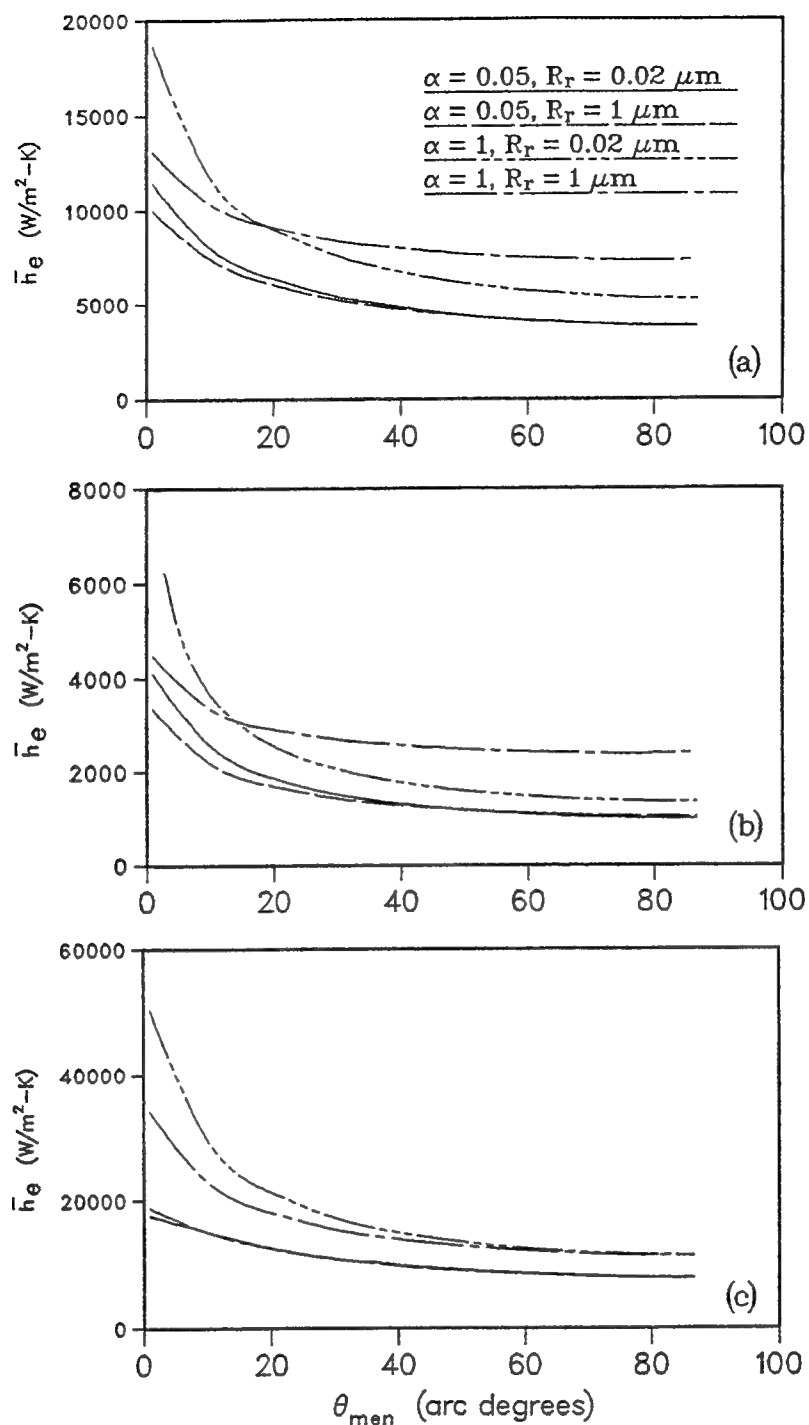


Figure 3.6: Effect of the meniscus contact angle on the local evaporative heat transfer coefficients ($\Delta T = 1$ K) (a) ammonia-Al heat pipe by Schlitt et al. (1974), ($T_v = 250$ K), (b) ethane-Al heat pipe by Schlitt et al. (1974), ($T_v = 200$ K), (c) water-copper evaporator by Ivanovskii et al. (1984), ($T_v = 300$ K)

Table 3.1: Comparison of the predicted \bar{h}_e with existing experimental data

Investigators	Schlitt et al. (1974)	Schlitt et al. (1974)	Ivanovskii et al. (1984)
Working fluid	Ammonia	Ethane	Water
T_v (K)	250	200	300
Casing material	Aluminum	Aluminum	Copper
Experimental value of \bar{h}_e (W/m ² -K)	3920	770	9500
Present prediction, \bar{h}_e (W/m ² -K), $\theta = 60^\circ, \alpha = 0.05$	4140	1180	8620

substances (ethanol, methanol, water, etc.), the accommodation coefficient had been found to have very small values (0.02 to 0.04) in the experiments by Paul (1962). The physical reason for low α values in the microfilm region of the evaporator can be the concentration of the contaminants which usually exist in a heat pipe in this region. For the case of $\alpha = 1$, the prediction gave significant (up to 100%) overestimations of \bar{h}_e even for a rough surface, as can be seen from Fig. 3.6. The experimental data by Ivanovskii et al. (1984) correspond to the case of evaporation of water from a copper plate with rectangular grooves for heat fluxes on the wall up to 20 W/cm² ($W = 0.17$ mm, $t_g = 0.8$ mm, $L_1 = 0.25$ mm, $L_e = 100$ mm, $T_v = 300$ K).

A comparison with the numerical data reported by Stephan and Busse (1992) has also been made for ammonia with: $T_v = 300$ K, $k_w = 221$ W/(m²-K), $A' = 2 \times 10^{-21}$ J, $\alpha = 1$, $L_1 = 0.5 \times 10^{-5}$ m, $W = 0.5 \times 10^{-3}$ m, $\gamma = 45^\circ$, $t_g = 0.5 \times 10^{-3}$ m, $R_v = 1$ m, $R_o = 1.0015$ m, $\theta_f = \theta_{\text{men}} = 19.7^\circ$, $\Delta T = 1.31$ K. The results of the comparison are listed in Table 3.2, which was prepared by Stephan and Busse (1992) except for the data of the present analysis. $T_{\delta v}$ is the temperature of the vapor side of the interface and Q'_{mic} is the heat flow rate per unit groove length in the region $0 \leq x \leq 1$ μm . The value of the heat transfer coefficient by Stephan and Busse (1992) was 23,000 W/(m²-K), while the result of the present numerical analysis is 17,385 W/(m²-K) for a rough surface (for $R_r = 0.02$ μm) and 23,900 W/(m²-K) for a smooth surface, which proves the validity of the present analysis.

Table 3.2: Comparison of the results with simplified models

Investigators	Present		Stephan and Busse (1992)		Schneider (1976)	Shekrladze (1987)
Assumption:	$T_\delta > T_v$	$T_\delta > T_v$	$T_{\delta v} > T_v$	$T_{\delta v} = T_v$	$T_\delta = T_v$	$T_\delta = T_v$
Surface:	rough	smooth	smooth	smooth	smooth	smooth
$T_w - T_v$ (K)	1.31	1.31	1.31	1.31	-	-
\bar{h}_e (W/cm ² -K)	1.74	2.39	2.3	7.9	6.9	3.9
q_e (W/cm ²)	2.56	3.69	3.0	10.4	-	-
$Q'_{\text{mic}}/Q'_{\text{tot}}$ (%)	37	38	45	94	-	-

The influence of the meniscus contact angle on the local heat transfer coefficient in the condenser (configuration by Schlitt et al. (1974)) is demonstrated in Fig. 3.7. The results agree qualitatively with those obtained by Babenko et al. (1981). The increase of the liquid surface curvature causes the strong decrease of the heat transfer coefficient, where a sharp maximum occurs in the vicinity of maximum θ_{men} . In this location, the heat transfer coefficient is also dependent on the temperature drop ΔT . In the numerical experiments the liquid film thickness was comparatively large (Fig. 3.7(a)) and the interfacial thermal resistance was negligible in comparison with that of the film. The values of the heat transfer coefficient in the condenser based on the outer tube diameter for the ammonia ($T_v = 250$ K) and ethane ($T_v = 200$ K) heat pipes reported by Schlitt et al. (1974) are 7600 and 3300 W/(m²-K), respectively. The numerical predictions were of the same order of magnitude as that reported by Schlitt et al. (1974).

3.9 Conclusions

The results of the numerical simulation of heat transfer during evaporation and condensation on the grooved surfaces of heat pipes are summarized as follows:

1. The validity of the present mathematical model for grooved evaporators has been confirmed, in general, by the comparisons with experimental

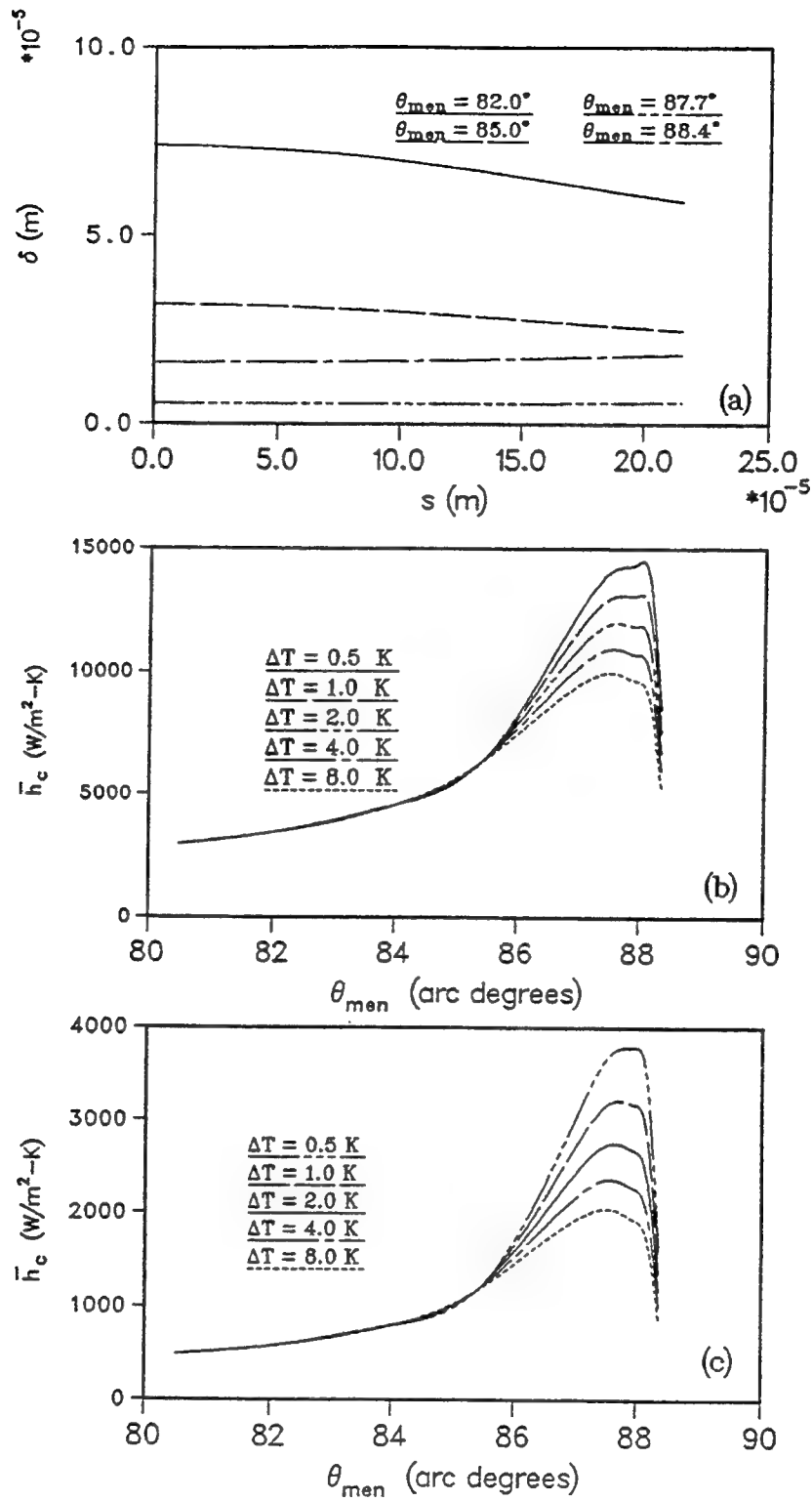


Figure 3.7: Effect of the meniscus contact angle in the heat pipe condenser on (a) liquid film thickness variation along the surface of the fin top (ammonia, $\Delta T = 1$ K, $T_v = 250$ K), (b) local heat transfer coefficient for ammonia ($T_v = 250$ K), (c) local heat transfer coefficient for ethane ($T_v = 200$ K)

data by Schlitt et al. (1974), Ivanovskii et al. (1984) and the numerical results by Stephan and Busse (1992). However, more detailed information concerning the values of the accommodation coefficients and dispersion constants is needed.

2. Accounting for the roughness of the solid surface in the thin evaporating film region resulted in a decrease of the heat transfer coefficient by up to about 30% in comparison to that obtained for a smooth surface for the case when the accommodation coefficient was set equal to unity. For $\alpha \ll 1$ the influence of the surface roughness on the evaporative heat transfer coefficient was insignificant.
3. The simplified model of evaporative heat transfer, where it was assumed that the free film surface curvature in the microfilm region was equal to that in the meniscus region, predicted values of the heat transfer coefficient only up to 5% smaller in comparison to the case where the curvature variation along the film was taken into account (for $\alpha = 1$).
4. The value of the local evaporative heat transfer coefficient (for a fixed θ_{men}) was practically independent of the heat flux on the evaporator external wall.
5. The interfacial resistance significantly influenced the value of the evaporative heat transfer coefficient. Therefore, the more advanced expressions

for this resistance during high intensive evaporation are needed.

6. The interfacial resistance and the disjoining pressure had negligible effects on the heat transfer in grooved condensers because of the large thickness of the liquid film, while the effect of the meniscus contact angle was significant.
7. Due to the fact that the greatest part of the heat flow through the liquid is transferred in the meniscus region where the liquid film is comparatively small, grooved evaporators are capable of withstanding comparatively high heat fluxes. While the model gives the values of the temperature drop in the liquid during evaporation, it provides an opportunity to predict the onset of the nucleate boiling in grooved evaporators.

In order to make the comparisons with experimental data more profound, the longitudinal variation of the meniscus angle should be taken into account. That means that the fluid circulation in an AGHP should be considered in conjunction with the present analysis.

Chapter 4

ANALYSIS OF MINIATURE GROOVED HEAT PIPES

4.1 Summary

A detailed mathematical model of axially-grooved heat pipes (AGHP) is developed in which the fluid circulation is considered along with the heat and mass transfer processes during evaporation and condensation. The predicted results obtained are compared to existing experimental data. Both capillary and boiling limitations are found to be important for the flat miniature copper-water heat pipe, which is capable of withstanding heat fluxes on the order of 40 W/cm^2 applied to the evaporator wall in the vertical position. The influence of the geometry of the grooved surface on the

maximum heat transfer capacity of the miniature AGHP is demonstrated.

4.2 Introduction

Some experimental data on the performance characteristics of the flat water-copper heat pipe with external dimensions $2 \times 7 \times 120$ mm has been reported by Plesch et al. (1991). The present chapter deals with the numerical prediction of the thermal characteristics of miniature and conventional axially-grooved heat pipes including the maximum heat flux on the outer evaporator wall. This heat flux is restricted by the fluid transport limit and boiling limitation. The superheat of the evaporating liquid, which is critical for the onset of nucleate boiling, depends on the heat transfer coefficient in the evaporator. Therefore, a detailed mathematical model is developed, including both the heat transfer through liquid films and axial fluid transport phenomena, which provides an opportunity to determine the maximum heat transfer capacity and thermal resistance of low-temperature AGHPs. The present model, which incorporates several one-dimensional boundary-value problems, has the following comparatively new features:

- The heat transfer through the liquid films and the fin between grooves (Fig. 4.1) in both the evaporator and condenser is accounted for in the model, which is described with respect to the disjoining pressure, interfacial thermal resistance

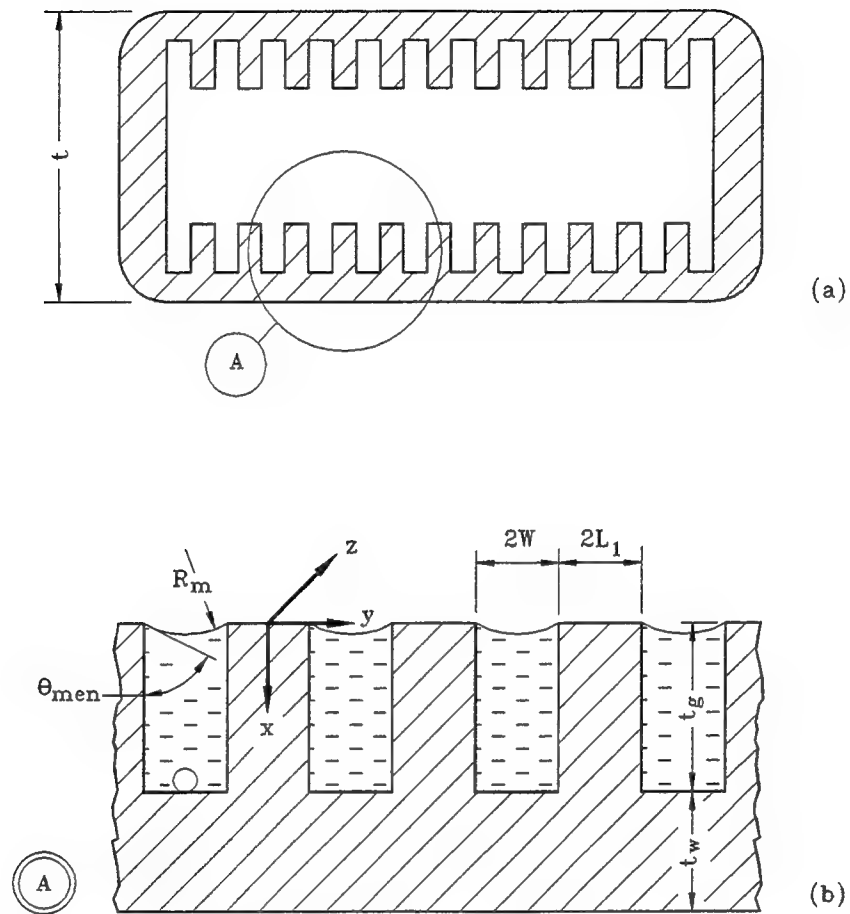


Figure 4.1: Flat miniature axially-grooved heat pipe cross sections

and surface roughness or curvature in the same manner as in Chapter 3.

- The effect of shear stresses at the free liquid surface in a groove due to the frictional liquid-vapor interaction on the liquid flow is taken into consideration.
- The boiling limitation and the thermal resistances of the evaporator and condenser are determined by accounting for the longitudinal distribution of the meniscus curvature, which is dependent on heat load and heat pipe inclination angle.

4.3 AGHP Mathematical Model

The mathematical model of a low-temperature AGHP is developed in order to optimize the performance of heat pipes and grooved evaporators and condensers for cooling systems. The proposed model is a significant contribution over the previous investigators' attempts (Kamotani, 1976b; and Vasiliev et al., 1981), where the heat transfer during evaporation in the microfilm and boiling limitation were not considered.

The present model is developed for rectangular and triangular (trapezoidal) grooves in circular or flat (rectangular) tubes, but other heat pipes and grooves configurations can also be described using the same general approach. Heat transfer processes in the heat pipe container and working fluid were considered to be one-

dimensional in the radial direction, such that axial heat conduction was neglected. It was also assumed that no puddle flow occurred in the AGHP, no part of the condenser was blocked by the liquid working fluid, the liquid was distributed uniformly between the grooves, and the fluid flow along the axis was related to the capillary potential gradient, as described by the main radius of curvature of the liquid in a groove.

The numerical results were obtained using an iterative mathematical procedure which involved the following problems:

1. Heat transfer in the evaporating film on a rough surface.
2. Heat transfer in the condensate film on the fin top surface.
3. Heat conduction in a metallic fin and liquid meniscus.
4. Fluid circulation in the AGHP.
5. Prediction of the onset of the nucleate boiling.

Since the first three problems are presented in detail in Chapter 3, their description is omitted here. However, these interconnected problems are included in the mathematical procedure along with the fluid circulation and boiling limitation equations presented in the following sections.

4.4 Fluid Circulation in an AGHP and the Capillary Limitation

The conservation equations for the steady-state operation of an AGHP are the continuity, momentum and energy equations for the liquid, vapor and wall, and the Laplace-Young equation for the radius of curvature at the liquid-vapor interface. At any axial location, the following mass conservation equation must hold over the cross section of the AGHP:

$$\bar{w}_v \rho_v A_v = N \bar{w}_\ell \rho_\ell A_\ell \equiv N \dot{m}_\ell \quad (4.1)$$

where \dot{m}_ℓ is the mass flow rate through a groove and N is the number of grooves. The average liquid and vapor velocities in the axial direction in equation (4.1) are

$$\bar{w}_\ell = \frac{1}{A_\ell} \int \int_{A_\ell} w_\ell(x, y) \, dx \, dy, \quad \bar{w}_v = \frac{1}{A_v} \int \int_{A_v} w_v(x, y) \, dx \, dy \quad (4.2)$$

An AGHP contains a definite amount of a working fluid M_t , which is distributed in accordance to the following relation, provided there is no excess liquid:

$$M_t = N \int_0^{L_t} \rho_\ell A_\ell \, dz + \int_0^{L_t} \rho_v A_v \, dz + M_\delta \quad (4.3)$$

where M_δ is the mass of the liquid film in the condenser section on top of the fins.

The conservation of axial momentum equation for an incompressible vapor flow using the one-dimensional boundary-layer approximation is

$$\frac{d}{dz}(p_v + \rho_v g z \sin \varphi + \rho_v \beta_v \bar{w}_v^2) = -f_v \frac{2\rho_v \bar{w}_v^2}{D_{h,v}} \quad (4.4)$$

where β_v is the momentum flux coefficient, f_v is the friction coefficient, and $D_{h,v}$ is the hydraulic diameter of the vapor channel. These coefficients for a circular vapor channel can be determined using the results of previous investigators for two-dimensional, laminar boundary-layer flow with suction or injection. For the range of radial Reynolds numbers usually seen in miniature AGHPs ($0 \leq \text{Re}_r < 20$) in the evaporator and adiabatic sections, the results given by Bankston and Smith (1973) can be approximated as follows:

$$(f \text{ Re})_v = 16 + 0.46\text{Re}_r - 0.017\text{Re}_r^2, \quad \beta_v = 1.33 - 0.005\text{Re}_r$$

In the condenser section (Bowman and Hitchcock, 1988; Jang et al., 1991)

$$(f \text{ Re})_v = 16[1.2337 - 0.2337\exp(-0.0363\text{Re}_r)][\exp(1.2\text{Ma})], \quad \beta_v = 1.33$$

The velocity of the liquid phase is very small in comparison to that of the vapor flow, so the interfacial shear for the vapor is computed by assuming the liquid to be stationary (Longtin et al., 1992). For a flat (rectangular) vapor channel configuration

the values of $(f \text{ Re})_v$ can be defined using the following equation (Shah and Bhatti, 1987)

$$(f \text{ Re})_v = 24(1 - 1.3553C + 1.9467C^2 - 1.7012C^3 + 0.9564C^4 - 0.2537C^5)$$

where $C = [t - 2(t_w + t_g)]/[N(W + L_1)]$ and the Reynolds number is based on the hydraulic diameter.

The axial transport of condensate in an AGHP takes place in the grooves, where most of the liquid resides. The thickness of the liquid film on the fin tops in the condenser section is assumed to be too small to contribute to the axial mass transport. Since the axial Reynolds number for liquid flow in an AGHP is usually less than 10, it can be considered to be viscous and quasi-one-dimensional. Thus, the conservation of momentum equation for the liquid flow in a groove with cross sectional area A_ℓ is

$$\frac{dp_\ell}{dz} + \rho_\ell g \sin \varphi = f_\ell \frac{2\rho_\ell \bar{w}_\ell^2}{D_{h,\ell}} \quad (4.5)$$

The values of f_ℓ can be taken from the numerical solution of the two-dimensional Stokes equation with boundary conditions which take into account shear stress in the liquid at the interface due to liquid-vapor frictional interaction (Vasiliev et al., 1981; Schneider and DeVos, 1980). The expression for the friction factor, given by Schneider and DeVos (1980) for rectangular grooves is used in the presented model

because of its reliability and accuracy. For the case of a planar free liquid surface geometry

$$(f \text{ Re})_\ell = (f \text{ Re})_{\ell 0} \left\{ 1 + \frac{4NW^3}{3\pi D_{h,v}^3} (f \text{ Re})_v \frac{\nu_v}{\nu_\ell} \left[1 - 1.971 \exp\left(-\frac{\pi t_g}{2W}\right) \right] \right\}$$

where $(f \text{ Re})_{\ell 0}$ corresponds to the case of no liquid-vapor interaction

$$(f \text{ Re})_{\ell 0} = 8t_g^2 \left[W^2 \left(1 + \frac{t_g}{W} \right)^2 \left(\frac{1}{3} - \frac{64W}{\pi^5 t_g} \tanh \frac{\pi t_g}{2W} \right) \right]^{-1}$$

Accounting for the liquid-vapor interaction seems to be important, especially for a flat miniature AGHPs.

The conservation of energy equation is cast into a form which reflects the change in the axial mass flow rate of liquid due to evaporation and condensation

$$\frac{d}{dz}(\rho_\ell \bar{w}_\ell A_\ell) = \begin{cases} \frac{2\pi R_o}{Nh_{fg}} h_{o,e} (T_{o,e} - T_v) \left(1 + \frac{h_{o,e}}{\bar{h}_e} \right)^{-1}, & 0 \leq z \leq L_e \\ 0, & \text{(adiabatic section)} \quad L_e < z < L_e + L_a \\ \frac{2\pi R_o}{Nh_{fg}} h_{o,c} (T_{o,c} - T_v) \left(1 + \frac{h_{o,c}}{\bar{h}_c} \right)^{-1}, & L_e + L_a \leq z \leq L_t \end{cases} \quad (4.6)$$

$\bar{h}_e(z)$ and $\bar{h}_c(z)$ are the mean local effective heat transfer coefficients between the external surface of the casing and vapor through the wall and liquid films (Khrustalev and Faghri, 1993). $h_{o,e}$ and $h_{o,c}$ are the heat transfer coefficients between the wall and the ambient. The vapor temperature is denoted by T_v . For a given axial heat

load function $Q(z)$, equation (4.6) can be rewritten as

$$\frac{d}{dz}(\rho_\ell \bar{w}_\ell A_\ell) = \frac{1}{h_{fg} N} \frac{dQ(z)}{dz} \quad (4.7)$$

The interfacial radius of the meniscus curvature is related to the pressure difference between the liquid and vapor by the Laplace-Young equation, which, in differential form, is

$$\frac{dp_\ell}{dz} = \frac{dp_v}{dz} - \frac{d}{dz} \left(\frac{\sigma}{R_m} \right) \quad (4.8)$$

The mean axial liquid and vapor velocities at the evaporator and condenser end caps are

$$\bar{w}_\ell|_{z=0} = \bar{w}_v|_{z=0} = 0 \quad (4.9)$$

$$\bar{w}_\ell|_{z=L_t} = \bar{w}_v|_{z=L_t} = 0 \quad (4.10)$$

which are imposed by the axial heat load function $Q(z)$. The vapor and liquid pressures at the evaporator end cap are

$$p_v|_{z=0} = p_{v0}, \quad p_\ell|_{z=0} = p_{v0} - \frac{\sigma}{R_{m0}} \quad (4.11)$$

The values of p_{v0} and R_{m0} are to be determined using additional conditions. When

solving equation (4.6), where $T_v(z)$ is also unknown and depends on p_v , the value of p_{v0} must be chosen such as to satisfy equation (4.10). When $Q(z)$ and T_{v0} are known, $p_{v0} = p_v(T_{v0})$, which can be obtained using the saturation tables. When there is an insufficient liquid fill volume, the radius of curvature of the meniscus at the evaporator end cap, R_{m0} , is found using equation (4.3), since the value of R_{m0} influences the axial distribution of liquid. In general, the radius of curvature of the meniscus is bounded by $R_{m,\min} \leq R_{m0} \leq R_v$. Since in the presented numerical experiments the situation of a sufficient liquid charge was considered, the following conditions for R_{m0} definition were used

$$\min\left\{\frac{1}{R_m(z)}\right\} = \frac{1}{R_v}; \quad \min\left\{\frac{1}{R_m(z)}\right\} = 0 \quad (4.12)$$

for circular and flat heat pipes, respectively. Equation (4.12) implies that for a given $Q(z)$, the value of R_{m0} which provides the equality of R_m to the vapor channel radius (for the circular tube case) at a single location on z along the AGHP should be chosen, while equations (4.4)–(4.11) are satisfied along the entire length of the AGHP. Note that this point is not always situated at the condenser end cap.

The solution of equations (4.4)–(4.11) gives the longitudinal distribution of the meniscus radius $R_m(z)$ and hence the meniscus contact angle $\theta_{\text{men}}(z)$, which are related for contact angles of $\theta_{\text{men}} \geq \theta_{\min}$ by

$$\theta_{\text{men}}(z) = \arccos \left[\frac{W}{R_m(z)} \right] - \gamma \quad (4.13)$$

For rectangular grooves $R_{m,\text{min}}$ is defined by equation (4.13) provided $\theta_{\text{men}} = \theta_{\text{min}}$, where θ_{min} is the minimum wetting contact angle, which is fixed for a specific working-fluid/container combination (Stepanov et al., 1977). This value of $R_{m,\text{min}}$ along with equation (4.12) determines the maximum heat transfer through an AGHP (capillary limit) at which equations (4.4)–(4.11) and the boundary conditions are still satisfied. For triangular (trapezoidal) grooves in the situation $\theta_{\text{men}} = \theta_{\text{min}}$, equation (4.13) gives the relation between the meniscus radius and the width of the liquid cross section.

When the longitudinal vapor pressure distribution, $p_v(z)$, and the temperature at the evaporator end cap, T_{v0} (for the case of an unknown heat load function) are found, the corresponding temperature distribution along the vapor flow, $T_v(z)$, can be calculated using the Clausius-Clapeyron equation.

4.5 Boiling Limitation and Heat Transfer Coefficients

Nucleation within the wick is undesirable for wicked heat pipe operation because the bubbles can obstruct the liquid circulation and hence cause hot spots on the evaporator walls. An estimation of the vapor bubble departure diameter during nucleate

boiling of water was made using the correlations obtained by Jensen and Memmel (1986). The bubble departure diameter was much larger than the groove width of the considered water-copper heat pipes, which means that the normal operation of an AGHP in the situation when nucleate boiling occurs in the evaporator is not realistic except for some special cases. Thus, for heat pipe performance optimization, it is necessary to predict the value of the heat flux which initiates vapor bubble formation in the working liquid. This task can be subdivided into two independent parts:

1. Estimation of the superheat of the liquid in the wick ($T_{\text{bot},\ell} - T_v$) which causes generation of vapor bubbles at the wall-wick interface. Here $T_{\text{bot},\ell}$ corresponds to the plane $x = t_g$ (Fig. 4.1(b)).
2. Computation of the heat transfer coefficient in the evaporator (\bar{h}_e) for the situation when no boiling occurs, which relates the values of the heat flux (q_e) and temperature drop across the wick ($T_{\text{bot},\ell} - T_v$).

Critical liquid superheat. A review on heterogeneous nucleation and bubble growth in liquids has been recently given by Carey (1992). Since the inner surface of heat pipes are invariably covered with machine-formed pits, cavities and scratches, vaporization usually begins on these irregularities. The process of bubble formation depends upon the solid surface microrelief, wetting contact angles and liquid properties. While theoretical prediction of the superheat which causes boiling

is extremely difficult, some empirical correlations should be involved in the analysis. Note that the vapor bubble embryo diameter is much smaller than the groove width, therefore, some of the correlations obtained for planar surfaces can be used in the present analysis.

Lorenz et al. (1974) reported experimental data for boiling of four different liquids on a copper surface with a #240 (sandpaper) finish. In these experiments, the number of active sites per square centimeter (\dot{n}), which increased rapidly with superheat, were determined by visual counting at different superheat values. Experimental results by Lorenz et al. (1974) can be approximated by the following equation

$$\dot{n} = C_1 - C_2 \left[\frac{h_{fg}(T_{\text{bot},\ell} - T_v)\rho_v}{2\sigma T_v} + \frac{1}{2R_m} \right]^{-1} \quad (4.14)$$

where for water $C_1 = 77$, $C_2 = 19 \times 10^6$ and $1 \leq \dot{n} \leq 6$, and for R-113, methanol and benzene $C_1 = 39.6$, $C_2 = 19.6 \times 10^6$ and $0.5 \leq \dot{n} \leq 10$. Note that in the analysis by Lorenz et al. (1974) $T_{\text{sat}}(p_\ell)$ was used instead of T_v and $1/R_m$ was equal to zero. The following relation between $T_{\text{sat}}(p_\ell)$ and T_v was used in the derivation of equation (4.14) (Carey, 1992, p.181)

$$T_v - T_{\text{sat}}(p_\ell) = \frac{T_v \sigma}{h_{fg} \rho_v R_m}$$

with the assumptions that $\rho_v \ll \rho_\ell$ and $\sigma/\rho_\ell R_m \ll 1$. For a known superheat ($T_{\text{bot},\ell} - T_v$), equation (4.14) indicates whether boiling occurs at a given point along

the evaporator length, which is characterized by the local radius of curvature of the meniscus, R_m . The values of the heat flux on the external surface of the wall and the superheat are related as follows

$$q_e = \bar{h}_{e,\text{bot}}(T_{\text{bot},\ell} - T_v) \left(\frac{R_v + t_t + t_g}{R_o} \right) \quad (4.15)$$

where $\bar{h}_{e,\text{bot}}$ is the local effective heat transfer coefficient between the saturated vapor and the bottom of a groove, which is generally dependent on the value of R_m at this location.

Heat transfer coefficients. The coefficients of heat transfer during evaporation and condensation on the grooved surface were calculated using the mathematical model developed in Chapter 3. It is essential to mention that in the model given in Chapter 3 the thin film formation on the fin surface for both evaporation and condensation was described by the following equation:

$$\frac{1}{3\mu_\ell} \frac{d}{ds} \left[\delta^3 \frac{d}{ds} (p_d - \sigma K) \right] = \frac{k_\ell (T_w - T_\delta)}{h_{fg} \rho_\ell \delta} \quad (4.16)$$

where s is the coordinate along the solid-liquid interface where the temperature is T_w , and δ is the local film thickness. The temperature of the liquid-vapor interface T_δ is affected by the disjoining and capillary pressures, and also depends on the value of the interfacial resistance, which is defined for the case of a comparatively small heat flux by the following relation

$$q = - \left(\frac{2\alpha}{2 - \alpha} \right) \frac{h_{fg}}{\sqrt{2\pi R_g}} \left[\frac{p_v}{\sqrt{T_v}} - \frac{(p_{\text{sat}})_\delta}{\sqrt{T_\delta}} \right] \quad (4.17)$$

p_v and $(p_{\text{sat}})_\delta$ are the saturation pressures corresponding to T_v in the bulk vapor and at the thin liquid film interface, respectively. The extended Kelvin equation which relates p_d , $p_{\text{sat}}(T_\delta)$ (normal saturation pressure corresponding to T_δ), and $(p_{\text{sat}})_\delta$ was also used in the model. The following equations for the disjoining pressure were used in the present model for nonpolar liquids and for water, respectively:

$$p_d = -A'\delta^{-B} \quad (4.18)$$

$$p_d = \rho_\ell R_g T_\delta \ln \left[a \left(\frac{\delta}{3.3} \right)^b \right] \quad (4.19)$$

where $a = 1.534$ and $b = 0.0243$. Solution of the heat conduction equation in the fin and liquid in conjunction with the equations for the thin film formation for a given q_e gives the temperature of the fin bottom as $T|_{x=t_g} = T_{\text{bot},\ell}$. The local heat transfer coefficient from the bottom of the groove to the vapor is defined as

$$\bar{h}_{e,\text{bot}} = \frac{q_e}{[T|_{x=t_g} - T_v]} \left(\frac{R_o}{R_v + t_t + t_g} \right) \quad (4.20)$$

The local heat transfer coefficient from the external surface of the heat pipe to the vapor is

$$\bar{h}_e = \left[\frac{R_o}{k_w} \ln \left(\frac{R_o}{R_v + t_t + t_g} \right) + \frac{1}{\bar{h}_{e,\text{bot}}} \left(\frac{R_o}{R_v + t_t + t_g} \right) \right]^{-1} \quad (4.21)$$

where the thermal resistance of a circular tube wall is taken into account. It was found in the results by Khrustalev and Faghri (1993) that for $\alpha = 1$ the values of \bar{h}_e for the rough solid surface were up to 30% less than for the smooth solid surface. However, for the case of small α (for example, $\alpha = 0.05$) the influence of the roughness on the evaporative heat transfer coefficient was insignificant. The characteristic roughness size R_r in the referred results varied from 0.02 to 1 μm . Obviously, equations (4.15), (4.20) and (4.21) are valid also for a planar evaporator in which $R_o \rightarrow \infty$, $R_v \rightarrow \infty$ and $R_o = R_v + t_t + t_g + t_w$.

In the present analysis the values of $\bar{h}_{e,\text{bot}}$ were calculated for every point along the axial direction in the evaporator of the modeled AGHPs for a given total heat load Q_a , and equation (4.14) was used with the corresponding R_m to predict the onset of nucleate boiling ($\dot{n} \geq 1$). The mean temperature drop in the evaporator was calculated using the following expression:

$$T_{w,o} - T_v = \frac{1}{2\pi R_o L_e} \int_0^{L_e} \frac{dQ}{dz} \frac{1}{\bar{h}_e} dz \quad (4.22)$$

For the condenser section similar expressions were used.

4.6 Numerical Treatment

For the fluid circulation in the AGHP (equations (4.4)–(4.13)), the four main variables dependent on z to be found are

$K = R_m^{-1}$: curvature of the free surface of the meniscus,

$\dot{m} = \bar{w}_\ell \rho_\ell A_\ell$: mass flow rate of liquid in one groove,

p_ℓ : liquid pressure,

p_v : vapor pressure.

The system of four ordinary differential equations, equations (4.4), (4.5), (4.7) and (4.8), was solved with the respective boundary conditions using the fourth-order Runge-Kutta procedure and the shooting method (on parameter R_{m0}). For each of the four functions the relative error was less than 0.0001%. While in the present paper the AGHP for the case of a given axial heat load function $Q(z)$ was modeled, the structure of the numerical AGHP simulation was as follows:

1. The fluid circulation along the AGHP was solved with the known function $Q(z)$ and T_{v0} , which gave $R_m(z)$, $\theta_{\text{men}}(z)$ and $T_v(z)$.
2. For every point on z , the heat transfer in the evaporator and condenser thin film regions along with the heat conduction in the fin were solved and the functions $\bar{h}_e(z)$, $\bar{h}_{e,\text{bot}}(z)$, $\bar{h}_c(z)$ and $T_{w,o}(z)$ were determined.
3. The number of active sites \acute{n} was calculated for every point on z in the

evaporator with the corresponding R_m to determine whether boiling occurred.

4. The values of the temperature drops in the evaporator and condenser were found.
5. Steps 1–4 were repeated several times for larger values of Q_a until the capillary or boiling limitation was indicated (with the relative error less than 1%).

4.7 Results and Discussion

To verify the numerical results obtained, the experimental data provided by Schlitt et al. (1974) were first used. Therefore, part of the presented results refer to the AGHP with the following geometry: $L_t = 0.914$ m, $L_c = 0.152$ m, $0.15 \leq L_e \leq 0.343$ m, $W = 0.305$ mm, $t_g = 1.02$ mm, $L_1 = 0.215$ mm, $R_v = 4.43$ mm, $R_o = 7.95$ mm, $\gamma = 0$, $N = 27$, $t_t = 0$. The working fluids were ammonia and ethane, the casing material thermal conductivity was assumed to be $k_w = 170$ W/(m-K), and dispersion constant $A' = 10^{-21}$ J. The axial heat distribution was specified as

$$Q = \begin{cases} Q_a z / L_e, & 0 \leq z \leq L_e \\ Q_a, & L_e < z < L_e + L_a \\ Q_a \left(1 + \frac{L_e + L_a - z}{L_c} \right), & L_e + L_a \leq z \leq L_t \end{cases} \quad (4.23)$$

and equation (4.7), instead of equation (4.6), was used in the numerical procedure.

The longitudinal distribution of the meniscus contact angle, which is influenced by the inclination angle and the fluid pressure variation (Δp), is shown in Fig. 4.2(a) for ammonia ($L_e = 0.343$ m, $T_v = 250$ K). For positive values of the inclination angle φ (when the condenser end is elevated) the points of minimum and maximum liquid surface curvature (the so-called “dry” and “wet” points) were shifted from the ends of the heat pipe towards the adiabatic section. As a result, the meniscus contact angle distributions in the heat loaded sections were even more uniform than those in the horizontal case. Note that the meniscus angles in the condenser differ very slightly from the maximum value, and their values in the evaporator can be almost the same as that in the condenser for positive φ . The corresponding longitudinal distributions of the local heat transfer coefficients in the evaporator and condenser and also wall and vapor temperature variations are shown in Figs. 4.2(b) and 4.2(c). The local heat transfer coefficient in the middle of the condenser was about two times larger than at the entrance or end cap, which resulted in the external wall temperature variation shown in Fig. 4.2(c). In the evaporator section, the variation of the local heat transfer coefficient was weaker (for heat loads which are not close to the maximum), so the

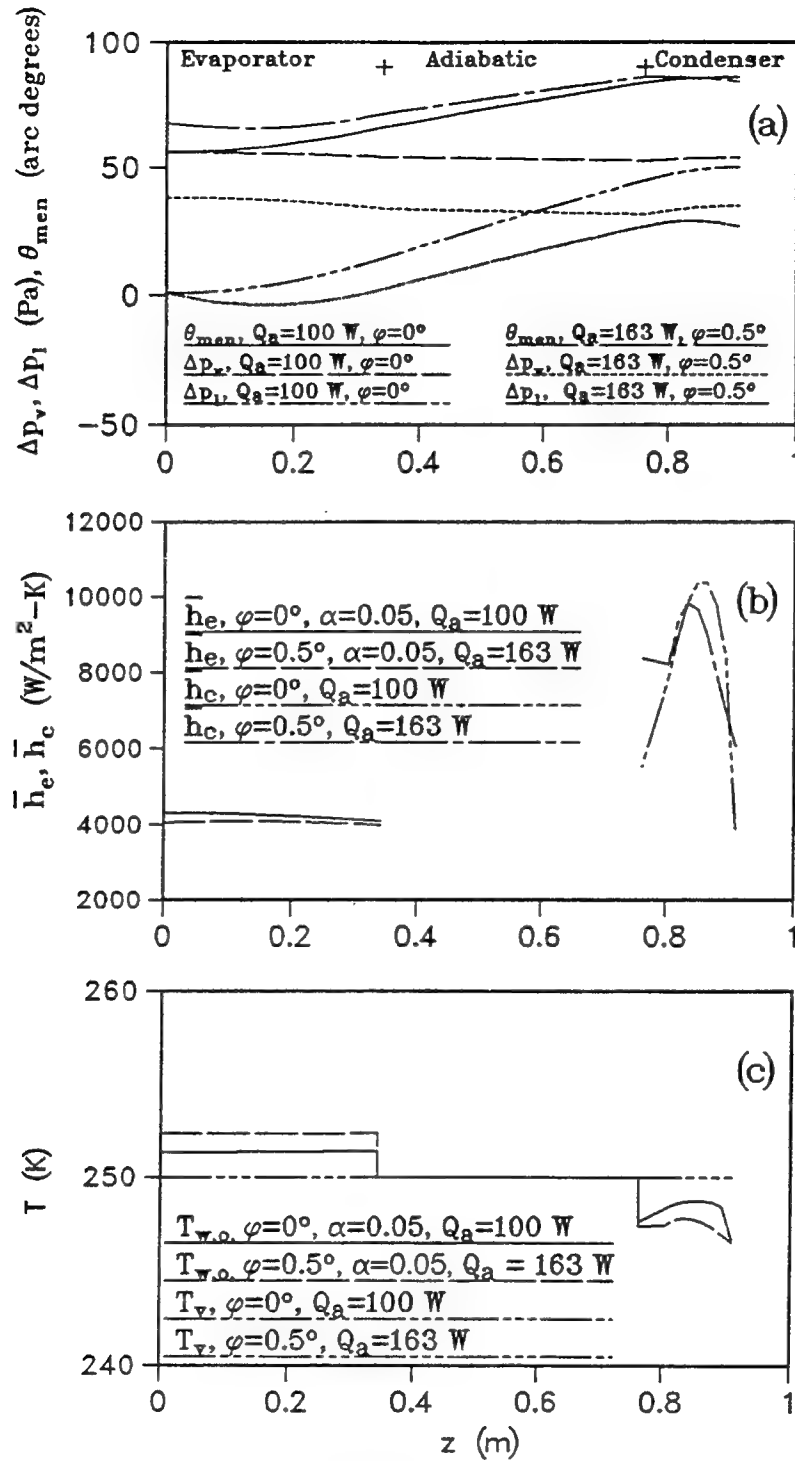


Figure 4.2: Performance characteristics of the ammonia-Al heat pipe ($T_v = 250 \text{ K}$)

(a) meniscus contact angle and fluid pressure, (b) local heat transfer coefficients, (c) wall and vapor temperatures

wall temperature profile was very smooth. The temperature drop along the vapor flow was less than 0.01 K.

The comparison of the computational results with the experimental data on heat transfer for the AGHPs evaporators by Schlitt et al. (1974) and for the planar water-copper evaporator by Ivanovskii et al. (1984) is presented in Fig. 4.3 for ammonia ($L_e = 0.343$ m, $T_v = 250$ K), ethane ($L_e = 0.15$ m, $T_v = 200$ K) and water ($W = 0.17$ mm, $t_g = 0.8$ mm, $L_1 = 0.25$ mm, $L_e = 100$ mm, $T_v = 300$ K; the heated surface was of about 40 cm²). The agreement of the results is good for $\alpha \ll 1$ since it was noted by Carey (1992, p. 119) that, for some substances (ethanol, methanol, water, etc.), the accommodation coefficient had been found to have very small values (0.02 to 0.04) in the experiments of Paul (1962). The physical reason for low values of α in the microfilm region of the evaporator can be the concentration of the contaminants which usually exist in a heat pipe in this region. While the experimental data for the temperature drops for ethane were still higher than those predicted, more precise values of the accommodation coefficient and dispersion constants are needed. For the copper-water evaporator the predicted boiling limit heat flux was 37 W/cm², and no boiling was reported by Ivanovskii et al. (1984), even though the liquid superheat exceeded 20 K at $q_e = 20$ W/cm² in the experiments. For a larger number of grooves per unit width such as in the AGHP by Plesch et al. (1991), the heat transfer coefficient should be higher because of the increase in

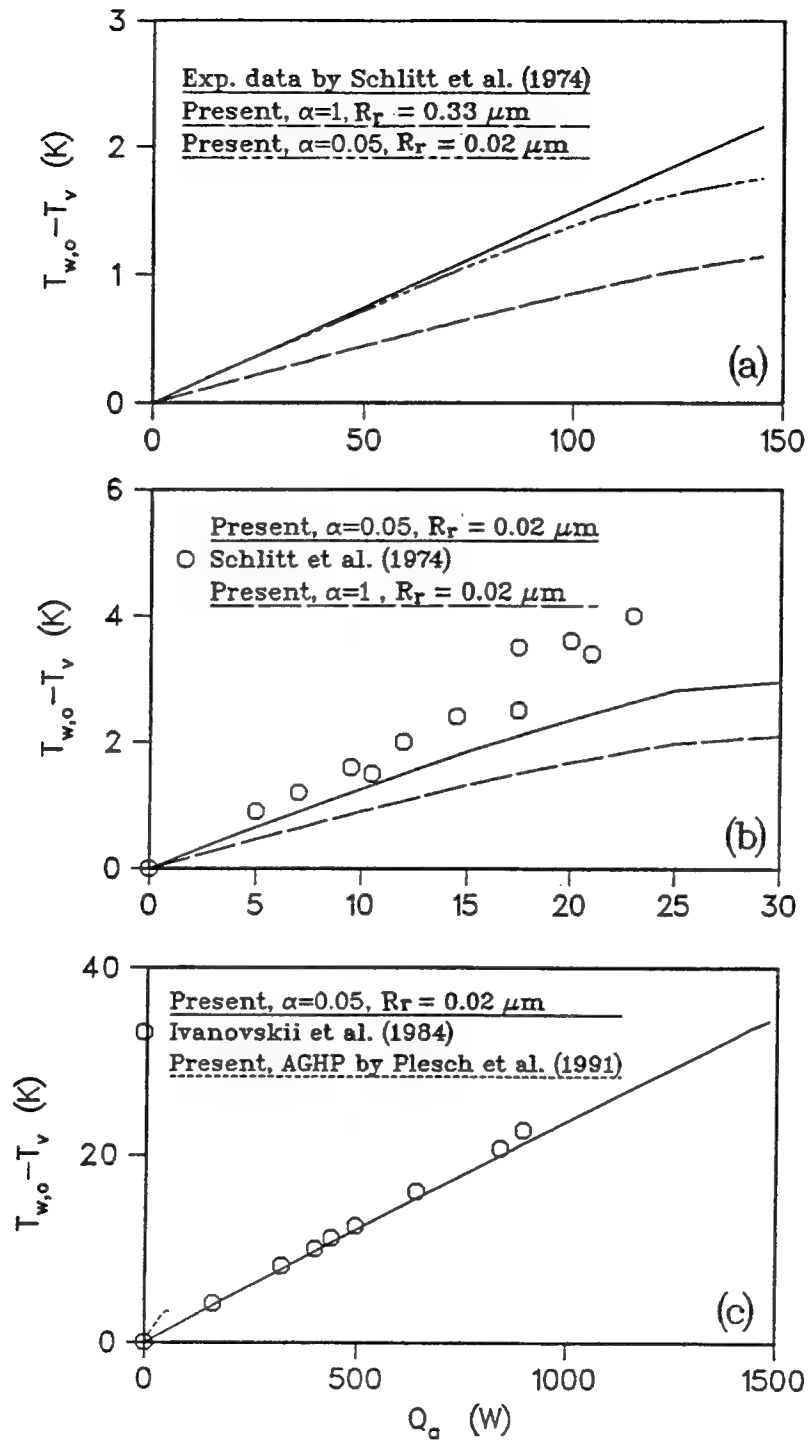


Figure 4.3: Temperature drop in the evaporator versus heat load (a) ammonia-Al heat pipe ($T_v = 250$ K), (b) ethane-Al heat pipe ($T_v = 200$ K), (c) water-copper planar evaporator ($T_v = 300$ K) and flat miniature AGHP ($T_v = 378$ K)

the thin film region over the same area. The characteristic values of the evaporative heat transfer coefficients for the evaporator by Ivanovskii et al. (1984) were 10,000 W/(m²-K), while for the miniature AGHP by Plesch et al. (1991) the predicted values of \bar{h}_e were larger than 40,000 W/(m²-K). Thus, the boiling limitation should take place at larger heat fluxes for narrower grooves.

The agreement between the predicted temperature drop in the condenser and the experimental results by Schlitt et al. (1974) can be seen from Fig. 4.4 for the ammonia ($T_v = 250$ K) and ethane ($T_v = 200$ K) heat pipes. As the heat load increased, the thermal resistance of the condenser increased and the evaporator thermal resistance decreased (see Figs. 4.3 and 4.4) due to the changes in the meniscus contact angle longitudinal distribution.

The numerically obtained values for the maximum heat transfer capacity of the AGHPs have been also compared with the experimental data by Schlitt et al. (1974) for ammonia (Fig. 4.5(a), $L_e = 0.3$ m, $T_v = 203$ K) and ethane (Fig. 4.5(b), $L_e = 0.15$ m, $T_v = 200$ K) within the assumption that $\theta_{\min} = 0$. Some disagreement of the results for comparatively large inclination angles (elevation) when the evaporator end is elevated can be explained by the complicated meniscus shape at the evaporator end, which is not described by the present model. However, for smaller tilt angles the agreement is satisfactory.

The second heat pipe configuration considered here is the AGHP investi-

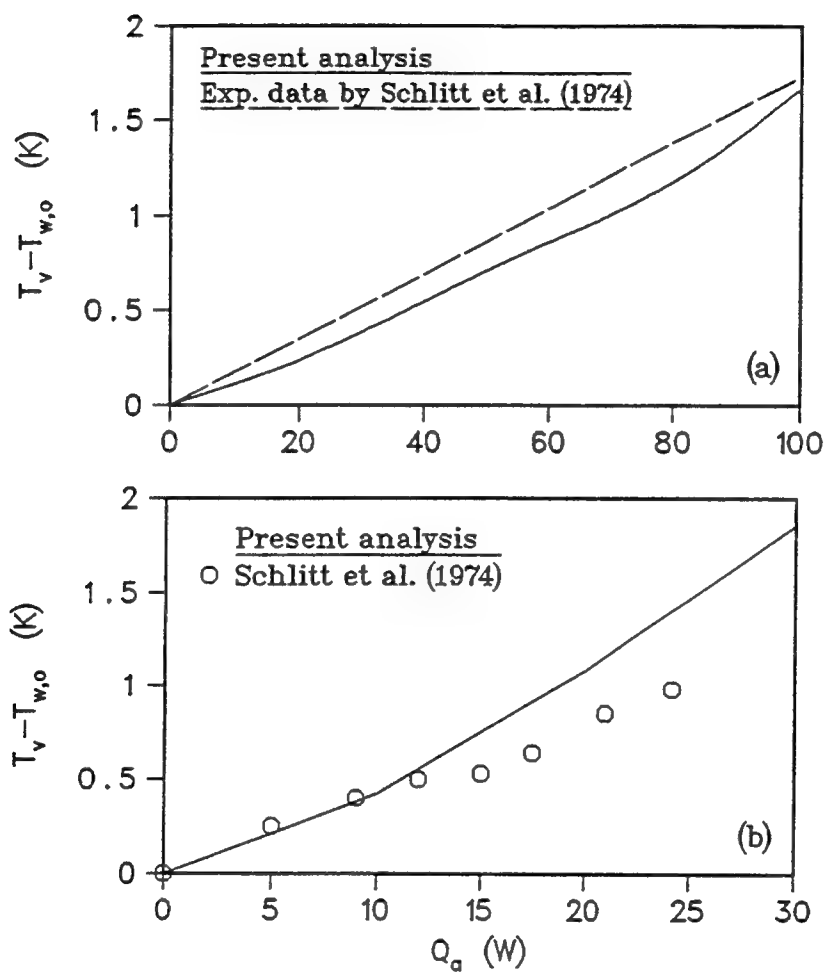


Figure 4.4: Temperature drop in the condenser versus heat load: (a) ammonia-Al heat pipe ($T_v = 250$ K), (b) ethane-Al heat pipe ($T_v = 200$ K)

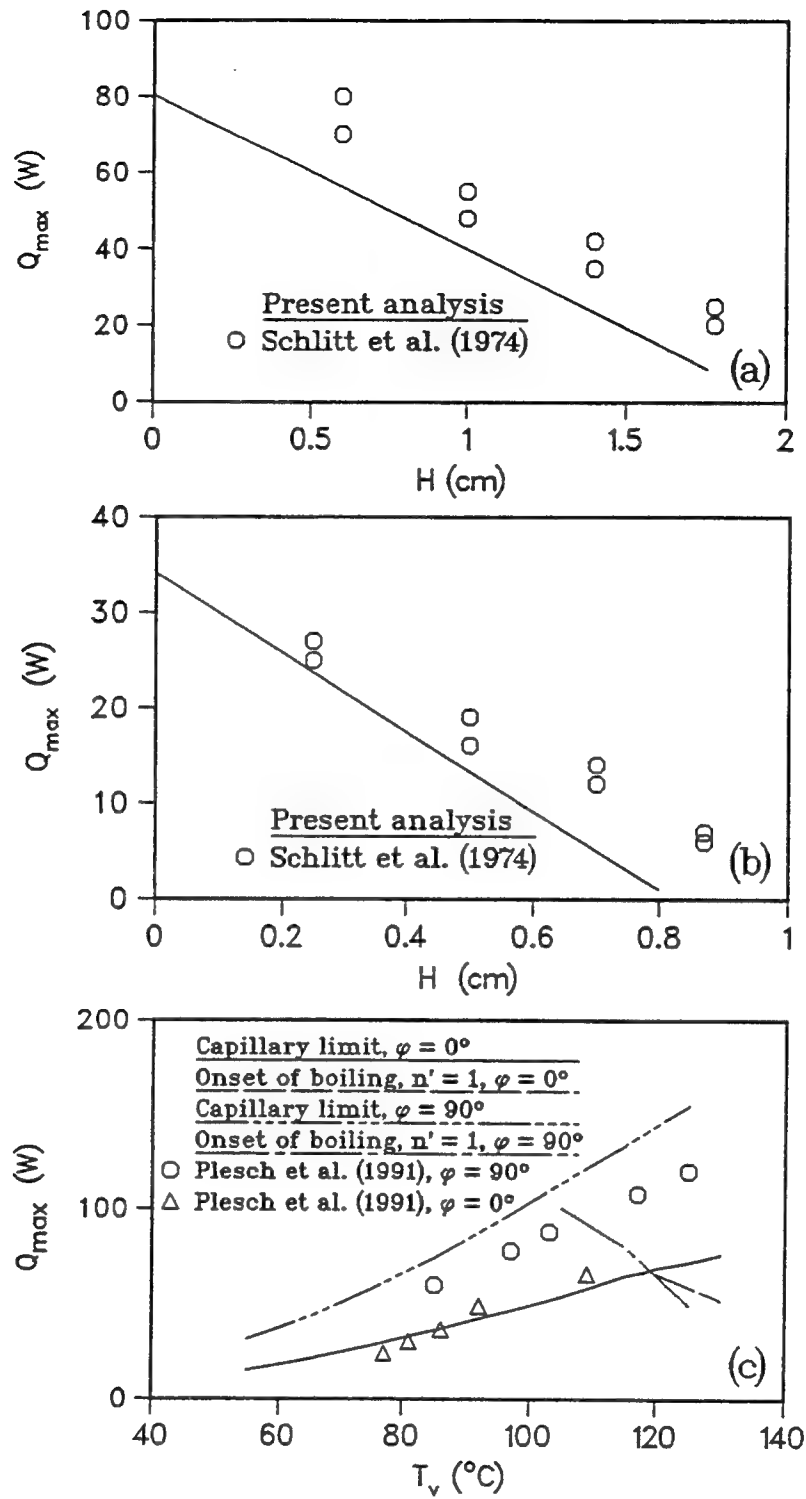


Figure 4.5: Maximum heat transfer versus elevation height (a) ammonia-Al heat pipe ($T_v = 203$ K), (b) ethane-Al heat pipe ($T_v = 200$ K), (c) water-copper flat miniature heat pipe

gated experimentally by Plesch et al. (1991). The cross sections are shown in Fig. 4.1 and the AGHPs geometrical characteristics are: $W = 0.06$ mm, $L_1 = 0.02$ mm, $t_g = 0.24$ mm, $t = 2$ mm, $t_w = 0.22$ mm, $L_e = 20$ mm, $L_a = 80$ mm, $L_c = 20$ mm, $N = 80$. The casing material was copper and the working fluid was pure water. Therefore, the minimum contact angle was set to $\theta_{\min} = 33^\circ$ (Stepanov et al., 1977). The heaters were situated at both sides of the evaporator with an overall heated surface of 2.56 cm². The numerical results for the maximum heat flow, Q_{\max} , transferred by the flat miniature AGHP are shown in Fig. 4.5(c), where it can be seen that Q_{\max} increased with the operating temperature. However, for $T_v > 100^\circ\text{C}$, it was restricted by the boiling limitation. To validate the numerical results, a comparison with two of the most representative series of the experimental data by Plesch et al. (1991) was made, as shown in Fig. 4.5(c). It should be noted that the experimental results by Plesch et al. (1991) were given (and plotted in Fig. 4.5(c)) versus the evaporator surface temperature, and it was not mentioned directly if the data for the measured heat flow rate were at a maximum. The numerical predictions of the capillary limit for both the horizontal ($\varphi = 0$) and vertical ($\varphi = 90^\circ$) orientations follow the experimental data. The temperature drop along the vapor flow was less than 0.4 K in the numerical experiments while the temperature drop in the evaporator reached several degrees (Fig. 4.3(c)). The influence of the grooved surface geometry on the maximum heat transfer through the flat AGHP with the external dimensions $2 \times 7 \times 120$ mm is

shown in Figs. 4.6 and 4.7 for the vertical and horizontal orientations, respectively. While the values of W and t_g were changed, the fin half-width and the wall thickness were kept constant at $L_1 = 0.02$ mm and $t_w = 0.22$ mm. The number of grooves N was different for different W , while the external dimensions were the same. Also, the vapor channel height was dependent on t_g because of the same reason. For the vertical orientation at $T_v = 55^\circ\text{C}$, the capillary limit restricted the maximum heat flux in the evaporator, which had a maximum value of about 15 W/cm^2 for $W = 0.03$ to 0.04 mm (Fig. 4.6(a)). For $T_v = 105^\circ\text{C}$ both the capillary and boiling limits occurred as shown in Fig. 4.6(b), and the optimal groove half width was about 0.05 mm with an absolute maximum heat flux of 40 W/cm^2 . In the horizontal orientation the maximum heat fluxes were 8 W/cm^2 (for $W = 0.03$ mm, $T_v = 55^\circ\text{C}$) and 25 W/cm^2 (for $W = 0.04$ mm, $T_v = 105^\circ\text{C}$) as shown in Fig. 4.6.

It is anticipated that in order to reach higher heat fluxes, more advanced heat pipe configurations should be used.

4.8 Conclusions

The numerical results of the mathematical model describing the fluid flow and heat transfer in the conventional and miniature axially-grooved heat pipes are summarized as follows:

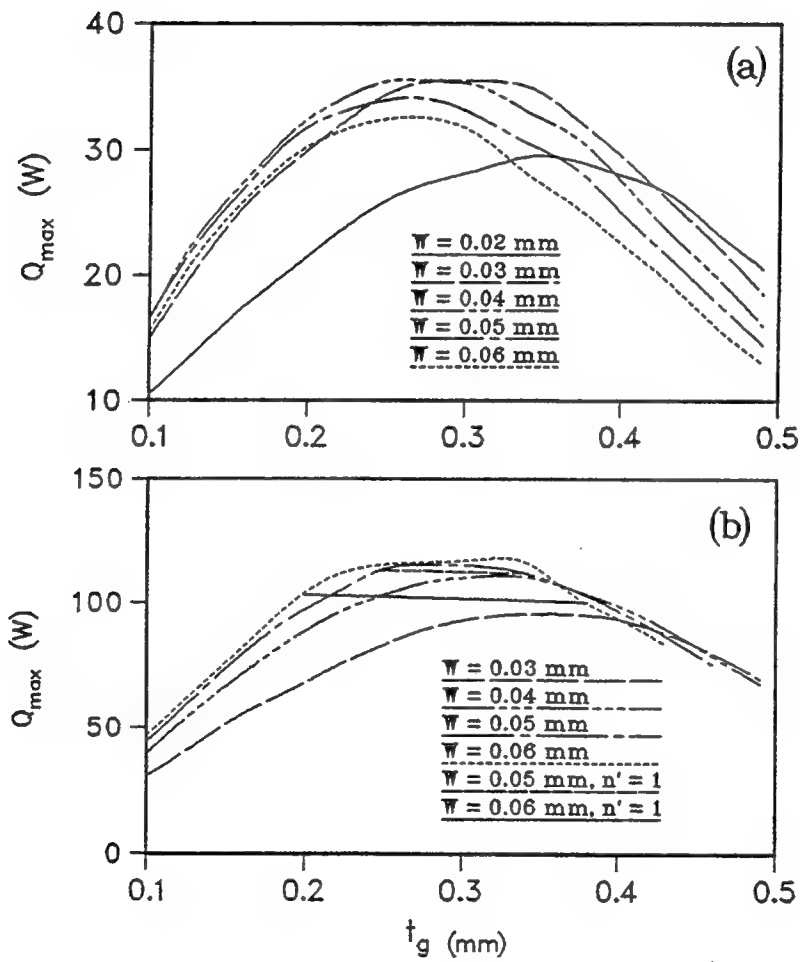


Figure 4.6: Maximum heat transfer of the flat miniature heat pipe versus groove depth (vertical orientation) (a) $T_v = 55^\circ$, (b) $T_v = 105^\circ$

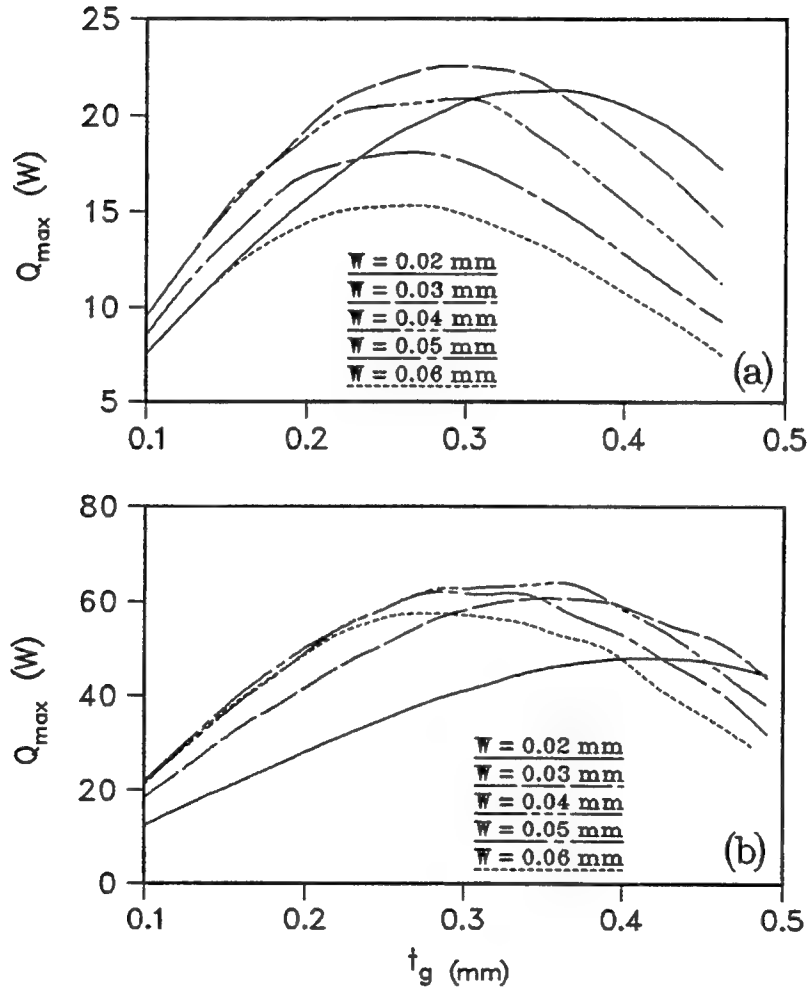


Figure 4.7: Maximum heat transfer of the flat miniature heat pipe versus groove depth (horizontal orientation) (a) $T_v = 55^\circ$, (b) $T_v = 105^\circ$

1. The validity of the present mathematical model for axially-grooved heat pipes has been confirmed, in general, by comparisons with existing experimental data. However, more detailed information concerning the values of the accommodation coefficients and dispersion constants is needed.
2. An increase of the heat load decreased the evaporator thermal resistance and increased the condenser thermal resistance due to changes in the longitudinal meniscus angle distribution along the AGHP in the horizontal position.
3. The maximum heat flux in the evaporator of the flat miniature copper-water AGHP was restricted by both the capillary and boiling limitations in the interval of the operating temperature from $T_v = 90$ to 120°C .
4. Due to the fact that the greatest part of the heat flow through the liquid is transferred in the region where the liquid film thickness is comparatively small, grooved evaporators are capable of withstanding high heat fluxes. The optimized copper-water flat AGHP with external dimensions $2 \times 7 \times 120$ mm could operate at maximum heat fluxes in the evaporator of 25 and 40 W/cm^2 for the horizontal and vertical orientations, respectively, provided that the operating temperature was high enough ($T_v = 90$ to 120°C).

REFERENCES

Ayyaswamy, P.S., Catton, I., and Edwards, D.K., 1974, "Capillary Flow in Triangular Grooves," *J. Applied Mechanics*, Ser. E, Vol. 41, No. 2, pp. 332-336.

Babenko, V.A., Levitan, L.L. and Khrustalev, D.K., 1981, "Heat Transfer in Condensation on a Grooved Surface," *J. Engineering Physics and Thermophysics*, Vol. 40, No. 6, pp. 615-619.

Babin, B.R., Peterson, G.P., and Wu, D., 1989, "Analysis and Testing of a Micro Heat Pipe During Steady-State Operation," *Proc. ASME/AIChE National Heat Transfer Conf.*, 89-HT-17, August 5-8, Philadelphia, Pennsylvania.

Bankston, C.A., and Smith, H.I., 1972, "Incompressible Laminar Flow in Cylindrical Heat Pipes," ASME Paper No. 71-WA/HT-15.

Bankston, C.A., and Smith, H.J., 1973, "Vapor Flow in Cylindrical Heat Pipes," *ASME J. Heat Transfer*, Vol. 95, pp. 371-376.

Bar-Cohen, A., Mudawar, I., and Whalen, B., "Future Challenges," *Proc. NSF/Purdue Sponsored Workshop on Research Needs in Electronic Cooling*, Andover, Massachusetts, 1986.

Bowman, W. J., and Hitchcock, J. E., 1988, "Transient, Compressible Heat-Pipe Vapor Dynamics," *Proc. ASME National Heat Transfer Conf.*, Houston, TX, Vol. 1, pp. 329-338.

Cao, Y., and Faghri, A., 1992a, "A Numerical Simulation of High Temperature Heat Pipe Startup From the Frozen State," to appear in *ASME J. Heat Transfer*.

Cao, Y., and Faghri, A., 1992b, "Analyses of Transient and Steady-State Performances of Nosecap and Wing Leading Heat Pipes," *Proc. ASME Annual Meeting*, Anaheim, CA, Nov. 1992.

Cao, Y., and Faghri, A., 1994, "Micro/Miniature Heat Pipes and Operating Limitations," *Journal of Enhanced Heat Transfer*, Vol. 1, No. 3, 1994, pp. 265-274.

Carey, V.P., 1992, *Liquid-Vapor Phase-Change Phenomena: An Introduction to the Thermophysics of Vaporization and Condensation Processes in Heat Transfer Equipment*, Hemisphere, New York.

Chen, H., Groll, M., and Rosler, S., 1992, "Micro Heat Pipes: Experimental Investigation and Theoretical Modeling," *Proc. 8th Int. Heat Pipe Conf.*, Beijing, China.

Chi, S.W., 1976, *Heat Pipe Theory and Practice*, McGraw-Hill, New York.

Cotter, T.P., 1984, "Principles and Prospects for Micro Heat Pipes," *Proc. 5th Int. Heat Pipe Conf.*, Tsukuba, Japan, pp. 328-335.

Dasgupta, S., Sujanani, M., and Wayner, P.C., Jr., 1991, "Microcomputer Enhanced Optical Investigation of an Evaporating Liquid Film Controlled by a Capillary Feeder," in *Experimental Heat Transfer, Fluid Mechanics and Thermodynamics*,

Edt. Keffer, J.F., Shan, R.K., and Ganic, E.N., pp. 361-368.

Derjaguin, B.V., 1955, "Definition of the Concept of and Magnitude of the Disjoining Pressure and its Role in the Statics and Kinetics of Thin Layers of Liquid," *Kolloidny Zhurnal*, Vol. 17, pp. 191-197.

Faghri, A., 1989, "Performance Characteristics of a Concentric Annular Heat Pipe: Part II - Vapor Flow Analysis," *ASME J. Heat Transfer*, Vol. 111, pp. 851-857.

Gerner, F.M., Longtin, J.P., Henderson, H.T., Hsieh, W.M., Ramadas, P., and Chang, W.S., 1992, "Flow Limitations in Micro Heat Pipes," *Proc. 28th ASME National Heat Transfer Conf.*, San Diego, California.

Holm, F.W., and Goplen, S.P., 1979, "Heat Transfer in the Meniscus Thin-Film Transition Region," *ASME J. Heat Transfer*, Vol. 101, No. 3, pp. 543-547.

ITOH Research & Development Laboratory Co., LTD., Japan.

Itoh, A., and Polasek, F., 1990a, "Development and Application of Micro Heat Pipes," *Proc. 7th International Heat Pipe Conf.*, Minsk, USSR, May 21-25.

Itoh, A., and Polasek, F., 1990b, "Micro Heat Pipes and Their Application in Industry," *Proc. Czechoslovak-Japanese Symposium on Heat Pipes*, Ricany, Czechoslovakia.

Ivanovskii, M.N., Privezentsev, V.V., Il'in, Yu.A., and Sidorenko, E.M., 1984, "Experimental Investigation of Heat Transfer with Evaporation of the Agent

from a Corrugated Capillary Structure," *J. Engineering Physics and Thermophysics*, Vol. 46, No. 4, 377-381.

Jacobs, H.R., and Hartnett, J.P., 1991, "Thermal Engineering: Emerging Technologies and Critical Phenomena," Workshop Report, NSF Grant No. CTS-91-04006, pp. 139-176.

Jang, J.H., Faghri, A., and Chang, W.S., 1991, "Analysis of the Transient Compressible Vapor Flow in Heat Pipes," *Int. J. Heat Mass Transfer*, Vol. 34, pp. 2029-2037.

Jensen, M.K., and Memmel, G.J., 1986, "Evaluation of Bubble Departure Diameter Correlations," *Proc. 8th Int. Heat Transfer Conf.*, Vol. 2, pp. 1907-1912.

Kamotani, Y., 1976a, "Analysis of Axially Grooved Heat Pipe Condensers," AIAA Paper No. 76-147.

Kamotani, Y., 1976b, "Thermal Analysis of Axially Grooved Heat Pipes," *Proc. 2nd Int. Heat Pipe Conf.*, Bologna, Italy, pp. 83-91.

Kamotani, Y., 1978, "Evaporator Film Coefficients of Grooved Heat Pipes," *Proc. 3rd Int. Heat Pipe Conf.*, Palo Alto, pp. 128-130.

Khrustalev, D.K., 1981, "Liquid Flow Through Capillary Grooves With Shear Stresses on a Free Surface," in *Heat and Mass Transfer in Porous-Element Systems*, pp. 51-56, HMTI, Minsk.

Khrustalev, D.K., and Faghri, A., 1993, "Heat Transfer During Evaporation and Condensation on Capillary-Grooved Structures of Heat Pipes," *ASME J. Heat Transfer*, (submitted).

Kojima, Y., Yamazaki, N., Yoshida, K., Mishiro, H., and Murakami, M., 1992, "LSI Cooling System with Micro Heat Pipe," *Proc. 8th Int. Heat Pipe Conf.*, Beijing, China.

Labuntsov, D.A., and Krukov, A.P., 1977, "Intensive Evaporation Processes," *Thermoenergetics*, No. 4, pp. 8-11.

Lance, G.N., 1960, *Numerical Methods for High Speed Computers*, ILIFEE, London, pp. 134-138.

Lee, Y.S., Lee, Y.P., and Lee, Y., 1992, "An Experiment study on Micro Two-Phase Closed Thermosyphons with Inserts," *Proc. 8th Int. Heat Pipe Conf.*, Beijing, China.

Li, T., Cao, L., and Xiang, L., 1992, "Research and Application for the Heat Transfer Performance of Small Heat Pipes," *Proc. 8th Int. Heat Pipe Conf.*, Beijing, China.

Longtin, J.P., Badran, B., and Gerner, F.M., 1992, "A One-Dimensional Model of a Micro Heat Pipe During Steady-State Operation," *Proc. 8th Int. Heat Pipe Conf.*, Beijing, China, Preprints, pp. C-5-1 to C-5-7.

Lorenz, J.J., Mikic, B.B., and Rohsenow, W.M., 1974, "The Effect of Surface Conditions on Boiling Characteristics," *Proc. 8th Int. Heat Transfer Conf.*, Vol. 4, p. 35.

Paul, B., 1962, "Compilation of Evaporation Coefficients," *ARS J.*, Vol. 32, pp. 1321-1328.

Peterson, G.P., 1990, "Analytical and Experimental Investigations of Micro Heat Pipes," *Proc. 7th Int. Heat Pipe Conf.*

Plesch, D., Bier, W., Seidel, D., and Schubert, K., 1991, "Miniature Heat Pipes for Heat Removal from Microelectronic Circuits," in *Micromechanical Sensors, Actuators, and Systems* (Edited by D.Cho, R.Warrington, Jr., et al.), DCS-Vol. 32, 303-313, ASME, New York.

Pletcher, R.H., Minkowycz, W.J., Sparrow, E.M., and Schneider, G.E., 1988, "Overview of Basic Numerical Methods," in *Handbook of Numerical Heat Transfer*, John Wiley, New York.

Potash, Jr., M., and Wayner, Jr., P.C., 1972, "Evaporation from a Two-Dimensional Extended Meniscus," *Int. J. Heat Mass Transfer*, Vol. 15, pp. 1851-1863.

Schlitt, K.R., Kirkpatrick, J.P. and Brennan, P.J., 1974, "Parametric Performance of Extruded Axial Grooved Heat Pipes from 100 K to 300 K," *Proc. AIAA/ASME Thermophysics and Heat Transfer Conf.*, AIAA Paper 74-724.

Schneider, G.E., Yovanovich, M.M. and Wehrle, V.A., 1976, "Thermal Analysis of Trapezoidal grooved Heat Pipe Evaporator Walls," AIAA Paper 76-481.

Schneider, G.E., and DeVos, R., 1980, "Nondimensional Analysis for the Heat Transport Capability of Axially-Grooved Heat Pipes Including Liquid/Vapor Interaction," AIAA Paper No. 80-0214.

Schonberg, J., and Wayner, P., 1990, "An Analytical Solution for the Integral Contact Line Evaporative Heat Sink," *Proc. AIAA/ASME 5th Joint Thermophysics and Heat Transfer Conf.*, June 18-20, Seattle, WA.

Shah, R.K., and Bhatti, M.S., 1987, "Laminar Convective Heat Transfer in Ducts," in *Handbook of Single Phase Convective Heat Transfer*, Kakac et al., eds., Wiley, New York.

Shekrladze, I.G. and Rusishvili, D.G., 1987, "Evaporation and Condensation on Grooved Capillary Surfaces," *Proc. 6th Int. Heat Pipe Conf.*, Grenoble, pp. 173-176.

Solov'yev, S.L., and Kovalev, S.A., 1984, "Mechanism of Evaporation of a Liquid from a Porous Surface," *Proc. 5th Int. Heat Pipe Conf.*, Tsukuba, Japan, Preprints Vol. II, pp. 77-82.

Stephan, P., 1992, *Wärmedurchgang bei Verdampfung aus Kapillarrillen in Wärmerohren*, Fortschr.-Ber. VDI Reihe 19 Nr. 59. Düsseldorf: VDI-Verlag.

Stephan, P.C., and Busse, C.A., 1992, "Analysis of the Heat Transfer Coefficient of Grooved Heat Pipe Evaporator Walls," *Int. J. Heat Mass Transfer*, Vol. 35, No. 2, pp. 383-391.

Stepanov, V.G., Volyak, L.D., and Tarlakov, Yu.V., 1977, "Wetting Contact Angles for Some Systems," *J. Engineering Physics*, Vol. 32, No. 6, pp. 1000-1003.

Tien, C.L., and Lienhard, H.H., 1979, *Statistical Thermodynamics*, Hemisphere Publishing Corporation, New York.

Vasiliev, L.L., Grakovich, L.P. and Khrustalev, D.K., 1981, "Low-Temperature Axially Grooved Heat Pipes," *Proc. 4th Int. Heat Pipe Conf.*, London, pp. 337-348.

Wayner, P.C., Jr., Kao, Y.K. and LaCroix, L.V., 1976, "The Interline Heat-Transfer Coefficient of an Evaporating Wetting Film," *Int. J. Heat Mass Transfer*, Vol. 19, pp. 487-492.

Wu, D., and Peterson, G., 1990, "Experimental Investigation of the Transient Behavior of Micro Heat Pipes," *Proc. AIAA/ASME 5th Joint Thermophysics and Heat Transfer Conf.*, June 18-20, Seattle, WA.

Wu, D., and Peterson, G.P., 1991, "Investigation of the Transient Characteristics of a Micro Heat Pipe," *J. Thermophysics*, Vol. 5, No. 2, pp. 129-134.

Zhang, J., Wang, C., Yang, X., and Zhou, Z., 1992, "Experimental Investigation of the Heat Transfer Characteristics of the Micro Heat Pipes," *Proc. 8th Int. Heat Pipe Conf.*, Beijing, China.

Zhou, J., Yao, Z., and Zhu, J., 1992, "Experimental Investigation of the Application Characters of Micro Heat Pipe," *Proc. 8th Int. Heat Pipe Conf.*, Beijing, China.